UNIVERSITÀ DEGLI STUDI DI PADOVA

DIPARTIMENTO DI INGEGNERIA INDUSTRIALE

CORSO DI LAUREA MAGISTRALE IN INGEGNERIA DEI MATERIALI

Tesi di Laurea Magistrale

Investigation of the Flexural Fatigue Behavior of Stone-Faced Cork Agglomerate Sandwich Composite

Relatore: Prof. Mauro Ricotta

Laureanda: Ilaria Andreazza

A.A 2016/2017

A mamma Nadia,

e papà Nicola.

Riassunto

Un nuovo concetto di rivestimento per edifici è stato ideato da un decennio a questa parte, con l'obiettivo di mantenere l’apprezzato aspetto della pietra naturale, ma aumentandone la tenacità e diminuendone il peso specifico. Questo è stato possibile rinforzando un pannello di pietra con materiali più leggeri e resistenti come il nido d'ape o, in questo caso, agglomerato di sughero. Sebbene tali rivestimenti non abbiano un ruolo strutturale, la loro caratterizzazione a fatica è necessaria poichè durante tutta la loro vita sono caricati con una forza variabile nel tempo, proveniente principalmente dal vento.

In questa tesi, due prove cicliche sono state ideate sulla base di una ricerca bibliografica, ed eseguite. Il materiale studiato, rientrante nella classe dei rivestimenti per edifici, è costituito da uno strato di pietra calcarea e uno strato di agglomerato di sughero rinforzato; il rinforzo viene eseguito con fibre di vetro su entrambi i lati. Sono state prodotte e testate due configurazioni, L1C1 e L2C1, che utilizzano pietre con diverso modulo di elasticità e porosità. Le prove di flessione a quattro punti hanno un rapporto di carico di 0,1 e carico massimo assunto come percentuale del carico statico a rottura (F_{UF}), cioè da 0,70 e 0,85 F_{UF} per la configurazione denominata L1C1, e da 0,40 a 0,70 F_{UF} per la configurazione L2C1.

Un test continuo è stato eseguito fino a 500'000 cicli o fino al fallimento del materiale, e un test con tempo di riposo dopo ogni blocco di cicli è stato utilizzato per valutare l'influenza del recupero viscoelastico del sughero. La microstruttura della pietra è stata analizzata con tomografia computerizzata a raggi X, una nuova tecnica nel campo delle scienze della terra.

È stato possibile determinare la validità del test, la presenza o meno di fatica sui materiali che compongono gli strati, e fornire un'indicazione qualitativa del comportamento del materiale in servizio. Sono state osservate diverse modalità di danneggiamento per le due configurazioni e per la stessa configurazione testata con e senza riposo. Le modalità di danneggiamento variano in base al carico massimo; nel composito L1C1 la rottura avviene sempre per indentazione della pietra; in L2C1 viene osservata, oltre alla rottura per indentazione, un’altra modalità di rottura per danneggiamento delle fibre inferiori. I test con tempo di riposo non hanno mostrato prova statistica di un aumento della vita a fatica rispetto ai test continui.

L'assenza di letteratura sulla fatica di compositi sandwich asimmetrici con *core* in sughero rende il lavoro attuale innovativo nel proprio campo.

Parole chiave: pietra, sughero, test di fatica, danno, composito asimmetrico, sandwich.

Abstract

A new concept of cladding has been invented since a decade, with the aim of maintaining the much-appreciated look of natural stone, and at the same time increasing its toughness, safety, and diminishing its specific weight. This has been possible backing a stone veneer with lighter and more resilient materials such as honeycomb or, in the present case, cork agglomerate. Although such claddings do not have a structural role, their characterization in fatigue is needed because throughout their life they will be loaded with a force variable in time coming mainly from the wind.

In this thesis, two cyclic tests have been chosen on the basis of a literature research, and carried on. The material used is made of a layer of limestone and a layer of reinforced-cork agglomerate; the reinforcement is done with glass fibers on both sides. Two configurations, L1C1 and L2C1, using limestones having different modulus of elasticity and porosity, have been manufactured and tested. The four-point bending tests had a load ratio of 0.1 and maximum load taken as a percentage of the maximum static load, i.e. from 0.70 and 0.85 of the static load for configuration named L1C1, and from 0.40 to 0.70 of the static load for configuration L2C1.

A continuous test was carried out up to 500’000 cycles or up to failure of the material, and a test with resting time after each block of cycles was used to evaluate the influence of the viscoelastic recovery of the cork. The microstructure of the stone has also been analyzed with X-Ray Computerized Tomography, a novel technique in the field of rock science. It has been possible to evaluate the validity of the test, the occurrence or not of fatigue on the materials composing the layers, and to give a qualitative indication of the behavior of the material in service. There has been observation of different failure modes for the two configurations, and for the same configuration tested with and without stops. The failure modes vary according to the maximum load; stone indentation was always observed in the composite with the weakest stone, fiber breakage was observed for the first time on the other configuration. The tests with resting time did not show a statistical increase in lifetime compared to the continuous tests.

The absence in the literature of research on the fatigue of asymmetric sandwich composites makes the present work innovative in the field.

Keywords: stone, cork, fatigue test, damage, asymmetric composite, sandwich.

Table of contents

List of symbols

d	Deformation
D_{abs}	Absolute stiffness
d_{acc}	Accumulated deformation
D_{rel}	Relative stiffness
E	Young's modulus
F	Load
F_A	Force amplitude of the fatigue cycle
F_{MAX}	Maximum force of the fatigue cycle
F_{MIN}	Minimum force of the fatigue cycle
F_{UF}	Failure load of static 4-pt bending test
K_I	Mode I stress concentration factor
K_{IC}	Critical stress concentration factor
M	Bending moment
m	Weibull modulus
N_f	Number of cycles at failure
R	Load ratio of the fatigue cycle
t	Thickness
v	Poisson's ratio
σ	Normal stress
σ'	Modified Weibull stress
σ_θ	Characteristic Weibull stress
τ	Shear stress
ε	Strain

List of figures

List of tables

Chapter 1.
Introduction

1.1 Objectives

The present dissertation project aims at identifying the damage mechanisms leading to fatigue failure in a specific unsymmetric composite material, made of a stone backed by a cork agglomerate sandwich. The effect of varying the type of stone will also be evaluated. This material has been the subject of previous research studies, due to the outstanding combination of mechanical resistance, acoustic and thermal insulation properties it possesses. Moreover, it has the potential to have a reasonably low environmental impact due to the presence of two fully biodegradable materials which make up the 95% of the product's volume, namely stone and cork, although an environmental analysis still needs to be assessed. In the application envisioned by the designer of this material, the latter will not have a structural function but rather an aesthetical one, e.g. as cladding for façades or as flooring system. Being this composite a rather new one, both because of the materials used and because of its asymmetric architecture, a full characterization of it is still missing. Therefore, the present work will try to partially fill this knowledge gap.

In the current work, the approach used will be that of a Materials Engineer, which aims at detecting and understanding the mechanisms involved with the initiation of the fatigue phenomenon and those related to the accumulation of damage, in relation to the microstructural properties of the material. It differentiates from the Mechanical Engineer's point of view in the sense that it will not try to predict the life-time of the composite with empirical formulae and correcting coefficients, as in the case, for example, of the renown Wohler curves. Neither of the cited approaches is thought to be better than the other. The goal of all the studies is the fusion of both points of view in a general and holistic model.

Out of all the classes of materials, composite materials (or composites) are not characterized by a specific chemical structure, but by the fact that two or more phases are joined in the formation of the final structure. The new material will have different properties from those of the original constitutive materials, which, if well designed, prove to be superior. Possibilities to join two or more materials and obtain a new one are obviously endless! One common example of composite material is reinforced concrete, made by a dispersed phase of aggregates, held together by a cement matrix. To provide the aggregate-filled cement with tensile resistance, steel bars run through the matrix. Reinforced-concrete falls into the category of matrix-reinforced composites, in which the reinforcement can be in the form of particles, short fibers, long fibers or woven fabrics. The common features of matrix-reinforced composites are, as the name suggests, the presence of a matrix, which is usually ductile, and of a reinforcement phase, which is sustaining the applied stress.

A different approach in the creation of composite materials is encountered in sandwich composites: in this case, a lightweight core is joined to two stiffer faces. The moment of inertia of the section increases, as the thickness of the core increases, making the sandwich a lightweight option able to resist high bending stresses; the stiff faces carry the tensile and compressive loads, while the core transmits shear loads. This technology is extensively used in aircrafts, vehicles, marine vessels, refrigerator containers etc., with cores made of honeycomb or foams.

A large amount of literature is present nowadays in the field of mechanics of composite materials, with comprehensive references on the study of fatigue in fiber-reinforced plastics (Harris 2003) and in sandwich structures (Daniel et al. 2010; Carlsson & Kardomateas 2011; Allen 1969), for example. Unlike for crystalline materials, though, composite fail during fatigue not because of the propagation of a single crack, but they rather accumulate damage in a general fashion (Talreja 2008). Therefore, it has not yet been possible to identify and develop a unique model to predict the fatigue life of a class of composites, as for example for fiber-reinforced composites, because of the too many variables involved in the damage accumulation. Often, though, it is possible to analyse and determine microstructurally which of the mechanisms start to act during the fatigue of a component, according to different stages of its fatigue life.

The challenge of the present work resided in the fact that no literature exists in the topic of fatigue behavior of cork or of cork agglomerates, if not for observation of macroscopical behavior (Reis & Silva 2009). Moreover, the asymmetrical geometry of the assembly makes it incorrect to apply the simplifications that have been used in the study of symmetrical composites.

In summary, the work will have as main objectives:

1. Identification of the damage mechanisms leading to fatigue failure.
2. Evaluation the effect of varying the type of stone.
3. Usage of a materials engineer approach.

In order to reach the objectives, a cyclic fatigue test was designed. The parameters chosen (e.g. control mode, stress state, maximum load) didn’t necessarily come from stress states encountered in application of a real part, but rather related to materials properties. Then, the specimens were tested and the failure modes evaluated through optical, and mechanical methods.

1.2 The material under investigation: commercial use and its competitors

The material object of this thesis is a deposited patent by (Amaral & Pinheiro 2017) and consists of a panel with a stone layer reinforced by a cork agglomerate sandwich layer. Its commercial name is Stork. Such a material was designed for architects, and provides a lightweight resistant, but still aesthetically beautiful, alternative to solid stone claddings. It aims at replacing natural stone in all the applications where the latter is used because, besides retaining the look of a stone cladding, it brings advantages in terms of:

- Cost: reduces transportation and labor costs because of the lower density.
- Design impact: possibility of design of larger panels than those permitted for solid stone.
- Safety: increases safety, because cladding of natural stone fails without warning due to the low tensile strength and brittleness.
- Stability: avoids bowing of natural stone under thermal stresses

All these advantages are a direct consequence of the lower weight of the cork composite compared to natural stone. If and only if stone is reinforced by another material, it is possible to reduce its thickness up to 3 mm, thus reducing its areal density. The production of a layer of stone veneer with a thickness below 5 mm by means of cutting the stone slab (§ 4.1.4) induces high stresses that result in warpage and/or cracking of the material, but when stone is in conjunction with cork or with another backing material, the thickness reduction of the stone panel is done only after the composite is made, hence stone does not break nor warp.

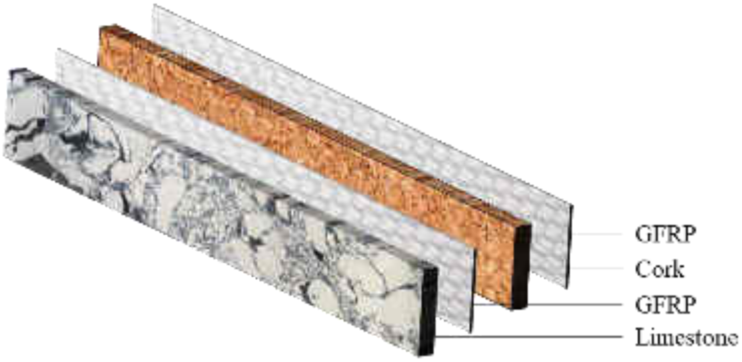

Figure 1.1 Exploded view of the material layers

Table 1.1 Comparison of mechanical properties of common granite cladding (www.stoneply.com), honeycomb backed stone, and Stork® (cork sandwich backed stone).

	Common Granite cladding (Granite, 30 mm)	*Honeycomb backing*	*Cork agglomerate backing (Stork ®)*
Impact Resistance (m kg)	0.75	1.2	1.4
Weight (approximate weight, varies by stone type) (kg/m^2)	80	13	15-18
Maximum flexural load – 3 pt (ASTM C293) (kN)	5.5	3.6	3.5
Maximum flexural load – 4 pt (ASTM C293) (kN)	3.5	1.4	3
Install Speed	Very slow	Fast	Fast
Thickness of Assembly (cm)	10 to 15	1.5 to 3	1.5 to 3

In the market, there are other composites that exploit the same idea of reinforcing a thin stone layer with a dissimilar material of lower density interposed between an adhesive (and fibers), to obtain a lighter alternative to stone cladding. The lighter materials used are honeycomb, aluminum composite panels, or foam glass.

1.3 Stone as a building material

Stone was the most important construction raw material from the Pharaonic Egypt until the Arab period. It was chosen for the construction of temples, monuments, tombs, roads, and the most important buildings because of its hardness, resistance, durability, and aesthetical quality.

In the antient Egypt the final residence of the Pharaohs, unlike the habitations of the civilians which were constructed of Nile-mud bricks and all of which have been lost, was built to last. A total of 2'300'000 stones make up the Great Pyramid (Figure 1.2 Left), with limestone used in the outer casing and rose granite used for the Pharaoh's chamber.

Figure 1.2 Left: Pyramid of Khufu, 2520-2494 BCE (photo from http://www.bluffton.edu/). Right: Pantheon, Rome (118-125 AD)

Egyptians were the first society to have created a logistic network for the transportation of stones from the quarry to the designated site, and to have begun shaping the stones with metal tools. Greeks and Romans improved the process of stone extraction and transportation; they considered marble of higher value than limestone or granite, and thus it constituted the raw material of monuments still appreciable today (Figure 1.2 Right). The whole construction process of the great works of the past required hundreds of thousands of men, among which slaves. Frequently, such works were needed to provide man an occupation and preventing rebellions and separatist movements to rise against the authorities. Designers and engineers were not thus acquainted with the concept of safety factors and material reductions. As long as men were available, an over-dimensioning was even sought for.

From the Renaissance, stone started to lose its structural function and began being applied on façades in the form of slabs or tiles. In the past two centuries, the use of stone was exclusive of government buildings, public gathering places, and homes of the wealthiest. Heights were limited, because as the buildings got taller, they required more mass in the base, and openings had to be reduced in size and quantity. A dramatic change in the concept of building structures only occurred as result of the industrial revolution (latter half of 19th century). The ready availability of metal at a low price shifted the way buildings were made: a metal frame constituted the skeleton of the construction and absolved the load-bearing function, while the exterior was now free from the structural role. The concept of cladding was born.

Stone cladding industry started at a slow pace, but it caught up when producers developed new methods of extraction, fabricators invented ways to process thinner slabs, technology made stone machining uniform and faster, and modular production took place. The rudimental anchoring techniques, which required slabs above a certain thickness, and thus made the whole process exclusive for the wealthiest, were supplanted. Modular production meant building prefabricated components reinforced on the back side to decrease construction time and costs. Today, there are numerous fixing systems and stone backing materials to install stone on façades, making this material popular again. In 2008, Italy, Spain, France and UK were the European biggest consumer of finished (67% of EU market) and intermediate stone products (82%), spending a total of € 8.3 billion (CBI Market Survey 2010).

Figure 1.3 SUNY Cortland school cladded with stone veneer (www.stoneply.com)

1.4 Organization of the present thesis

This thesis is organized in seven chapters. The current chapter is a general introduction; in Chapter 2 there is a review of fatigue testing methodologies, and the development of the current cyclic test; Chapter 3 has a description of the physical and mechanical properties of the composite constituents, with an emphasis on the state of the art, if present, of their fatigue resistance. The chapter also contains an overview on sandwich composites. It finally reports the analytical calculation of the stresses on the section, when loaded in four-point bending; the following section, Chapter 4, is about material and methods of the experimental work, while Chapter 5 reports the obtained results. A discussion is made in Chapter 6, and the conclusions follow in Chapter 7.

Chapter 2.

Review of fatigue testing and design of the present experimental work

2.1 What is fatigue in materials?

> *Fatigue is the process of progressive localized permanent structural change occurring in a material subjected to conditions that produce fluctuating stresses and strains at some point (or points) and that may culminate in cracks or complete fracture after a sufficient number of fluctuations.* (Campbell 2012)

Observation of cyclic failure of metallic components occurred in the 1800s in Europe, when railroads and bridges cracked at loads smaller than their failure load. This phenomenon soon became a problem to be accounted for in the design of safe structure and components. Wohler was the pioneer who developed the framework of design procedures, in the form of S-N curves, which still aid dimensioning steel for fatigue nowadays. His graphs represent data of the life cycles sustained by a metal according to the load amplitude at a given load ratio; steels are known to have a fatigue limit, which is the stress under which a steel could endure the load “infinitely”. Later developments of fatigue design accounted for the effect of internal and external factors such as: surface finish, dimension, type of loading, presence of stress concentrators, etc. The S-N graphs are a notable aid in design, but it was only in the early 1900s that sophisticated techniques, in particular the transmission electron microscope, became available to have an increased understanding of the microscopic behavior of materials.

The topic of fatigue in composites and sandwich structures is still being studied, and of difficult generalization. Being a sandwich made of the superposition of layers, the individual behavior as well as its production method influences the behavior in fatigue. Fatigue in metals and unidirectional composites will be introduced, as to show the two approaches to adopt with those materials.

2.1.1 Cyclic hysteresis curve

The shape of a load-displacement curve of the specimen tested in the present work upon loading and unloading is shown in Figure 2.1. When the load is reversed (point B), the load-displacement relationship does not follow a line with a slope equivalent to the initial slope in loading: the slope is higher, because the material deflects less. Once the load is brought back to its initial value, the specimen does not fully recover the deformation, maintaining a residual deformation (difference between A and C). At this point, one fatigue cycle has been performed, and it is defined a hysteresis loop. Figure 2.2 pictures three cycles at increasing maximum load. The area under the curves represents the dissipated energy. After a number of cycles at the same maximum load, the hysteresis loop stabilizes.

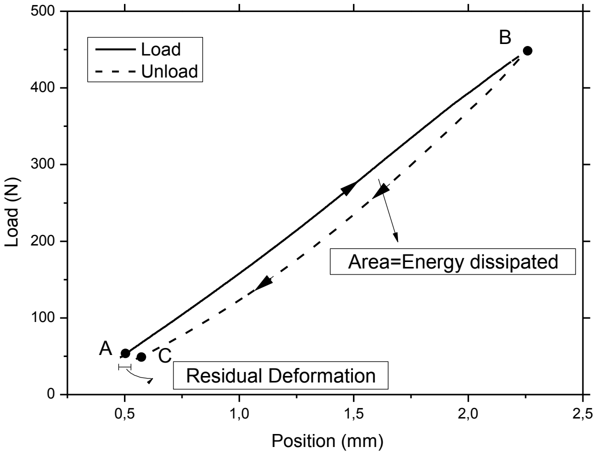

Figure 2.1 Sample hysteresis loop

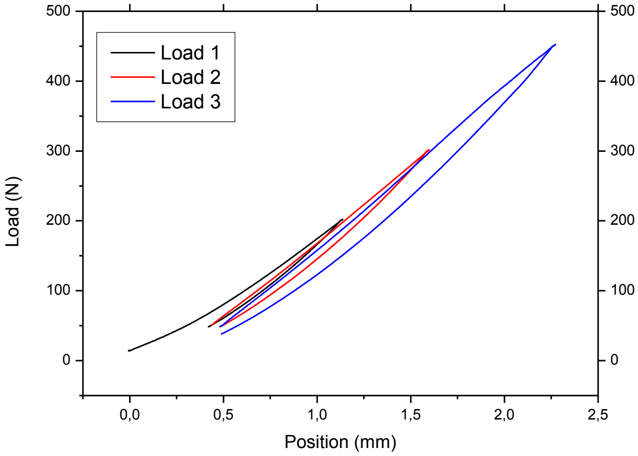

Figure 2.2 Three hysteresis loops at increasing maximum load

2.1.2 Fatigue in metals

Metals are polycrystalline, which means that their structure is an assembly of grains where atoms are arranged in order. Inside grains, which have random orientation, dislocations can move along crystallographic planes of easy slip, once a force is applied. In the grains oriented in a way that slip planes coincide with planes of maximum shear stress, dislocations move and create a one or more planes of new surface material. Upon unloading, reversed slip will occur in the same slip band but in parallel slip planes, due to irreversible processes such as strain hardening and oxide formation. A microcrack initiates along a slip band because this acts as a point of stress concentration. This mechanism is repeated for each loading-unloading cycle and causes crack extension. Slip planes usually occur at the surface of the metal because the constraint opposed by the environment is lower than that opposed by neighboring grains: material is present only at one side. Moreover, the surface is the home of roughness and defects (corrosion pits) which create an inhomogeneous stress distribution, from which a crack is more prone to nucleate. Microcrack growth occurs on more slip planes, and depends on the plasticity (ease at which dislocations move); material structural barriers can stop the crack propagation.

Initial crack growth rate is slow because the crack is travelling over grain boundaries in grains whose slip planes differ, but as soon as growth does not depend on surface conditions, propagation becomes continuous. This stage makes up the most part of crack growth, and the crack growth rate is described by the Paris law. Propagation can proceed by mechanisms such as striation, cleavage, and microvoid coalescence according to the material and to the stage of the fatigue process. Failure for fatigue in metals is always catastrophic.

2.2 Fatigue in unidirectional composites

Earlier studies on fatigue in fiber-reinforced plastics erroneously compared the behavior of the two classes of materials, and developed tests on composites on the basis of what was known from metals. Polymer matrix composites do not possess a crystalline structure, nor can deform plastically; their structure is inhomogeneous and often anisotropic. Unlike for metals, damage in composites is not localized but rather it is a general process. Damage is caused by different mechanisms, each one of which has a development rate, is structure dependent, and may or may not propagate according to the nature of the composite. The most common damage mechanisms are: resin cracking, debonding, and fiber cracking. Accumulation of damage causes overall strength and stiffness reduction, until strength falls below the applied load with catastrophic consequences.

(Talreja 2008) developed fatigue life diagrams for unidirectional fiber reinforced plastics, which, differently from the Wohler maps, predict the failure mode according to the fiber and resin properties of the laminate. These diagrams have the number of cycles on the x-axis and the maximum strain on the y-axis.

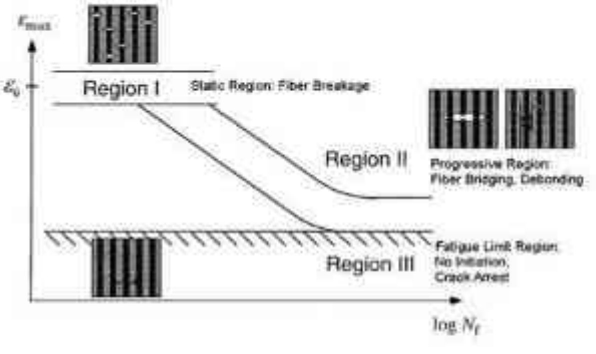

Figure 2.3 Fatigue life diagram (Talreja 2008)

One example of his diagram is shown in Figure 2.3; three regions are indicated:

- Region I is at the composite (or fiber) failure strain; it represents static failure in tension, therefore it is located at small number of cycles and high strains.
- Region II is a region of fiber-bridged matrix cracking, where damage is progressive and the fiber interface plays a role in the transmission of stresses.

- Region III is located below the matrix fatigue failure strain, and signifies matrix cracking. Cracks are bridged by fibers or stopped by interfacial debonding.

The fatigue diagrams are a powerful tool in the interpretation of the results of fatigue tests, and an aid prediction of fatigue response.

An additional difficulty in the study of fatigue in laminates is that their mechanical properties are often sensitive to strain-rate and temperature: this is the case of glass fibers and thermoplastic matrixes. The effect of water exposure is detrimental to the fatigue, because it induces a plasticization of the matrix and weakening of the interfacial bond. Conversely, any treatment improving the interfacial adhesion or processing that reduces matrix crack propagation is likely to be beneficial.

As an example of fiber architecture affecting the fatigue life, (Curtis & Moore 1987) compared the tensile and fatigue strength of CFRP laminates with woven and non-woven fibers. They found the performance of the former materials much poorer, due to additional damage induced by the crossover points and the fiber distortion. Progressive damage has a statistical nature, as well as quality of commercial and natural materials. This variability has to be accounted for because it affects the results of fatigue tests. Variability in composites is even greater than in metals, thus the importance of repeating a test a considerable amount of times.

2.3 Results of previous works on fatigue of composites with cork

Previous dissertations tested the same composite with a non-optimized production method, unlike in the present thesis. The optimization reduced production times and increased the flexural strength. The present work is intended to continue and improve a research previously conducted by (Correia 2016) on the same composite, who aimed at designing a fatigue testing methodology to evaluate the macroscopical effect of flexural fatigue at different temperatures and different initial loads.

A four-points bending test (geometry according ASTM C393) was chosen by the author, because bending is considered the most common type of solicitation of the composite in its applications. The method developed used a mixed control system (Figure 2.4): both extreme displacements and maximum force were imposed on the machine. During each cycle the specimen must reach the maximum force previously imposed, while the minimum force fluctuates, keeping the extremes of deformation constant. In doing so, the problems encountered in pure load control and pure strain control are overcome. Respectively in pure load control the cork viscoelasticity led to excessive deformation amplitudes of the specimen, which could be harmful for the testing machine, while in pure strain an excessive decrease of the maximum load (due to mechanisms of stiffness reduction) never led the specimen to failure. The fatigue test was organized in blocks of 10^5 cycles, with the maximum load increasing of 10% of the monotonic tensile load during each block. The influence of the starting maximum load was also investigated.

The author followed the evolution of a so-called *apparent stiffness* (*D*) along the number of cycles (*N*), given the above-described test. The apparent stiffness is defined as

$$D = \frac{\Delta F}{\Delta l},$$

where ΔF is the force amplitude applied by the testing machine, and Δl the relative machine displacement.

Figure 2.5 shows the machine minimum and maximum displacement along the cycles. As previously mentioned, the imposed maximum compressive load requires the specimen to deform more and more, hence the average deformation of the machine has to increase. Recovery of deformation is function of time for viscoelastic materials such as cork. If the time between two consecutive cycles is not “enough” (less than the relaxation time), the deformation is not recovered, as it happens here.

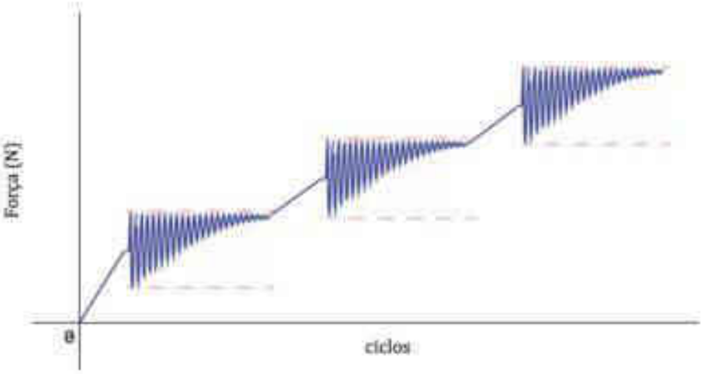

Figure 2.4 The cyclic test used by Correia. Maximum force and deformation range are kept constant. Every 10^5 cycles (one block), the force is increased

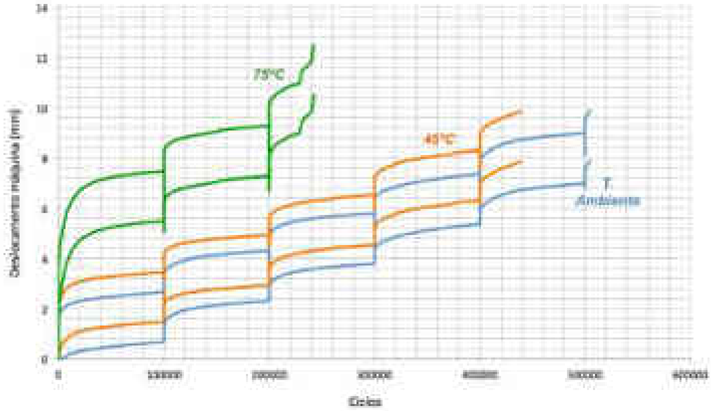

Figure 2.5 Minimum and maximum deformation along cycles for three temperatures: 25°C, 45°C, and 75°C.

2.3.1 Failure

Failure in the **monotonic** bending test (of the non-optimized composite) occurred because of a crack initiated on the stress concentration points below the loading pins on the hard (and fragile) plate (Figure 2.6 left). After failure of the stone component, the layer of resin-fiber in the interface skin-core wrinkles and the cork agglomerate follows this deformation without delamination. Also, no delamination occurs between stone and fiber which indicates a good adherence between different layers of different materials.

In **cyclic** test, the damage is visible both in the hard plate as well as in the core (Figure 2.6 right). It is again assumed that cracks initiate below the point of load application on the stone. When the whole transversal section of the stone has failed, there can be an effect of penetration of the stone edges inside the cork during the cycle. This cutting effect ultimately leads to a 45° crack throughout the core.

Figure 2.6 Left: Failure of specimen in 4-point bending (Gomes 2016). Right: Failure of specimen in cyclic 4-point bending

The work of Correia pointed out that:

- Traditionally, failure criteria require the separation of the specimen in two or more parts. Here, this condition is never reached under constant load cycles, therefore another failure criterion must be determined to declare if a specimen has failed or not. This new criterion could be based, for example, on the reduction of a material property (e.g. stiffness), on the attainment of a certain deformation, or on the initiation of a specific damage mode.
- The calculation of the stress undergone by each lamina is missing. It is possible to calculate it with classical lamination theory, when in the linear elastic regime.
- It is not known what mechanism initiates and propagates the damage until the predefined failure mode. A microscopic investigation of the transversal section at various stage of the fatigue test could clarify this point.

For the scope of this work, the testing method proposed by Correia will not be used.

2.4 Design of a fatigue test

A variety of tests is possible, because of the large number of parameters characterizing the test: amplitude control, frequency, load ratio, loading direction. The available fatigue test standards for common composite materials are listed in Table 2.1.

Table 2.1 Standards on fatigue testing of polymer composites.

Standard	Description	Specimen limitations
ISO 13003	Fibre-reinforced plastics - Determination of fatigue properties under cyclic loading conditions	Fiber-reinforced plastic composites
ASTM D3479	Tension-Tension Fatigue of Advanced Composites	Continuous- or discontinuous- fiber reinforced composites
ASTM D6873	Bearing Fatigue Response of Polymer Matrix Composite Laminates	Polymer matrix composite bearing specimen

As can be observed, to date, there is no specification or international standard to test cyclic fatigue resistance of asymmetric sandwich composites. The closest resource found on the literature was the report by (S. Kneezel & J. Scheffler 2014), which followed the ASTM test by the same authors in (Scheffler et al. 2007).

Fatigue tests are carried out normally at the highest frequency possible to minimize the time and cost of undertaking a fatigue program. There are two issues that must be considered: one is that because of the low thermal conductivity and the high damping factor of reinforced plastics (that, unlike in metallic materials, increases further as microdamage occurs in the specimen) autogenous or self-generated heating occurs. Heating is detrimental to mechanical properties and to the fatigue life (Toubal et al. 2006; Katunin 2012 and many others). The second effect is the rate dependence of the material properties themselves in the absence of the temperature effects.

Increases in frequency in sandwich composites with PVC cores and glass fiber-vinilester faces (Kanny & Mahfuz 2005) led to longer lives for the same stress levels. The author assumed that the temperature increase associated with the highest testing frequency “consumed” the energy provided by the external work, while if no heating occurs (at lowest frequency), the work is entirely converted into strain energy to fuel the damage process.

According to the stress magnitude, the self-heating effect may lead to two scenarios. Below a critical stress value, the specimen temperature increases and stabilizes to a certain amount, being the thermal energy dissipated with the environment equal to the energy generated. In this case, which is characterized by a small temperature increase, autogenous heating does not influence the fatigue process. In the second case, there is not stabilization, and heat dominates and intensifies the fatigue process: the stiffness decreases and, in turn, more heat is generated (Katunin 2012).

From the many factors related to fatigue testing, it appears that there are three prime issues in the choice of any fatigue program. These are:

- the failure criteria to be applied (e.g. fracture, stiffness loss),
- the stress state to be applied (e.g. multi-axial, uniaxial),
- the control mode to be applied (e.g. load, displacement).

2.4.1 Failure criteria

Unlike in metals, in sandwich composites non-catastrophic damage events can occur throughout the stressed volume; therefore, the definition of failure is particularly difficult. The occurrence of one of this damage events may itself define the failure point.

Besides traditional fracture, stiffness loss, and visual appearance have been used as failure criteria. Stiffness is the resistance opposed by the body to elastic deformation.

$$Stiffness = \frac{P_{max} - P_{min}}{d_{max} - d_{min}}$$

Compliance is the inverse of stiffness. *Compliance change* was used e.g. by (Hossain & Shivakumar 2014) in defining different types of failure according to the progression of damage, since each jump in compliance was associated with the onset of a certain type of damage in the fatigue life. *Stiffness loss* along cycles is the ratio between the stiffness of the ith cycle and that of the first cycle.

Using stiffness (or compliance) as failure criteria, failure is declared at a certain percentage of stiffness loss N_α (or compliance gain), where N is the number of cycles corresponding to a α% stiffness loss. Reduction in stiffness can be monitored non-destructively, as opposed to strength reduction, therefore its use is more widespread. Stiffness degradation was also used by (El Mahi et al. 2004) and many others in the literature, to estimate damage and model fatigue life in laminate composites.

Visual appearance is also a criterion for failure for coupons. In fact, in structural applications, a component can be declared unfunctional before having reached the number of cycles correspondent to its end-of-life because of a change in aesthetic properties. (Shafiq & Quispitupa 2006) used as damage criterion the acoustic emission amplitude and energy levels, which correspond to the occurrence of a certain damage event. Table 2.2 lists a review of the literature on fatigue tests on sandwich composites: the control, frequency, failure criterion, cutoff number of cycles used etc.

The failure cutoff for metals is set at $2{\cdot}10^6$ cycles, because the S-N curve has constant slope after 10^6 cycles. Composites material tests should be carried out for a higher number of cycles, because they tend to have lower fatigue life, and their characteristics vary according to fiber and matrix material.

Table 2.2 Summary of fatigue parameters used from researchers in the literature

Reference	Composite	Test	Control	F_{MAX}/F_{US}	R	Freq (Hz)	Outputs	Max Cycles	Failure criterion
(El Mahi et al. 2004)	PVC foam GF epoxy	3pb	load	0,6 to 0,98	0	10	$F_{MAX}/F_{MAX,0}$, $d_{0,max}/d_{max}$		Stiffness reduction
(Judawisastra et al. 1998)	3D foam sandwich	3pb	load	0,65 and 0,8	0,1	1 and 2	Stiffness degradation	10^6	separation
(Hossain & Shivakumar 2014)	Ecofoam + glass vinyl esther	4pb	load	0,7 to 0,9	0,1	2	Damage in compliance between cycles	10^6	separation
(Burman & Zenkert 1997)	foam	4pb	load	0,25 to 0,7	0,5 to -1	2	Change in stiffness / thermal conductivity		
(Sha et al. 2006)	Al foam and metallic face	4pb	load	0,4 to 0,8	0		Deformation energy vs deflection		
(Shafiq & Quispitupa 2006)	PU foam and Carbon-fiber Epoxy	3pb	load	0,7 to 0,95	0,1	2	Acoustic Emission	$5*10^5$	Strength reduction (to 60%)
(Kanny & Mahfuz 2005)	PVC foam and vinylester GF	3pb	load	0,75 to 0,90	0,1	3 and 15			separation
(Ben Ammar et al. 2014)	PVC foam and GF epoxy	4pb	displacement		0,25 and 0,33	5	Hysteresis curve, damping factor, Stiffness degradation	10^4	separation
(Kulkarni et al. 2003)	PVC foam and GF epoxy	3pb	load	0,6 0,65… 0,9	0,1	3	Stiffness degradation	10^6	separation

2.4.2 Investigation of damage

One of the aims of the thesis was the investigation of the processes that lead to fatigue damage. Therefore, a summary of microscopic characterization techniques used by investigators will follow. The monitoring techniques are distinguished in 2 classes: destructive and non-destructive. As obvious, the latter can only be used post-mortem.

Optical microscopy is the easiest and most versatile technique of non-destructive damage inspection. It is performed in nearly all studies concerning fatigue and consists in the observation, at magnifications that vary according to the objective of the study, of the cross section of the specimen. In flexural tests, photographs are taken in the section normal to the width. Unless performing the cyclic test inside a SEM apparatus, the magnification limit is in the order of the wavelength of light. SEM observations on the specimen belong to the destructive-methods category, therefore are done only at the end of the test.

(Tsai et al. 2000) used cyclic tests stopped at 5 fractions of the total fatigue life, at maximum stress equal to the fatigue limit strength of each plate. After the unloading, specimens casted in epoxy resin were observed using metallography. Photographs taken at the longitudinal section can show the onset and progression of the damage.

(Takeda et al. 1995; Takeda & Ogihara 1994; Montesano et al. 2014) used the replica_technique to monitor transverse crack density. During the fatigue tests, the testing machine was periodically stopped and the polished edge surface of a specimen was replicated on a replica film (acetyl cellulose film) with methyl acetate as resolvent. The film was then observed by optical microscopy. (Montesano et al. 2014) also used scanning electron microscopy (SEM) for post-*mortem* investigation. Plastic replica technique involves softening a plastic film in a solvent, applying it to the surface, and then allowing it to harden as the solvent evaporates. After careful removal from the surface, the plastic film contains a negative image, or replica, of the microstructure that can be directly examined in the light microscope or, after some preparation, in the electron microscope (Marder 1989).

(Song et al. 2016) used **digital image correlation** software to investigate the apparent maximum tensile strain fields on the surface of the specimens, which is strongly correlated with the damage.

During testing an infrared **thermographic camera** was used to observe the temperature changes in the specimen by (Burman & Zenkert 1997; Adam & Horst 2017). The study showed that the testing machine induces increases in temperature in the specimen near the rollers.

Also, **Acoustic Emission** is a technique used for evaluating damage evolution (Ben Ammar et al. 2014; Shafiq & Quispitupa 2006; Gao et al. 1999; Yu et al. 2015), in particular the onset of cracks, which differ according to the composite materials and loading cycles, and the accumulation of those cracks. Any form of damage (debonding, matrix cracking, delamination and fiber fracture) can give rise to an acoustic emission signal. Relating the output signal to the various possible damage modes permits monitoring of damage over cycles. does not define the micro- crack before stress is applied

Penetrant enhanced **X-Ray tomography** enabled monitoring of through-width damage in fiber reinforced plastic laminates in (Gao et al. 1999) to describe the spatial distribution of matrix cracks and delamination.

Optical inspection, replica method, thermographic inspection, acoustic emission are non-destructive. SEM inspection can only be done destructively.

Chapter 3.

Mechanical and physical properties of the materials composing the layers

Here, literature on cork, limestone, and glass fiber reinforced-plastic has been reviewed. Their physical structure was reported together with notions of their mechanical behavior; cork's fatigue behavior has never been described in the literature, therefore a description of foam's fatigue was introduced instead.

3.1 Cork from *Quercus Suber*

Cork is a natural cellular material produced in every tree by the cork cambium, a thin cylindrical layer of cells located under the epidermis of the plant (Figure 3.1). The cells of the cork cambium, as well as those of the vascular cambium, have merismatic activity: they are responsible for the growth of the tree, both axially and radially. The function of the cork layer is to protect the tree both from pathogen attack and from desiccation.

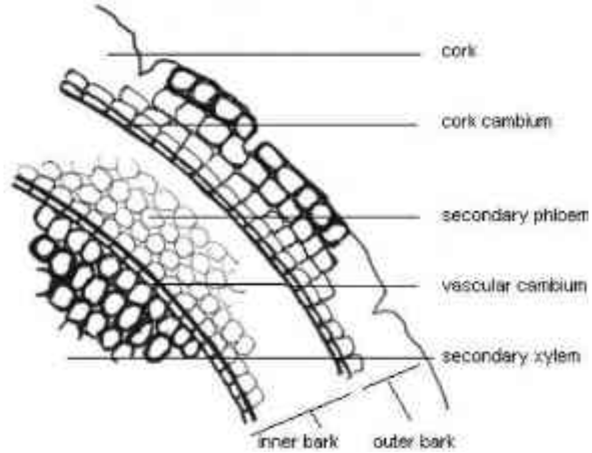

Figure 3.1 Location of the cork tissue on a tree (www.garden.org)

Despite being produced by every tree, all the cork commonly known for its commercial uses comes from *Quercus Suber*, or cork oak. This tree flourishes only in specific regions of the Western Mediterranean (Portugal, Spain, Southern France, part of Italy, North Africa) and China, and requires a great deal of sunlight and a highly unusual combination of low rainfall and high humidity (Silva et al. 2005). The unusual thickness of cork from *Quercus Suber* is probably a survival strategy in response to the environmental conditions where it grows, where forest fires are not rare. Cork acts as an insulating barrier to protect the tree's stem and branches from the heat and the flames; after the fire, the tree can regrow from those branches (Pereira et al. 2008).

The extraction of cork is done manually and consists in cutting and pulling out of the tree large rectangular planks. Since the most added value from raw cork comes from the production of wine stoppers, the thickness of cork planks is dictated form its industrial use and must be of at least 27 mm; this corresponds to an over-bark tree diameter of 22 cm. Therefore, in Portugal, after cork oak has reached maturity, it is harvested every 8-10 years, which is the time it takes for the tree to reach the desired size. The time at which maturity occurs depends again on the growing conditions, but it can take from a minimum of 20 years to 40, in less favorable environments. After maturity, cork coming from the first harvest is called *first reproduction* or *virgin* cork. The morphology of first and second reproduction cork is more irregular compared to cork from the third reproduction on, and its quality is not high according to the standards of wine stoppers producers. Therefore, it has other uses, as will be discussed later.

Tree growth is not constant over a year, nor uniform throughout the years between two harvestings (Figure 3.2 Left). The active growth period is between March and November, after which the tree enters dormancy and no increase in thickness occurs. During the active period, radial growth rate gradually increases reaching its peak in the month of July, after which it decreases until a stop (Figure 3.2 Right). The variability in cork's growth is reflected in its structure (Figure 3.3). In fact, in periods of higher growth the cork cell's walls are thin and fragile, while in the early or late season cell walls are thicker, and cells generally bigger. Due to the cells' lower resistance to tensile forces cork is harvested in the periods of highest merismatic activity, namely July and August.

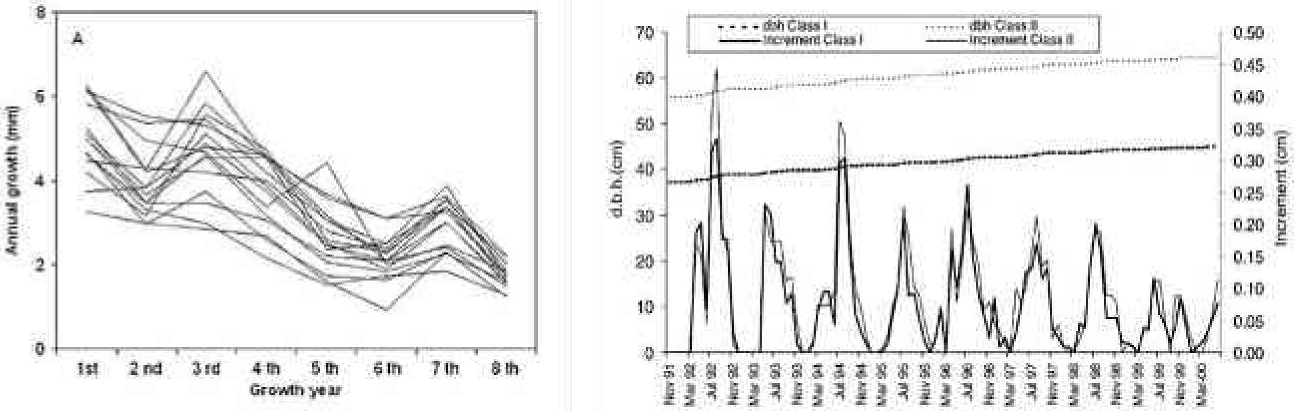

Figure 3.2 Left: annual increments of cork during 8 years of growth after stripping (location: Benavante, Portugal) (Pereira 2011). Right: diameter at brest height (d.b.h.) and monthly diameter increment in period from November 1991 to March 2000 (Costa et al. 2003)

The price of cork is the biggest disadvantage, when compared to its alternatives, such as plastic foams.

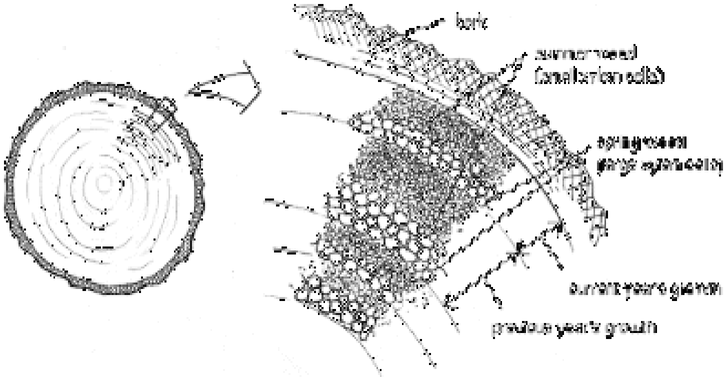

Figure 3.3 Morphology of the tree's annual wood tissue growth.

3.1.1 Morphology

The coordinate system used in the present work when referring to tree's direction is that developed by wood anatomists, and shown in Figure 3.4. It can be thought as a cylindrical coordinate system, where axial direction is along the tree's stem growth, radial direction is in a plane perpendicular to the axial direction and corresponds to growth in diameter, and tangential direction is orthogonal to both axial and radial.

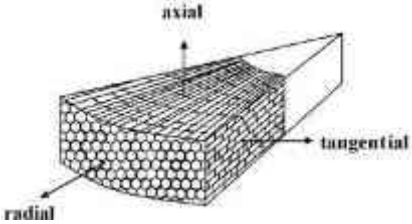

Figure 3.4 Coordinate system of the cork's cells.

Sections are named as follows:

- Transverse section is normal to axial direction.
- Tangential section is normal to radial direction.
- Radial section is normal to tangential direction.

Natural cork is made of a quite regular arrangement of closed prismatic cells that depart outwards along the radial direction. Cork cells are generally described as n-gonal prisms with bases normal to the radial direction and height along the radial direction. The average number of prisms' faces is 6 (Gibson & Ashby 1997; Pereira 2011), and dispersion around the average is low, highlighting a large homogeneity of cell shape. In the radial direction prisms are stacked base-to-base, base dimensions being equal to the dimension of the mother cell in the cambium.

Radial and transverse sections are similar; their structure resembles a brick-wall with all rows roughly parallel. Prism bases in adjacent rows do not coincide, but are staggered. It is common practice in literature to consider these sections as equal, thus the properties of cork being transversely orthotropic. An important feature of cork cells is the presence of wall corrugations in the lateral faces of the prism, which can be seen from radial and transverse sections. The number and amplitude of the corrugations vary. The bases of the cells are not corrugated. Corrugation determines mechanical properties.

3.1.2 Cell dimensions

The average values of cell dimensions are reported in Nevertheless, cell dimensions vary. The highest source of variation is the month when they were formed: earlycork cells are larger and have thinner walls while latecork cells have thicker walls and smaller prism height (dimensions reported in Table 3.1). The former cells are formed when the physiological activity of the tree is its highest, thus the cell growth and the number of cells born is high compared to the period before dormancy. Thick-walled latecork cells show higher rigidity in comparison to thin-walled cells, and show no undulations. Cell dimensions also vary from tree to tree, according to the location and environmental conditions (e.g. amount of precipitations) undergone by the trees. Cork cells are up to three orders of magnitude smaller than metallic or polymeric foam cells.

Table 3.1 Geometrical dimensions of early cork, late cork

		Early cork	Late cork
Height	(µm)	30-40	10-15
Base edge	(µm)	13-15	13-15
Wall thickness	(µm)	1-1.5	2-3

Irregularities

The most important source of cork heterogeneity are the lenticular channels, which run radially across the planks to ensure gas exchange between the below-cork tissues and the exterior. They are formed together with the cork cells. They visually appear as small rounded spots in the tangential sections and as radially aligned strips in the other sections, the so-called cork porosity (Pereira 2015). They are usually referred to as porosity and are closely related with the determination of macroscopic quality of planks. Commercial cork stoppers are more valuable, the less porosity they contain. Number and size of pores vary among samples as well as among different areas of the same plank.

Cork tissue includes occasionally lignified woody type cells, which are denser and harder than cork tissue and stand out because of their dark color. They are called “nail” by the cork industry and constitute a negative factor for cork quality.

Irregularities also arise due to the alternation of early- and late-cork, which determines less or more dense cork areas. There can be stresses in tangential direction, which cause cell corrugation and collapse, corrugation bands, and fracture.

3.1.3 Extraction and production of commercial cork

After manual cork stripping, the curved planks are stored in a field forming a pile, for a storage time varying from few weeks to a year, during which the content of humidity of the planks decreases until it reaches 6-10%. A variable period of mill storage follows; it was found that storage time does not affect cork’s final quality.

The byproducts obtained in the cutting of stoppers, reproduction cork of low quality, virgin and secondary cork and every other waste goes to trituration and granules used for agglomerates. Quality of planks is determined made after the boiling process according to the thickness and porosity (or other discontinuities).

Boiling is done in water for one hour, the process occurs in a closed autoclave with filters used remove suspended solids from the water. The objective of boiling is to flatten the planks, relieve growth stresses in cells, decrease of corrugation of cell walls, reduce the porosity and increase in uniformity of the cellular structure. Cells expand radially of 15%, in other direction of 6%. It is common belief that the boiling process is done to sterilize the cork planks, but it is not the case.

After water boiling, planks are left to air dry for 2-3 days, during which the moisture content decreases to 14-18%. Afterwards, there is a manual selection step to separate the planks per quality grade.

Agglomerates

Raw materials include:

- Byproducts from processing line of production of stoppers; have been boiled
- Raw cork that hasn't been boiled.

A first milling operation is done in hammer type mills; subsequent size reductions are done in knife or disc grinders. Separation by density allows sorting out particles with wood inclusions. The final product corresponds to granulates calibrated by particle size and density.

Agglomeration is carried out either using resin as an adhesive, or without any adhesive. In the first case, the adhesives can be either thermosetting polymers or thermoplastic, such as polyurethanes. Flooring and surfacing agglomerates are produced from rectangular prismatic blocks that are laminated into boards. Granules are mixed with the adhesive and plasticizers and fed to a continuous mat that is pressed and heated in a hot plate press. Adhesive content is usually 3-8% and polymerization temperature and time depend on the adhesive (from 100 to 150°C, during 1-20 h). Boards of different densities are achieved using selected distributions of granulometric fractions and applying less or more pressure.

At the cellular structural level, the compression of the cork particles during agglomeration causes densification of cells at the grain boundary, with cell collapse and corrugation.

3.1.4 Cell wall and chemical properties

Every cell is surrounded by a cell wall, and its interior is filled with a gas. Cells join at their faces due to deposition of lignin (biopolymer). We have been referring to cell wall at a microscopic scale, considering it a uniform solid. Investigating it at lower scales, its layered composite structure can be appreciated (Figure 3.5 left). First, there is a primary wall containing cellulose and pectin; the other layers grow inward from the primary wall, and different cells thus are glued externally by the lignin polymer which connects the primary walls. The secondary wall is the thickest. From TEM images it's possible to see alternating electron-dense and electron-translucent layers, or lamellae (Figure 3.5 Right). A tertiary wall makes the boundary from solid wall and cell lumen. The cell walls are therefore double walls, because constituted by the joining of two single cells walls.

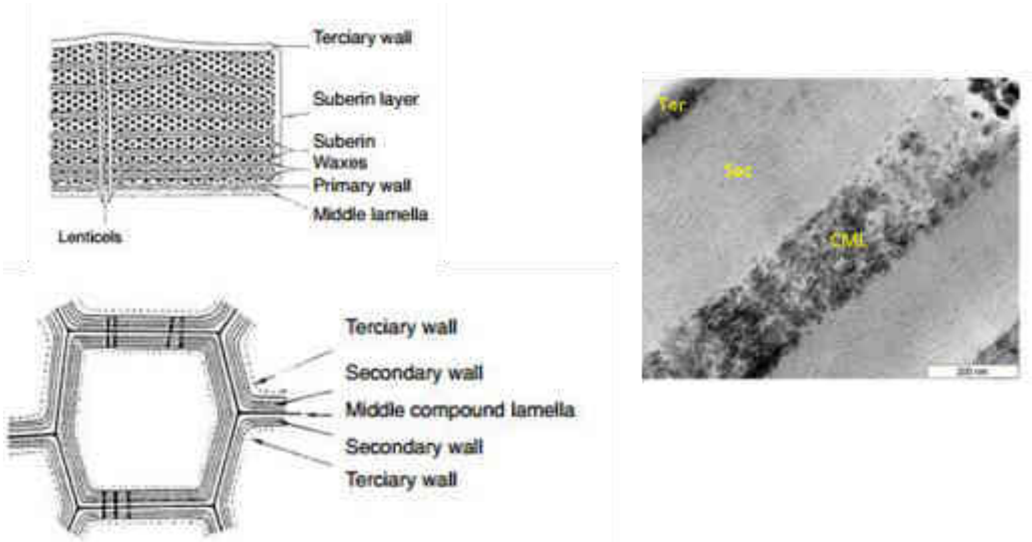

Figure 3.5 Left: representation of the layers inside the cork cell's walls (Gil 2007). Right: TEM image of secondary and tertiary walls (Graça 2015).

Cork's cell wall is made of structural and non-structural components, also called extractives. Structural components are polymeric, insoluble and without them the walls would collapse; extractives can be solubilized in solvents, don't have a structural function and thus are not important for the determination of mechanical properties. The members of the first category are suberin, lignin, cellulose and hemicellulose. In comparison with wood, whose structural components are lignin (20-35%) and polysaccharides (70-80%), cork is mainly made of suberin (50-60% of total material) followed by lignin (about 25%), cellulose and hemicellulose (20%). Extractives make up about 17% of the total dry mass. The amount of lignin is similar in both. Suberin is the characteristic chemical components of cork cells in every tree's bark and of other tissues found in underground plants. It determines its overall behavior.

The topochemistry of cell walls, i.e. the structural arrangement of the chemical components, is still a subject of research, but it is possible to make a good guess of the walls' structure by comparing the microscopic observations with chemical analysis and the mechanical behavior. The most believed theory is that light (translucent) lamellae are suberin-rich, while dark shaded (electron-dense) lamellae are constituted by lignin and polyphenolic components. Between the two, there are strong covalent bonds. The middle lamella is made of lignin, hemicellulose and pectins, while the tertiary wall is made of hemicellulose and cellulose.

Lignin is a rigid and hard molecule with strong bonds and a 3D structure made of a great number of aromatic rings. The aromatic fraction make the molecule amorphous. Its structure is branched and very complex. It is supposed to provide structural rigidity to the cell acting as a scaffold for the more flexible suberin component; in fact, when cork is delignified, cell walls collapse and become a completely flexible layer.

3.1.5 Observed mechanical properties

Cork is an anisotropic material, since its structure is different in the radial, tangential and axial directions. Therefore, researchers have always reported cork's mechanical properties differentiating on the three directions. Although it is effectively possible to observe different behaviors in compression, tension, and bending, the stress-strain trend in the three directions is equal, and the difference in mechanical properties is not very large. Compression and fatigue behavior of cork will be described hereafter.

a. Compression (and recovery)

The stress-strain curve in compression (Figure 3.6) shows three stages:

- Up to a strain of about 5%, there is a linear relationship between stress and strain, which corresponds to elastic deformation of the cells.
- After the initial stress rise, there is a plateau for the stress until strains of about 70%. In correspondence of the weakest regions, the cell walls start to buckle and collapse. The buckling then gradually affects the whole specimen.
- For strains above 70%, there is a sharp increase of stress slope, corresponding to the densification of cork and the contact between opposite faces of cells.

Compression does not cause failure of the cells, even in the densification phase; fracture is observable only when applying tension loads. Cork's strength in the radial direction is higher than in the other directions. Higher cork density, thus a higher proportion of solid material results in an increase in the Young's modulus, and the energy absorbed during deformation increases with cork's density. A study on compression of cork agglomerate shows a trend similar as that observed in natural cork (Jardin et al. 2015).

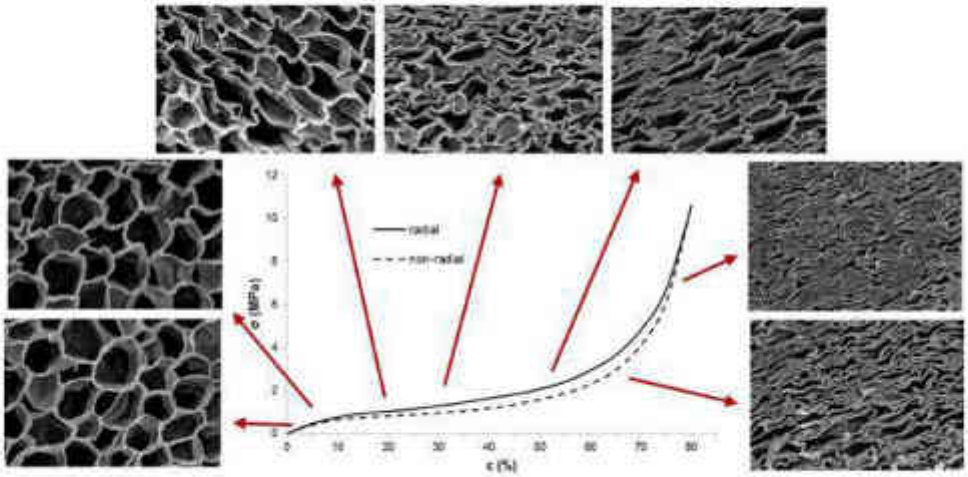

Figure 3.6 Compression curve of natural cork (Pereira 2015)

Complete recovery of dimensions after unloading only occurs in fully elastic materials. Cork shows an instantaneous recovery of dimensions almost to its initial size, the elastic recovery, and a recovery along time after unloading, the viscous part. The unrecovered deformation is always very low. Initial dimension recovery is associated with the unfolding of buckled cell walls and occurs quickly: it has been shown that after 50% strain, 50% of the deformation is recovered after the first day, almost 70% in two days and recovery was almost total after 15 days. Recovery of cork with lower density is higher than in higher densities, especially for compression in the radial direction. It has thus been proposed that the permanent deformation being associated with deformation of lenticular pores (Anjos et al. 2014).

When the dimensions of cork particles are reduced, e.g. in granules, there are many open, through-cut cells, therefore the external surface increases and the number of closed cells decreases. It is interesting to determine below which dimension cork loses its "cork-like" behavior. It has been inferred (Pereira 2015) with statistical reasoning that in order to keep a cork-like behavior in a composite, the minimum amount of cork should be of 72%, when mean suberin value is 52.8% in mass of structural components.

b. Fatigue of foams

There exist no specific studies on the fatigue resistance of cork, therefore a review of the cyclic properties of foams will follow, due to the structural similarity with cork.

Foams – plastic or metallic – are generally used as the core of a sandwich, where they are subjected to shear stresses, but very few literature exists on their shear behavior. Aluminum open- and closed-cell foams were tested by (Harte et al. 1999) in tension-tension and compression-compression fatigue, at constant load. In tension fatigue, foam specimens were reported to break at constant value of strain. The breaking mechanism was associated to cyclic ratchetting and low cycle failure of cell edges. For compressive tests, the strain rate, initially constant, increased abruptly at a strain value of 2%. This was associated to the formation of localized crush bands, in closed cell foams, and uniform straining in the open cell foams. Inside the crush bands, cell edges were broken at low cycles; cell walls fragmentation was confirmed by a drop in measured electrical resistance along the cycles.

Compression, tension, and shear fatigue tests on closed cell Rohacell foam were performed by (Zenkert & Burman 2009), together with monotonic tests. Quasi-static tests on foams of different densities can be normalized with respect to the density, showing excellent agreement in tensile strength, elastic modulus, and fracture toughness, but not in compression and shear strength. In static compression, lower density foams failed for cell buckling, higher density foams for formation of plastic hinge. Also tensile S-N curves can be normalized with density, and collapse into one generic S-N curve, showing that the tensile failure mechanism is cell size and cell wall thickness independent. The compressive strength, for lower density foams, was lower than the tensile strength. Tests in compression fatigue showed formation of a shear band when a 2% permanent strain was reached. In the shear band, foam cells collapsed, while the surrounding cells were unbroken. Fatigue tests in shear showed different failure modes according to the foam density: at lower density, shear and compression have the same mechanism (cell buckling); at intermediate density, shear and tension showed same slope in S-N graphs, therefore their failure mode should coincide; high density foams exhibit the same failure mechanism in all load cases, because their S-N curves overlap.

(Huang & Lin 1996) modeled the effect of cyclic tensile-compressive stresses (with $R = -1$) on cellular materials. They concluded that fatigue life is controlled by the stress concentration factor at the cell wall, thus the number of cycles before rupture of the cell wall material determines the growth rate of a fatigue crack. Considering that fatigue crack propagation rate of the solid cell walls follows the Paris law (refer to (Huang & Lin 1996) for symbol explanation),

$$\frac{da^*}{dN^*} = A^*(\Delta K_1^*)^{m^*},$$

three cases were studied and modeled: a) a macrocrack is already present, b) high cycle fatigue, and c) low cycle fatigue. High cycle fatigue occurs when the maximum tensile and compressive stresses are below the yielding strength of solid cell walls. In all the cases, the same law applies: but the equation for A* differs.

A* depends on cell size, on relative density ρ^*/ρ_s of cellular materials, and on fatigue parameters of solid cell wall materials. m* only relates to fatigue parameters of solid cell wall materials: m for microcrack propagation, α for HCF., and β and n for LCF. The above equation suggests that the cyclic stress intensity range to yield constant macrocrack growth decreases with decreasing relative density of foams at a constant macrocrack growth rate.

3.2 Limestone

Limestone owes its popularity as a building material to the great abundance on the Earth's crust, the ease of processing, and its uniform appearance. In this paragraph, there follows an introduction of physical and mechanical properties of limestone with reference to its behavior under cyclic loading.

3.2.1 Physical characteristics

Limestone is a rock formed by sedimentation and diagenesis of calcium carbonate, in a process that started in the Precambian era (more than 600 million years ago). It is microstructurally made of grains, a matrix, and a certain number of defects such as pores, cracks and grain boundaries. Its composition manly features $CaCO_3$, $MgCO_3$, various amounts of silicates, metal oxides, and other impurities. A limestone is said to be dolomitized as magnesium ions are integrated within the calcite matrix, magnesium substituting for calcium on a one-to-one atomic basis. Most commercial limestones come from *organic* deposition, i.e. from shell and skeletons (bioclastic limestone) or carbonate secretions of marine organisms (biochemical limestone). *Inorganic* precipitation of minerals from sea and inland waters has also been possible (non-clastic limestone), but consists of a very small percentage of limestone quarries. Initially an incoherent material, calcium carbonate becomes a rock through chemical, physical and biologic processes which produce cementation, crystallization and sedimentation of the fragments.

The distribution of grain sizes affects the texture, and ranges from mudstone (mainly calcitic mud with few coarse grains) to grainstone (mainly coarse grains with little mud cement). The amount of porosity, density, composition, color, grain size and shape are a result of the deposition and diagenetic processes and determine all the types of limestone present. There are many ways of classifying limestone, according to its grain size, texture, type of impurities and carbonate content.

3.2.2 Characterization Techniques

A list of techniques for mineralogical, chemical, and structural characterization is provided in this section.

TGA. From the decomposition temperature of its compounds, when heating a limestone sample in a stream of CO_2 gas, it is possible to determine its mineralogical structure. In particular, as the CO_2 bound to $CaCO_3$ and $MgCO_3$ evolves at different temperature ranges, their quantity can be determined.

XRF and **XRD** are used for elemental composition. Quantitative values are obtained by comparison with a calibration curve.

Petrographic determinations of mineralogical composition were carried out by **optical polarized microscopy** (OM) on polished thin sections using a polarizing microscope (also see Tucker 2001). **SEM** observations are also performed to study grain shape and size, topography.

Fluorescent microscopy was used to observe the initiation and propagation of new microcracks in bohus granite under cyclic loading by Åkesson et al., 2004.

Transmitted ultrasonic waves using thorough three-dimensional ray path coverage were used to assess the development of microcrack damage in a granite cylinder subjected to uniaxial cyclic loading (Chow et al. 1995). The change in velocity of ray paths indicates the increase of boundaries within the material, which is a consequence of damage formation.

The crack activities in stone failure tests can be monitored via the acoustic emission (**AE**) technique, which detects the occurrence of elastic waves during loading.

(Zabler et al. 2008) applied X-ray CT to limestones samples in compressive loadings until a progressively increasing maximum load. The output is a 3D image in which, according to the sample size, the resolution varies until a minimum of 8-10 µm, which is enough to image grains, pores, cracks, and other discontinuities. In contrast to planar imaging methods, X-ray tomography data quantitative analysis of the fractures using 3D image analysis.

Digital Image Correlation permits to obtain displacement and strain fields on the surface of materials providing full-field, real-time, online and non-contact measurements.

3.2.3 Mechanical properties

Due to their strongly heterogeneous nature, experimental and analytical characterization of the elastic properties and fracture strength of rocks has high variability. The bulk behavior of many rocks under stress is controlled by the local distribution of flaws, fossils, inclusions, cavities, grain boundaries, mineral cleavage planes and micro-cracks. In addition, in the case of monomineralic and some crystalline rocks, the flaws may not be apparent until stress is applied.

The properties generally calculated are: density, porosity, tensile strength, compressive strength, flexural strength. Elastic constants vary with the porosity, fluid type in the porosity, and the mineral composition of the rock.

Limestone samples tested in unconfined compression (Stowe 1969) reported elastic behavior up to failure, which occurred by vertical splitting. Their strength and axial strain increases with higher loading rates. The reported tensile strength is about 9 times smaller than the compressive strength.

Table 3.2 Mechanical properties of limestone. (1) is from reference (Stowe 1969)*; (2) is from reference* (Pápay & Török 2010)

	Compressive strength (MPa)	*Young's modulus (GPa)*	*Tensile strength (MPa) (2)*
Slow (1)	7.70	77.4	-
Rapid (1)	18.7	72.1	-
Medium-grained limestone	-	-	2.44
Fine-grained limestone	-	-	1.32

3.2.4 Crack propagation in limestone under cyclic loading

a. LEFM in stones

Linear elastic fracture mechanics (LEFM) developed a mechanical model for the evolution of fracture that ultimately led to the identification of the fracture toughness (or critical stress intensity factor, *K*) for each fracture mode (opening, in-plane shear, out-of-plane shear), a material property to be used in a failure theory. LEFM was developed to be applied in metallic materials, and while some of its principles are applicable to stones, there exist large differences between the two classes of materials both in terms of material response and engineering application. Metallic materials always have a plasticity zone formed by shear stresses at the crack tip, while in stones the inelastic response takes the form of microcracking at the crack tip due to tensile stress. Although this theory is based on linear elasticity and is directly related with the Griffith theory, plastic flow and other nonlinear behavior can occur on a small scale without affecting its predictive success (Rossmanith 1983).

LEFM states that every material contains defects, which are the reason why the experimental mechanical properties are lower than those predicted from strength of atomic bonds, and why a scattering in the value of those properties exists. A defect, or crack, is defined as a line across and/or along which the displacement field exhibits a discontinuity. At the extremity of the cracks, the stress field experienced by the linear elastic body is amplified, and varies according to position coordinates (r, θ), and the factor K_I. The stress fields, reported in Eq. 3.1a-c, are shown to control crack growth and crack path stability.

$$\sigma_x = \frac{K_I}{\sqrt{2\pi r}} cos\frac{\theta}{2}\left(1 - sin\frac{\theta}{2} sin\frac{3\theta}{2}\right) \tag{3.1a}$$

$$\sigma_y = \frac{K_I}{\sqrt{2\pi r}} cos\frac{\theta}{2}\left(1 + sin\frac{\theta}{2} sin\frac{3\theta}{2}\right) \tag{3.1b}$$

$$\tau_{xy} = \frac{K_I}{\sqrt{2\pi r}} cos\frac{\theta}{2} sin\frac{\theta}{2} cos\frac{3\theta}{2} \tag{3.1c}$$

K_I is defined as

$$K_I = \sigma\sqrt{\pi a}Y, \tag{3.2}$$

where σ is the far-field tension, a is the crack half-length, and Y a geometrical factor. The failure criterion states that Mode-I fracture initiates when K_I reaches a critical value K_{IC}, at which point crack propagation cannot be stopped. The same criterion was expressed by Griffith using thermodynamic considerations (Griffith 1921). When cracks grow, they start to interact, thus the stress intensity driving crack growth increases and leads to instability and final failure.

Crack tips are never perfectly sharp and nonlinear behavior is known to take place in the immediate vicinity of the crack tip in even the most brittle materials. The inelastic behavior at the high stress levels near a crack tip is usually plasticity in metallic materials which gives rise to a plastic zone with finite stresses. In stone this inelastic behavior is often manifested by micro-cracking and a zone of micro-cracking forms at the crack tip.

b. R-curves and toughening mechanisms

In the case of ideally brittle materials, the fracture toughness is independent of the crack extension Δa. Many ceramics, though, show a different behavior, where the energy term inhibiting crack growth increases with increasing crack extension. The energy for crack propagation is dependent on the crack's size, therefore propagation is not described by a single value of K_{IC}, but by $K_{IC} = K_{IC}(a)$.

In the propagation of fatigue cracks, two mechanisms are competing and ultimately determine the outcome: *intrinsic* microstructural mechanisms, and *extrinsic* crack-tip mechanisms. The formers act to promote crack growth *ahead* of the crack tip, they are a property of the material and thus independent of the crack length; intrinsic forces are the driving force to propagation. Extrinsic mechanisms, conversely, shield the crack and provide a resisting force to crack extension: they are responsible for the R-curve behavior. Examples of extrinsic mechanisms are crack bridging, the creation of inelastic zones around the crack wake (microcrack toughening in stones) that impart closing tractions on the crack surfaces. Brittle materials are toughened by the latter class of mechanisms.

c. Subcritical crack growth (SCG)

In the presence of a crack of length below the critical value for propagation, it is still possible, under application of a constant or cyclic load, to observe crack growth due to time-dependent processes acting at the tip of cracks. SCG in stones can be caused by different mechanisms, such as stress corrosion, diffusion, dissolution, ion exchange and microplasticity; it is defined as the increase of crack length over time and calculated as

$$v = \frac{da}{dt} = f(K_I). \qquad (3.3)$$

In some cases, a threshold exists below which no growth is found (K_0), the crack is said to be dormant. The Paris' law plot of crack growth for ceramic materials in log-log graph (for example Figure 3.7) has 3 regions: a linear region, a plateau, and a further increase until unstable growth.

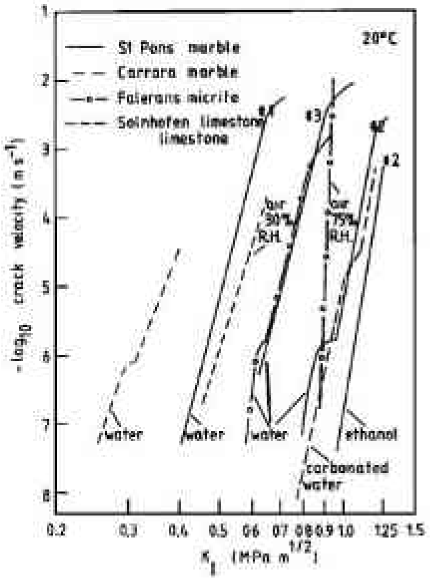

Figure 3.7 Subcritical crack growth for marbles and a limestone (Atkinson 1984)

There is a distinction to be made between SCG due to static and to cyclic fatigue. In the last case, the crack growth rate is larger and lifetime shorter than that from constant load tests (Rossmanith 1983).

The basic mechanism of subcritical crack extension in ceramics should be the same under constant and cyclic loading (time-dependent breaking of atomic bonds). The observed differences have to be traced back to the different stress situation at the tip of a crack. Stress is characterized by the stress intensity factor and by the R-curve behavior. Crack shielding is different in the two loading cases: in fatigue, the R-curve behavior does not affect the fracture toughness as it does in creep tests. Worse than that, ceramic materials with increasing R-curve show a shorter fatigue life than those without R-curve. During cyclic loading the crack surface interactions can be reduced by the cycles. Contact areas are deteriorated due to sliding of crack borders, therefore bridging stresses (which hold the material together) are diminished and propagation happens faster (Munz & Fett 1999).

(Erarslan 2016) studied the micro-mechanical and micro-structural dynamics of sub-critical crack growth and strength variation in notched stone specimens under mechanical loading without corrosive chemical environment. In stones, the crack tip non-linear process zone is caused by the initiation and growth of the microcracks in the immediate vicinity of a crack tip. This zone is called fracture process zone; microcracks form because the maximum principal stresses reaches the ultimate tensile strength of the stone. There is observation of ultimate failure load reduction because of stone fatigue, being the reduction the highest for the highest maximum stress loading (43% reduction K_{IC} at 40% F). Cyclic loading had a significant effect on stone strength, with continuous accumulation of irreversible deformation up to failure.

Damage mechanism in cyclic loading as compared to monotonic loading is also different: the accumulation of plastic deformation before failure under cyclic loading was much greater. This shows that the development of micro-cracks causes permanent deformation. Observation of crack surfaces of failed specimens in cyclic loading showed particles and dust inclusions, while in monotonic the surfaces are clear. This is another evidence of microcracking in the FPZ: under cyclic loading grains cracked along the boundaries (intergranular) and not intragranularly. The dust observed is probably due to grain pull-out and decohesion. In statics, fracture is brittle and occurs along cleavage planes, as observable in SEM.

3.2.5 General stone behavior in cyclic loading

Research on cyclic behavior of stones started in the early 1970s driven by the needs of the mining industry of predicting the effect of percussive drilling and the of vibrations generated by blasting. At the present day, though, it is still unclear how damage evolves throughout cyclic loading in stones. (Peng et al. 1974) made a comprehensive study of the effect of cyclic loading on limestone both in compressive, tensile, and tensile-compressive loading. The results showed a different behavior of limestone in compressive and tensile loading, as consequence of different mechanisms that are involved in both cases. The area inside the stress-strain hysteresis loop defines the energy dissipated within each cycle by the material, owing to internal damping.

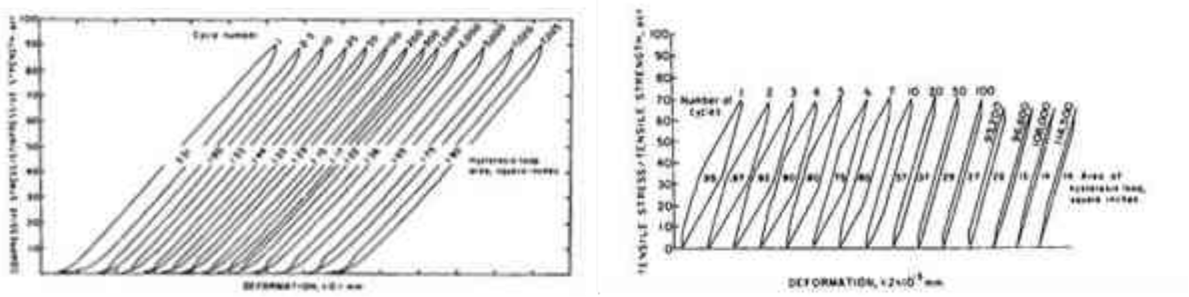

Figure 3.8 Hysteresis loop for limestone under cyclic compressive (left) and cyclic tensile (right) loading (Peng et al. 1974).

In cyclic compression, the area of hysteresis loop (Figure 3.8 left) decreases after the initial cycles, until it reaches a steady value; before failure, the area increases sharply. For cyclic tensile lading, the area of the hysteresis loops (Figure 3.8 right) also decreases at the beginning of cyclic loading, but as the specimens approach failure, there is no increase in energy absorption and failure is instantaneous. For the mixed loading tests, the behavior is intermediate, and fatigue life is much shorter than in the previous cases: after an initial loop area reduction, the energy absorption stabilizes; right before failure, the maximum deformation for each tensile half-cycle stays constant, while for the compressive half-cycle it increases exponentially. Both in cyclic compressive and tensile loadings, the fracture mode observed was similar to the corresponding static mode. When there is stress reversal, fracture happens rapidly; the tensile cycle generates crack propagation in the direction perpendicular to the loading, while compression generate longitudinal cracks, and crack coalescence happens faster. The decrease in damping capacity in the first few cycles may be due to the stabilization of internal structure of the stone. Under cyclic compressive loading the friction between crack surfaces may account for the increase of damping capacity of the last cycles; this behavior doesn't occur in tension because of sudden failure of the specimen.

(Song et al. 2016) confirmed that stone failure and damage is controlled by localization of tensile strain. When cycling a specimen in compression at $F_{MAX} = 60\%$ of failure load and measuring the tensile strain fields (with a VIC), the region of strain concentration extends. This means that there is a permanent deformation and accumulation of damage in those points.

(Åkesson et al. 2004) performed uniaxial cyclic compression tests on drilled granite samples at frequency of 4Hz and $F_{MAX} = 60\%$ of the static test. The growth of cracks was analyzed qualitatively and quantitatively with fluorescent and polarized microscopy. The research proved that there is a fatigue effect leading to crack growth, due to the increase in volumetric strain of the specimens. The increase in radial strain suggests formation of cracks parallel to the loading direction, observation confirmed by the crack analysis. Compared to an unloaded sample, the fatigued one showed increase abundance of cracks parallel to the loading. These cracks are intragranular or transgranular, where the latter are due to propagation of existing grain boundary cracks. Gradient in mechanical strength and modulus of elasticity seem to be the cause for the nucleation of new cracks.

3.3 Glass fabric reinforced plastics

Textile reinforcement can be found employing weaving, knitting, stitching, and braiding technologies. Such technologies have been developed to improve the interlaminar strength, toughness and compressive strength of laminates. The behavior in compression is influenced by the properties of the fibers, of the matrix, and of the interface. Response of unidirectional or bidirectional laminates to out-of-plane loading is weak, as only the matrix contributes to the strength. Compressive strength of woven laminates, compared to non-woven, have 15% strength decrease as a result of the stress concentration points given by cross-overs (Yang et al. 2000).

(Caprino & Giorleo 1999) reported, in addition to the flexural fatigue resistance of glass fabric-reinforced epoxy resin (GFRP), its monotonic behavior in 4pt bending. GFRP had a linear elastic behavior up to 70% of its failure load, after which yielding occurs. Deviation from linearity occurred with kinks at the compression surface of the specimen, associated to buckling of the glass fibers in compression. Failure occurred for macroscopic buckling, and resin whitening was visible.

Also in fatigue, failure happens due to compression, but whitening emerged throughout the entire test and the the entire volume, with final rigidity at break 15% of the initial rigidity.

The endurance limit of GFRP in tension-tension fatigue, as tested by (Jeon et al. 2011), is 20% at stress ratio 0.1 (Figure 3.9 The S-N curves of woven fabric glass/epoxy laminate composites compared to Al 6005 in accordance with the maximum stress; R= 0.1 (from (Jeon et al. 2011)).). In tension-compression with stress ratio of -1, endurance limit of the tested laminate was found at 20% stress percentage in the warp direction, and 20% in the fill direction. Additional information on literature on fatigue of unidirectional composites was given in §2.2.

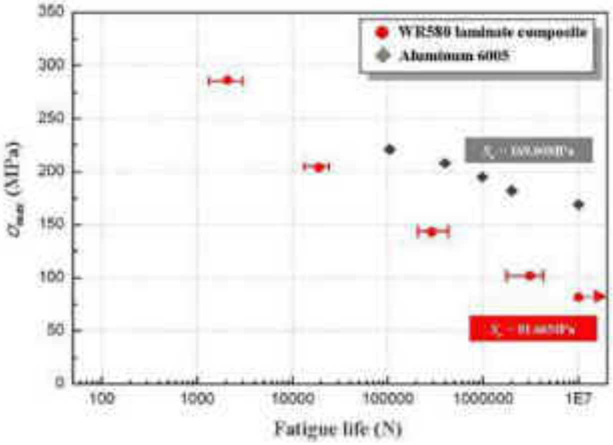

Figure 3.9 The S-N curves of woven fabric glass/epoxy laminate composites compared to Al 6005 in accordance with the maximum stress; R= 0.1 (from (Jeon et al. 2011)).

3.4 Sandwich composites

Generally constituted by a lightweight core and resistant faces, sandwich composites are widely used as load carrying materials. Here follows a summary of the failure modes in static and fatigue loading.

3.4.1 Static failure of sandwich composites

Reported failures for symmetric sandwich composites are due to: face/core yielding or fracture, core shear, buckling - face wrinkling, delamination, buckling – face dimpling (in honeycombs), and core indentation – core yield (Figure 3.10 left).

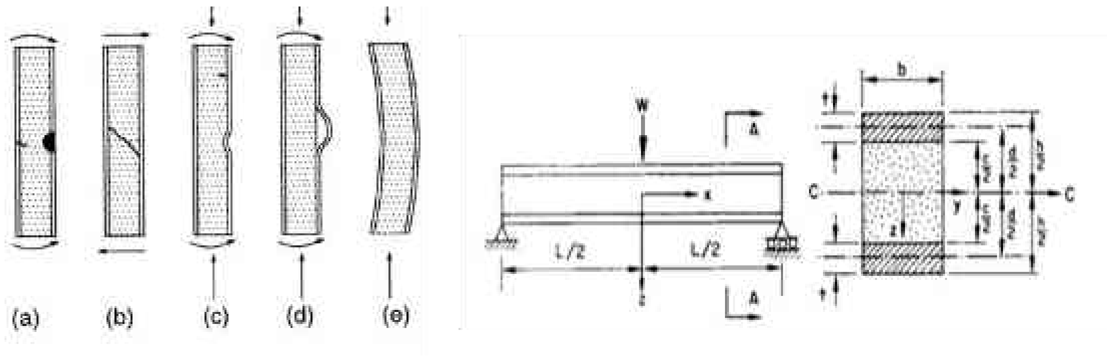

Figure 3.10 Left: sandwich failure modes, taken from (DNV 2003) a) face/core yielding, b) core shear, c) buckling – face wrinkling, d) delamination, e) general buckling. Right: Sandwich beam denominations.

It is possible, in the case of sandwich materials with thin faces, to use the ordinary theory of bending to predict the failure mode or design the composite against a particular failure. The theory assumes that cross-sections which are plane and perpendicular to the longitudinal axis of the unloaded beam remain so when bending takes place. Under a bending moment, M, the stress σ occurring in a section at distance z from the neutral line is given by:

$$\sigma = \frac{M \cdot z}{I} \tag{3.4}$$

In a sandwich beam (Figure 3.10 right), however, the flexural rigidity (*IE*) is the sum of the flexural rigidities of face and core, measured about the centroid:

$$D = E_f \frac{bt^3}{6} + E_f \frac{btd^2}{2} + E_c \frac{bc^3}{12} \tag{3.5}$$

To obtain the stress experienced at a certain depth *z*, the strain at that point has to be multiplied by the modulus of elasticity of the layer. The approximated normal and shear stress distribution in a section, along the z axis, is reported in Figure 3.11. Shear stress is normally neglected in the faces, since it is much lower than the normal stress acting there, therefore in the faces: $\sigma_1 = \sigma_f$, $\sigma_2 = 0$. Generally, but not always, the shear stresses in the core are large compared with the normal stresses; in this case the principal stresses in the core are equal to the shear stress ($\sigma_1 = \tau_c$, $\sigma_2 = -\tau_c$).

Figure 3.11 Linear stress distribution in sandwich beam under bending moment

For a sandwich beam in three-point bending, the predicted collapse loads based on the beam theory, and for the different collapse modes, are (Steeves & Fleck 2004):

Face yielding or microbuckling	$P = \frac{4\sigma_f btd}{L}$
Face wrinkling	$P = \frac{2bdt}{L}\sqrt[3]{E_f E_c G_c}$
Core shear failure	$P = 2\tau_c bd$
Indentation	$P = bt\left(\frac{\pi^2\sigma_c^2 E_f d}{3L}\right)^{1/3}$

Yielding in the face is initiated when the equivalent stress in the face at the extreme fiber equals the yield stress of the face material. Wrinkling occurs when the stress in the compressive face reaches the critical stress given. Similarly, core yields in shear when the maximum shear stress in the core reaches the shear strength of the foamed core material; in tension, when the maximum principal tensile stress in the core equals its yield strength, there is failure in core tension. By using the formulae reported, it is possible to construct failure maps which indicate, for a given geometry and material selection, the failure load and failure mode. Therefore, an appropriate selection of face-sheet thickness, core thickness and core density, makes it possible to design a sandwich with a desired type of failure (Zenkert & Burman 2011; Triantafillou & Gibson 1987). Maps for PVC core and laminated faces have been provided by (Steeves & Fleck 2004), while (Triantafillou & Gibson 1987) did them for alloy face sheets and polymeric foam cores.

Our specimen can fail for the same mechanisms mentioned above, but due to its complex geometry failure maps might be very different. With an optimized production process, a previous study showed that in 4-point bending under third point load the sandwich failed on the stone face (Gomes 2016). Delamination did not occur, proving a good adhesion quality of layers. Shear failure of the core arouse when high resin infiltration in the cork agglomerate was combined with high curing pressure (3 bar). This condition leads to embrittlement of the cork core and a permanent compressive deformation (due to the high curing pressure), that reduces the cork's maximum shear strength.

The distribution of stresses inside our specimen can help us understand where the higher normal and shear stresses are located; for this purpose, the theory of classical lamination is used in this analysis (see § 3.5).

3.4.2 Fatigue failure of sandwich composites

The work present in the literature is limited to symmetric sandwich composites; faces are commonly made of fiber-reinforced plastic or metal sheets, and cores are made of foams, honeycombs or other cellular materials.

Failure modes in fatigue are often similar to those observed in static and impact loading. Under cyclic loading, though, sandwich beams are particularly prone to core shear failure. (Sharma 2006) observed that this is because cyclic loading reduces the residual shear strength of the foam core. The principal modes of failure are three: face-sheet yield, core shear, and indentation; their occurrence depends on the thickness of the faces, and their strength.

(Burman & Zenkert 1997) pointed out in their test of foam core sandwich beams that heat was generated in the foam, which, due to its insulating properties, is not lead away. Localized heating happened just beneath the loading rigs and was transferred from the cylinder of the test machine to the specimen. At high loading ratios the thermal influence from the warm loading piston was the cause of failure under the supports. In fact, the fatigue lifetime at higher temperatures decreases and localized heating damages the specimen, invalidating the experiment. This result suggests that autogenous heating has to be considered in the future tests. They observed that the damage initiation phase consisted of the most part of the fatigue life, during which microscopic damage forms, and after which progression and failure follows due to coalescence of microcracks.

(Shafiq & Quispitupa 2006) tested sandwich beams made of carbon-epoxy faces and kraft-paper honeycomb-filled PU foam as core in flexural fatigue, classifying damage according to AE events. Core failure resulted to be the predominant damage mechanism of flexural fatigue followed by interfacial failure, whereas, fiber rupture triggered the onset of catastrophic failure. Core cracks appeared early in cyclic life, propagated parallel to the interface for a distance that varies with load applied, and changed opening mode to shear.

(Kanny & Mahfuz 2005) observed that only in the last stages of the cyclic test on S2 glass fiber–vinylester reinforced sandwich composites with PVC cores, would numerous cracks in the core under the loading point appear, that coalesce into a bigger crack which propagated in the compression side of the beam. After reaching a critical length, the crack kinked of 45° and propagated on the tension side. It is reported that the first stage of crack coalescence accounts for 80% of the fatigue life. The authors also investigated the effect of frequency and core density on the fatigue life; a frequency dependence occurs because of localized heating that makes the core more compliant. The results showed that the number of cycles to failure increased with frequency, but the time to failure showed the opposite trend. Such behavior was attributed to the external work not contributing to plastic deformations, but to increase the temperature of the core. Therefore, less strain energy was available for the damage process. The crack propagation depends on the frequency, only when this causes a temperature increase; in this case, since the core is more compliant, it delays the crack propagation

(Shenoi et al. 1995) reported fatigue failures either for core shear cracks or for face tension, when testing beams with different foam density and reticulation. As foam density increases, failure occurs for face tension. Predictions of failure mode can be made from static tests only if the failure loads are not too close.

The overall feeling of the scientific authors read is that the fatigue process and damage accumulation mechanism is still not well understood, despite fatigue studies on sandwich materials have been carried out since the 80s.

3.5 Calculation of stresses

In this section, two methods are presented through which it has been attempted to determine the stress distribution of the composite: the classical lamination theory and the classical beam theory.

Materials properties

Cork and stone are assumed to be isotropic. Therefore, their properties are fully defined with two independent constants: Young's modulus (E) and Poisson's ratio (ν).

The glass fabric reinforced plastic (GFRP) layer is transversely isotropic, where the 1-2 plane is the plane of isotropy. Therefore, the 1 and 2 subscripts on the stiffnesses are interchangeable. The stress-strain relations have five independent constants: E_1, E_3, ν_{12}, ν_{13}, G_{23}. In the present flexural tests, the principal directions coincide with the engineering directions (x y z), thus they will also be used interchangeably.

The elastic moduli of fibers and resin were found from the data-sheets of the supplier; the proprietary quantity of resin is expressed as weight ratio, therefore it was converted as volumetric ratio, then the elastic modulus of the resin-fabric layer has been obtained with the rule of mixtures. From the volumetric density of the glass fabric and its areal weight, the fabric thickness was estimated to be 0.23 mm. Exact measurement of the thickness of this layer is difficult, and it was decided to use the value of 0.5 mm as thickness.

The thickness of white limestone is always lower than 5 mm, namely approximately 3.6 mm. Its compressive modulus is not usually listed in the technical sheet, as it is of difficult evaluation and great variability as a consequence of the heterogeneous stone texture. A value of 35 GPa has been obtained in an experimental classwork within a geology course in Mining Engineering, and it was considered suitable. Literature reports value of Young's modulus from 20 to 70 GPa for limestone. Its tensile modulus is approximately 10% of the compressive modulus.

Tensile modulus of cork's agglomerate is so small compared to the other layer's, that it can be neglected.

The values used for the analysis are listed in Table 3.3.

Table 3.3 Thickness, Young's modulus, Poisson's ratio, and bulk modulus of the materials, as used in the stress analysis

Material	*Thickness (mm)*	*E (GPa)*	*v*	*G (GPa)*
Stone	3.6	35	0.25	14
GFRP (top & bottom)	0.5	36.5	0.1	10
Cork	15	-	0.1	-

3.5.1 Classical lamination theory (CLT)

The CLT makes the following assumptions:

- The laminate is *sufficiently* thin. This means that a line originally straight and normal to the middle surface of the laminate is assumed to remain straight and normal to the middle surface when the laminate is deformed. Thus $\gamma_{xz} = \gamma_{yz} = 0$ and $\varepsilon_z = 0$.
- The bonds are presumed to be infinitesimally thin as well as non-shear-deformable. This results in continuous displacements across lamina boundaries so that no lamina can slip relative to another.
- Small and equal deformations within the elastic stress range for all components.

The steps to evaluate the stress distribution can be found in (Jones 1998), and involve the calculation of a stiffness matrix ($[Q]$) for each layer (Eq. 4.1), the assembly of the matrixes in the so-called $[ABD]$ matrix (Eq. 4.2, 4.3), the calculation of the strains and curvatures at each ply interface, and finally the calculation of normal and shear stresses.

$$\begin{bmatrix} \sigma_1 \\ \sigma_2 \\ \tau_{12} \end{bmatrix} = \begin{bmatrix} Q_{11} & Q_{12} & 0 \\ Q_{12} & Q_{22} & 0 \\ 0 & 0 & Q_{66} \end{bmatrix} \begin{bmatrix} \varepsilon_1 \\ \varepsilon_2 \\ \gamma_{12} \end{bmatrix} \quad (4.1)$$

$$A_{ij} = \sum_{k=1}^{N} \left(Q_{ij}\right)_k (z_k - z_{k-1}) \quad (4.2)$$

$$B_{ij} = \frac{1}{2}\sum_{k=1}^{N}(Q_{ij})_k(z_k^2 - z_{k-1}^2)$$

$$D_{ij} = \frac{1}{3}\sum_{k=1}^{N}(Q_{ij})_k(z_k^3 - z_{k-1}^3)$$

$$\begin{bmatrix}[N]\\ [M]\end{bmatrix} = \begin{bmatrix}[A] & [B]\\ [B] & [D]\end{bmatrix}\begin{bmatrix}[\varepsilon]\\ [k]\end{bmatrix} \tag{4.3}$$

The resulting [*ABD*] matrix is:

$$\begin{bmatrix} 189 & 54.2 & 0 & -1142 & -396 & 0 \\ 54.2 & 189 & 0 & -396 & -1142 & 0 \\ 0 & 0 & 67.2 & 0 & 0 & -373 \\ -1142 & -396 & 0 & 12188 & 3516 & 0 \\ -396 & -1142 & 0 & 3516 & 12188 & 0 \\ 0 & 0 & -373 & 0 & 0 & 4336 \end{bmatrix}$$

The application of a force of 1 kN on the testing machine produces the stress distribution of Table 3.4, represented in Figure 3.12. The neutral line is located 3.91 mm below the stone layer, therefore on the interface between the cork and the glass fiber.

Table 3.4 Normal stresses distribution in L1C1 according to the CLT.

	Normal stresses (MPa)			
	Stone	*GFRP*	*Cork*	*GFRP*
Top	-24.5	-1.6	0.0013	89.7
Bottom	-1.14	1.34	0.087	92.6

3.5.2 Classic beam theory

The calculation of stresses in each layer has been done according to (Allen 1969), and comprises of two steps:

1) Evaluation of the strain of each layer, according to

$$\varepsilon = \frac{Mz}{D}, \tag{4.4}$$

where *D* is called flexural rigidity, and for a sandwich beam it is the sum of the flexural rigidities (I*E) of its components.

2) Evaluation of the stress, as $\sigma = E\varepsilon$.

The flexural rigidity of this beam was found to be: 249468 GPa mm^4. The application of a force of 1 kN on the testing machine produces the stress distribution of Table 3.5 and Figure 3.12. The neutral line is located 3.98 mm below the stone layer, therefore on the interface between the cork and the glass fiber.

Table 3.5 Normal stresses distribution in L1C1 according to the classical beam theory.

	Normal stresses (MPa)			
	Stone	*GFRP*	*Cork*	*GFRP*
Top	-19.8	-5.35	0	116
Bottom	-5.13	-3.23	0.00165	119

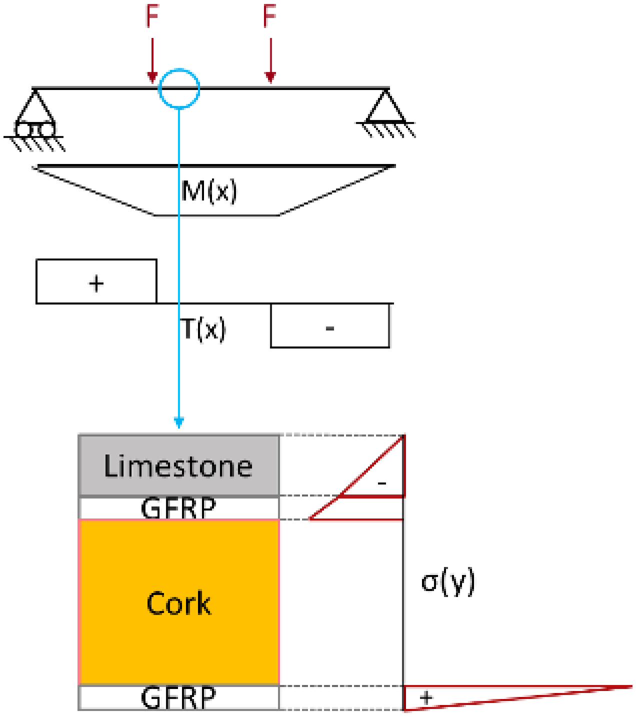

Figure 3.12 Graphical representation of the normal stress distribution according to the CLT and classic beam theory.

Chapter 4.

Materials and methods

4.1 Materials

The studied composite material is made by a limestone backed by a glass-fabric reinforced cork sandwich. By varying the type of limestone only, two configurations were obtained, and named L1C1 and L2C1. The mechanical characteristics of the various layer will be hereafter presented, as given by the materials producers.

4.1.1 Limestones

Figure 4.1 Geological map of Portugal with indication of the quarry location of the limestones Vidraço Azul (Alcobaça) and Branco do Mar (Porto de Mós).

In this thesis, two different Portuguese limestones were selected to form the stone layer of the composite material: *Branco do mar* (L1, white limestone) and *Vidraço de Ataíja azul* (L2, blue/grey limestone). The stones, which were quarried in Pordo de Mós and Alcobaça (Figure 5.1), have similar mineral compositions, but different physical and mechanical properties, particularly due to the difference in porosity value.

According to the Portuguese stone catalogue (www.lneg.pt), *Branco do Mar* is a fine grained whitish limestone, with calciclastic to oolitic macroscopic features, abundantly bioclastic. Their geological age is the Callovian, the last age of the middle Jurassic (166.1 ± 4.0 to 163.5 ± 4.0 million years ago). *Vidraço Azul* is described as grey and bluish-grey limestone, finely calciclastc and occasionally with some stylolites. The beds also formed in the Callovian age.

The mechanical and chemical properties of the limestones are described in Table 4.1.

Table 4.1 Mechanical and chemical properties of the used limestones (http://rop.lneg.pt/rop/FormTipo.php).

	Branco do Mar (L1)		Vidraço Azul (L2)	
Mechanical properties				
Compression strength	52	MPa	162	MPa
Flexural strength	7.5	MPa	10.3	MPa
Apparent density	2280	Kg/m3	2680	Kg/m3
Water absorption	6.2	%	0.4	%
Open porosity	13.3	%	0.9	%
Wear resistance	6.6	mm	2.6	mm
Impact resistance	30	cm of free fall	35	cm of free fall
Chemical analysis				
CaO	55.91	%	54.31	%
Al_2O_3	0.10	%	0.88	%
MgO	0.10	%	0.26	%
SiO_2	0.22	%	1.05	%
Fe_2O_3	0.05	%	0.15	%
P.R. (LOI)	43.82	%	42.95	%

Macroscopic analysis was performed as a general characterization of the stone structure; examinations at low magnifications (Figure 4.2 left) were made with a common camera. Specimens examination at higher magnification (Figure 4.2 right) were performed with the digital microscope Dino-Lite AM7515MZT.

It can be seen with naked eye that L1 has a granular structure with high porosity between the grains, which are held together by a matrix. The grains are whitish, round, and approximately all the same size (diameter of 0.1 to 0.4 mm). The structure is isotropic and homogeneous.

Later characterization with X-ray CT confirmed the observations, but also showed zones of higher density inside the stone, which couldn't be observed with optical microscope. Such zones are a natural feature of stones.

Due to the porous structure of L1, there is a visible boundary between the zone where resin was absorbed and where there is no resin; in this thin layer, all pores are filled with the resin, and the grains become indistinguishable. L2 has a compact structure, with no visible pores nor layer of resin absorption.

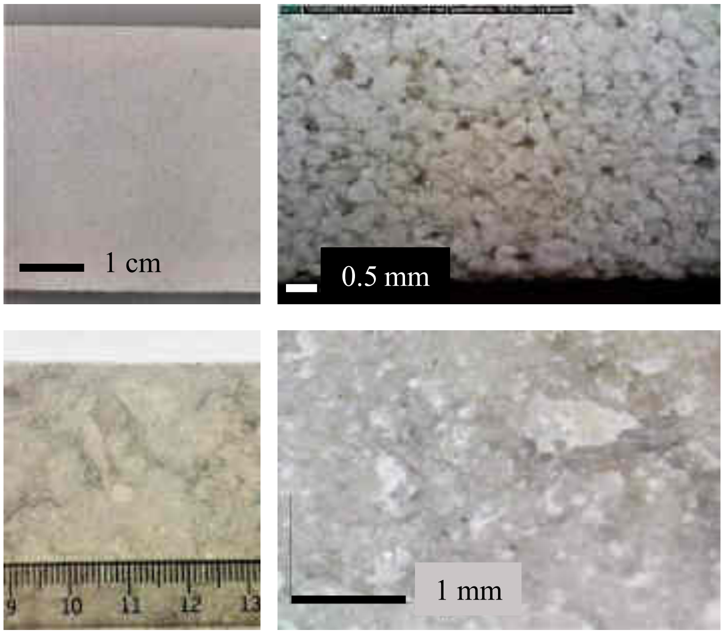

Figure 4.2 Macroscopic (left) and microscopic (right) examination of the limestones L1 (top) and L2 (bottom).

4.1.2 Cork agglomerate

The cork agglomerate was provided by Amorim Cork Composites. Its mechanical and physical properties are shown in Table 4.2. As already mentioned, it is made of the agglomeration of small cork particles, whose binder is polyurethane.

Table 4.2 Cork mechanical properties as provided by the manufacturers

	Cork	
Density	200	kg/m^3
Compressive Strength	0.5	MPa
Compressive Modulus	6	MPa
Tensile Strenght	0.7	MPa
Shear Strength	0.9	MPa
Shear Modulus	5.9	MPa

Cork agglomerate has uniform macroscopic appearance. Again, pictures were taken at low magnification with a common camera, high magnification using Dino-Lite AM7515MZT, and even higher using a SEM (Figure 4.3). Under high magnifications cork's appearance is highly heterogeneous. Cork's cells have different orientations among grains and, due to the stresses induced during compaction, cells' orientation inside the same grain also varies. Grains are coated with a polymer to provide adhesion; the coating is highly uniform, located only in the exterior of grains, without areas of high polymer concentration.

The area of the granules was measured from Figure 4.3 top-right using ImageJ software; a circular sample was chosen, inside which the perimeter of all granules is manually marked, and the granule area and shape automatically calculated; area and shape influence the compaction of granules. Circularity is calculated as

$$Circularity = 4\pi \cdot Area/Perimeter^2 \,.$$

A value of circularity of 1 indicates a perfect circle, towards 0.0 it signifies an increasingly elongated shape. Area and shape Pareto diagrams were generated, and shown in Figure 4.4.

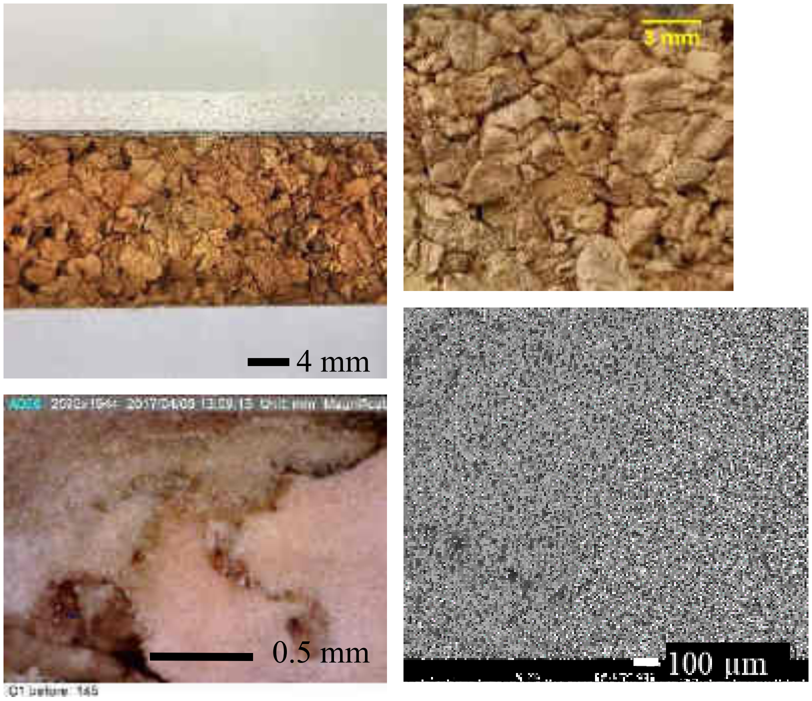

Figure 4.3 Top left: macroscopic image of the cork in the composite; top right: closer view of cork agglomerate; bottom left: detail of the binder between agglomerates; bottom right: SEM image of the cork cells.

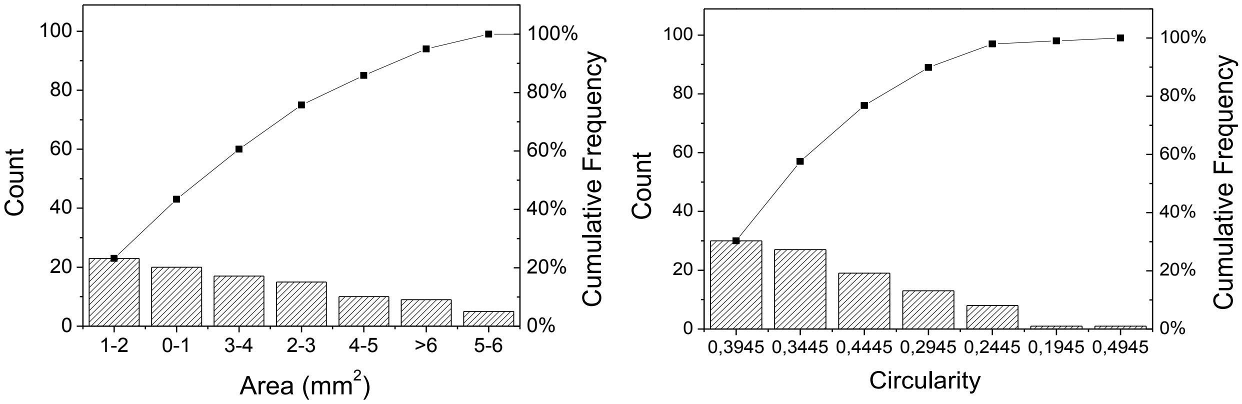

Figure 4.4 Pareto diagrams of the area (a) and of the circularity (b) of the cork agglomerate

4.1.3 Biaxial glass fabrics

Resin impregnated biaxial woven fabrics stiffen the cork layer (above and below it). The fabrics in the two layers have different grammage, being the one in contact with the stone of higher grammage in order to permit a smoother Young's modulus gradient. Their mechanical properties are given in Table 4.3.

Table 4.3 Mechanical properties of the glass fabrics

	Biaxial fabric E glass 1		*Biaxial fabric E glass 2*	
Weave	Plain		Plain	
Areal density	612	g/m^2	290	g/m^2
Volumetric density	2.6	g/cm^3		
Filament diameter	12 to 15	µm	8.9 to 10.2	µm
Tensile strength	1900 to 2400	MPa	1900 to 2400	MPa
Tensile Modulus	69 to 76	GPa	69 to 76	GPa
Elongation at break	3.5 to 4	%	3.5 to 4	%
Thickness	0.23077	mm	0.29	mm

4.1.4 Manufacture of the composite

The first step to manufacturing stone composite panels is to quarry the natural stone. Blocks of stone of size about 1,5 m wide x 3 m long x 1,5 m high are extracted from the quarry with cutting techniques developed to maintain the block as free of defects as possible; the most employed tool is the diamond wire saw, invented by Luigi Madrigali.

Blocks are then transported to the stone factory, where they are cut into slabs with minimum thickness of 10 mm (Figure 4.5 right) and afterwards polished on one side. The slabs are trimmed to the desired nominal size, milled flat, washed and dried. Once the stone has the needed length and width, the production of the stone-cork composite can take place: stones are dried prior to the placement of a layer of resin-impregnated glass cloth, unless the stone is too big to fit in the drying oven.

Figure 4.5 Left: Stone quarry in Estremoz, Portugal. Right: cutting stone into slabs.

The glass fabric is impregnated of resin with the aid of spatulas, in order to have homogeneous coverage and eliminate most of the bubbles. The cork layer and the last layer of resin-impregnated cloth follow in order, and at last a polyethylene sheet prevents adherence of the resin with the plate of the hot press. In an optimized production process, this layering of resin-impregnated glass cloth, cork and other glass fabric is repeated on the other side of the stone, obtaining at the end a stone slab sandwiched between two reinforcing layers. Nevertheless, in the present case, only one-sided composites were produced. The composite is then placed in a hot press where curing of the resin occurs, and later post-cured, as prescribed by the resin manufacturers. Post-cure allows for alleviation of thermal stresses, due to mass diffusion and reduction of free volume around the polymeric chains, which results is higher transition temperature, flexural resistance and higher displacement at break.

The cork-stone-cork undergoes a cutting process at the middle of the stone thickness, to yield two panels of the same dimensions using diamond studded wire saws. In the present case of cork-stone only, this step was not done. At the end, stone is set to the desired height, stone surface is finished according to the customer's choice, and the composite is cut to the final dimensions.

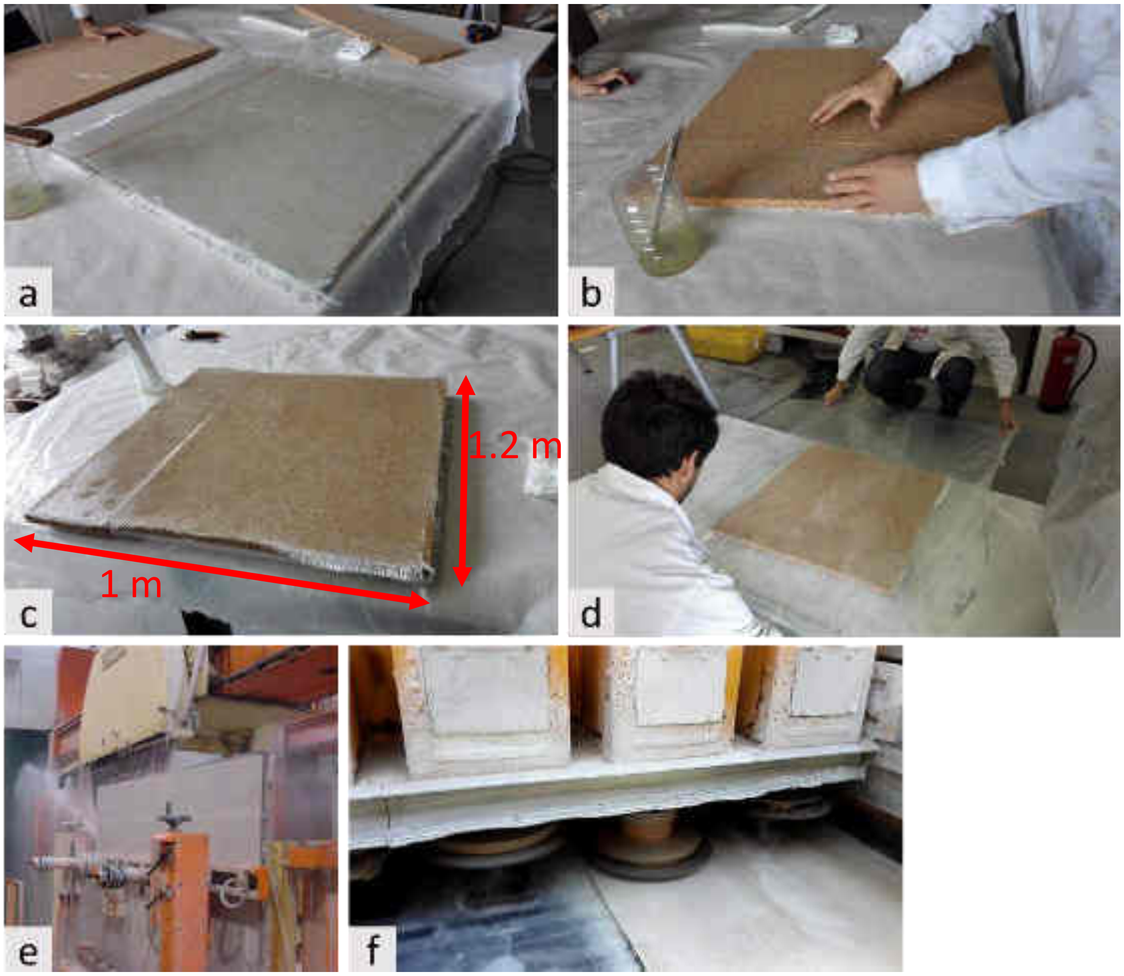

Figure 4.6 a) First glass fabric reinforced plastic layer; b) Deposition of cork agglomerate layer; c) Second glass fabric reinforced plastic layer; d) Application of LDPE sheet before curing process in the hot press; e) Cutting of the "double-sandwich" in two panels; f) grinding of the stone layer until the desired thickness.

4.2 Methods

The static and fatigue testing was performed using the same geometry (Figure 4.7, Table 4.4), with the stone layer on the compressive side. The testing machine for both tests is the servo-hydraulic Instron 8800, with load cell of 100 kN. The cylindrical rollers have a radius of 20 mm.

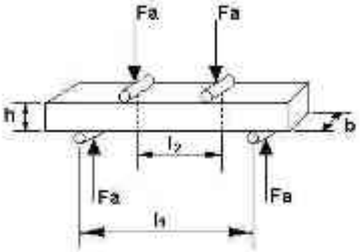

Figure 4.7 Static and fatigue test geometry

Table 4.4 Geometric dimensions of the specimens

b	l_1	l_2
50 mm	250 mm	83.3 mm

The manufacturing was done in two steps: initially, the stone plates of dimensions 300 mm x 600 mm and 8-10 mm of thickness were laminated; then, to obtain specimens of the desired dimensions, the plates were processed by the company "Joaquim Duarte Urmal & Filhos, Lda". The final process comprehends the lowering of the stone layer to a thickness of about 5 mm, and the cutting of the plate in specimens of the final dimensions (300 mm x 50 mm). The composites with the two limestones were worked in the same moment, with the saw blade set at the same height. Due to the lower mechanical resistance and higher brittleness of L1, the process resulted, for the material L1C1, in a) an uneven distribution of the thickness along the specimen's length, and b) a final thickness of the stone always less than 5 mm. As it will be mentioned, that thickness will influence the failure load of the composites.

4.2.1 Static tests

The tests were carried out to determine the failure load (F_{UF}) of the materials, which will then be used to define minimum and maximum force (F_{MIN}, F_{MAX}) of the fatigue cycles. The tests are conducted at constant velocity of 5 mm/min.

4.2.2 Continuous fatigue tests

The flexural fatigues tests were performed in load control, at a frequency of 2.7 Hz for L1C1 and of 4 Hz for L2C1, sinusoidal waveform, load ratio R = 0.1, and maximum load chosen as a percentage of the static failure load. Due to time limits, all the tests were stopped at 500'000 cycles, or when catastrophic failure occurred. The fatigue test variables (R, F_{MIN}, F_{MAX}, F_A) are dependent by the relations $R = F_{MIN}/F_{MAX}$ and $F_A = (F_{MAX} - F_{MIN})/2$. Therefore, only two variables need to be arbitrarily chosen.

Due to the viscoelastic nature of the material, and to the different response of the limestones, it has been necessary to set the PID of the testing machine. The values of PID that guarantee that the output waveform approaches as much as possible the waveform requested by the user are given in Table 4.5.

Table 4.5 PID values for the fatigue tests

	L1C1	L2C1
P	12.60	23.75
I	2.5	0.222
D	0	0
Lag	12.30	3.00

The testing machine records the value of force, position, and time for every cycle, as defined in the test method. Besides these values, to compare the test results at different maximum force, further parameters have been calculated by using a MATLAB function written by the author. Those parameters have been called: relative stiffness (D_{rel}), absolute stiffness (D_{abs}), accumulated deformation, dissipated energy per cycle, and cumulative dissipated energy. They will be hereafter presented in detail.

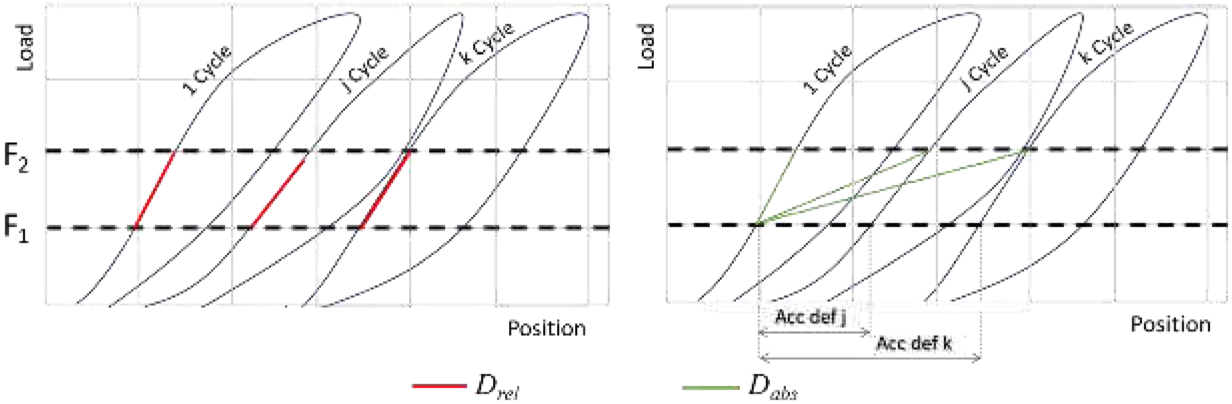

Figure 4.8 Graphical representation of the hysteresis cycles and of the calculated parameters

Stiffness is defined as the ratio between the applied force and the displacement of the piston. If the piston does not penetrate on the material, that displacement also reflects the displacement experienced by the specimen.

- **Relative stiffness**. Since the load-displacement curve is not linear, it is necessary to define two force values (F_1 and F_2 in Figure 4.8) between which to calculate the slope, which is equivalent to the tangent stiffness of the two points. The extremes were decided, for the two materials, according to where the linear part of the curve is located, and approximately between 0.3 - 0.5 F_{UF}. In L1C1 it is calculated between 300 - 600 N, in L2C1 between 600 - 900 N. The linear approximation of the curve is considered correct (R^2=0.99).
- **Absolute stiffness**. The need to calculate this parameter can be appreciated observing Figure 4.8, which is a model of the hysteresis curves; when the number of cycles increases, the material accommodates a deformation which is not instantaneously recovered, and which is not taken into account in the calculation of D_{rel}. Therefore, D_{abs} has

been introduced to have a unique parameter where both the slope of the curve and the accumulated deformation are included.

- **Accumulated deformation**. It is the deformation not recovered at force F_1, and equal to the difference between the position of the n*th* cycle and of the first cycle at F_1: $d_{acc}^{n} = d_n(F_1) - d_1(F_1)$.
- **Dissipated energy**. It is quantified by the area inside the hysteresis loop. In this case, the integration has been done using the trapezoidal approximation:

$$A_j = \sum_{i=1}^{n-1} (F_i + F_{i+1}) \cdot (d_{i+1} - d_i) \cdot \frac{1}{2},$$

  where A_j is the area of the j*th* cycle, and *n* the number of data per cycle.
- **Cumulative dissipated energy**. It is the cumulative sum of the energy dissipated in every cycle. Since the testing machine only saves data of a limited number of cycles (e.g. 100, 101, 200, 201, … , 1000, 1001, 2000, 2001, …, 10000, 10001 etc), it is assumed that the energy absorbed in the cycles where no data are available is the average between the energy of the previous and next known cycles.

4.2.3 Fatigue tests with resting time

Fatigue tests with 24 hours resting time between blocks were conducted for L2C1 at load percentages of 45, 50, 55, 60%. The number of cycles in a block is equal to 70% of the failure cycles (N_f) in the continuous tests. The test design is summarized in Table 4.6. The parameters calculated were the same as those of the continuous tests.

Table 4.6 Test design parameters for the fatigue test with stops

Load percentage	N_f	Cycles per block
45	Inf	500’000
55	130’000	90’000
60	38’000	26’000
65	3600	2500

4.3 X-ray Computed Tomography

4.3.1 Functioning principles

X-ray CT is a non-destructive technique able to image the internal structure and composition of stones before and after stress is applied. A specimen of appropriate size is placed in the trajectory of an X-ray beam; a scintillator converts the transmitted X-rays into visible light, and a camera records this light. After the picture is taken, the sample rotates of a fraction of a degree, and the process is repeated until the sample has completed 180° or 360°. At the end of a measurement, the pictures taken, which represent the full scan, are elaborated by a computer program and as an output we have a 3D image (Figure 4.9). CT is based on the fundamental principle that the attenuation coefficient depends on the density of the object passed by the X-rays, the atomic number and the power of the rays.

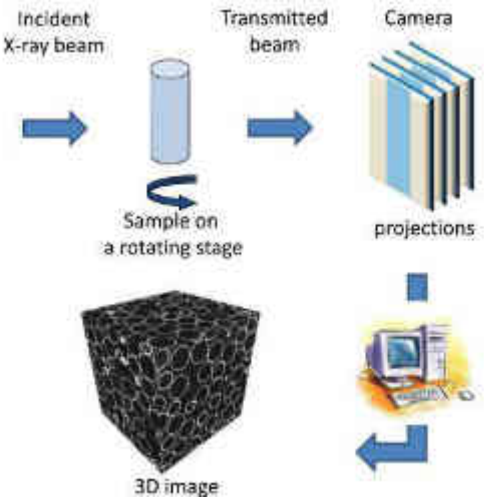

Figure 4.9 Functioning scheme of a X-ray CT from (Salvo et al. 2010)

If the X-ray at the exit of the tube is made monochromatic or quasi-monochromatic with the proper filter, one can calculate the attenuation coefficient corresponding to the volume of irradiated material by the application of the general formula of absorption of the X-rays in the field: $I = I_0 e^{-\mu x}$. The image by the CT scanner is a digital image and consists of a square matrix of elements (pixel), each of which represents a voxel (volume element) of the tissue of the patient. The image is reconstructed from many measurements of attenuation coefficient.

The spatial resolution depends on the spot size of the X-ray source, on the pixel size and scattering of the detector, on the scintillator, on the measurements and algorithm used for reconstruction among others. Typically, spatial resolution in laboratory tomographs varies from millimeters to one micron. The popularity of X-ray CT in material science has risen in the last 10 years or so, as reflected by the increasing number of papers published employing the technique. The reasons are obvious: it allows to follow the microstructural evolution of microstructure during heat treatment and mechanical testing (either at room or high temperature) non-destructively and at scale sizes down to one micron; post-mortem, as well as ex situ, and continuous in situ analysis are possible; moreover, this technique overcomes the limitation of optical and transmission microscopes, which is the possibility to make only “2D scans”. (Salvo et al. 2010) followed the solidification of an aluminum alloy in real time using a specific furnace mounted on a synchrotron X-ray CT, which allows for very fast scans. (Zabler et al. 2008) studied cracks formation in limestone under unconstrained compression.

4.3.2 Experiments

The X-ray CT has been conducted at IST, on a Bruker Skyscan 1172 apparatus. Two samples have been drilled from each post-fatigue tested specimen, at different positions along the specimen (Figure 4.10) from specimens with limestones L_1 and L_2. Comparison with samples on sound specimens is made. Although stones are highly heterogeneous due to their nature, it is believed that two samples per composite are representative of the microstructure.

When performing a tomography on this composite material, the stone and cork layers have a very different X-ray absorption: cork is does not absorb X-rays at the power values in which stone is opaque, and vice versa. Following data acquisition, 3D images were reconstructed using the software CTvox 3.3.0.

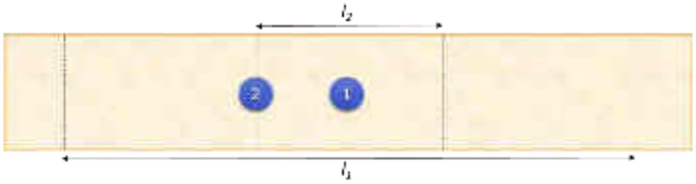

Figure 4.10 Position of X-ray CT drilled samples in the fatigued specimen

.

Chapter 5.
Results of static and fatigue tests

This chapter illustrates the results of the static and fatigue tests, as well as the images gathered through X-Ray CT inspection.

5.1 Static tests

The results of the static tests are represented in Figure 5.1 and summarized in Table 5.1 and Table 5.2, together with the specimens' thickness. The red lines indicate the inferior and superior load limit between which the stiffness is calculated, in the cyclic tests.

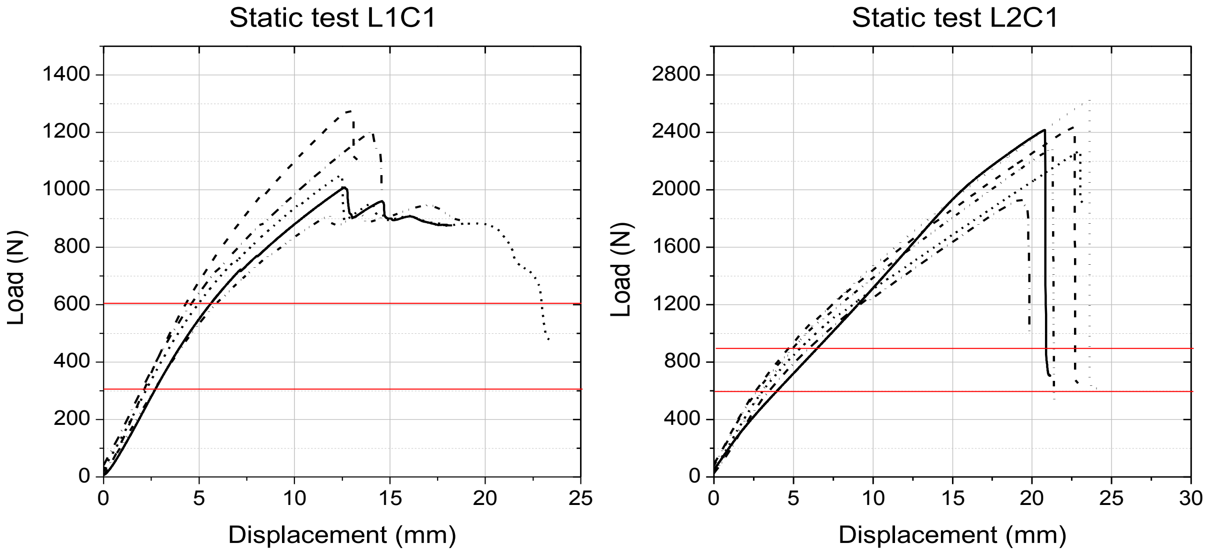

Figure 5.1 Load-displacement curves for the static tests L1C1 and L2C1

Table 5.1 Results of the static test L1C1

Name	*Average thickness (mm)*	*Failure load F_{UF} (N)*	*Deformation at break (mm)*	*Relative stiffness (N/mm)*
S1	20.21	1008	13.11	103
S2	21.01	1277	12.87	138
S3	20.60	1051	12.44	110
S4	20.90	1205	14.08	115
S5	20.05	903	11.80	93

Table 5.2 Results of the static test L2C1

Name	*Average thickness (mm)*	*Failure load F_{UF} (N)*	*Deformation at break (mm)*	*Relative stiffness (N/mm)*
S10	21.19	2289	21.23	117
S07	21.28	2439	22.68	143
S06	21.36	2418	22.88	149
S08	21.55	2626	23.57	118
S09	21.61	1932	19.40	134
S11	21.65	2271	23.02	125

5.1.1 Observation of failure

a. L1C1

Along the monotonic test, there is occurrence of audible fracturing of the stone above the outer rollers, which corresponds to the kinks in the load-displacement curves. The fracturing events are as follows (with reference to Figure 5.2):

1) Near the maximum load, the contact between the cylindrical roller and the stone generates an area of intensification of stresses, which eventually reach the compressive strength of stone. One crack nucleates, not at the point of contact but at a certain thickness below the roller; this cracks propagates parallelly to the interface (phase I).
2) After propagation, the crack kinks upwards and a layer of material is pushed away (phase II). Since the grain cohesion is not strong, the fracture surface is not planar but it is curved.
3) One or more cracks kink downwards (phase III).
4) The second group of cracks propagate in a direction parallel to the interface, and more precisely along the boundary of the resin-rich stone region (phase IV). Eventually a crack kinks of an angle less than 90° either towards the top or the bottom, in the latter case causing delamination (phase V) (Figure 5.3, Figure 5.2 b, c).

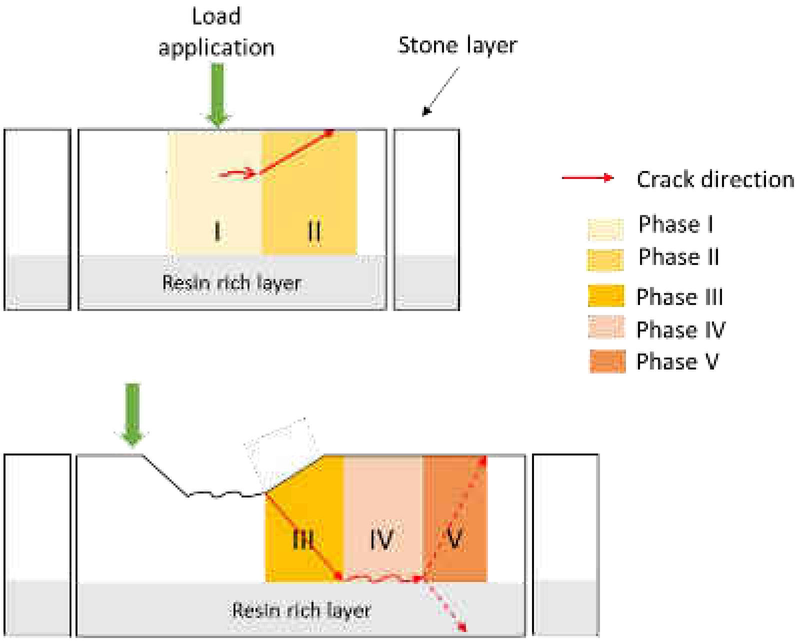

Figure 5.2 Scheme of crack propagation in white limestone (L1C1)

Figure 5.3 Macrocrack propagating below roller contact parallelly to the resin-rich layer; b) Crack kinking upwards in phase V; c) Crack kinking downwards in phase V and causing delamination; d) Evidence of intergranular fracture propagation

The propagation always occurs along grain borders, where there is the cementing matrix (Figure 5.3d). In this type of limestone, the shear stress resistance between grains is lower than that inside grains; fracture proceeds in an intergranular path.

b. L2C1

The fracturing events are as follows (with reference to Figure 5.4 right). Fracture always initiates below one of the rollers, and propagates parallelly to the load application, until it reaches the glass fiber layer. Propagation direction varies: during a first phase, propagation follows a plane inclined with respect to the load application direction for a thickness of about 1 mm (phase I in Figure 5.4). The inclination seems to be the same as that left by the stone cutting process (about 60°). Propagation proceeds almost perpendicularly to the load application direction for a length of the order of tenths of mm, for all the specimens (phase II). After phase II is completed, one crack propagates to the surface, detaching a chip of material (Figure 5.4 top-left). The initial crack then propagates down to the glass fabric layer (phase III); just above the glass reinforced resin layer, delamination occurs for a variable length (phase IV). For further deformations, one or more cracks propagate starting from the glass fibers up to the stone layer, until other stone pieces detach. The crack in phase V usually changes direction: where initially it is vertical, then it kinks.

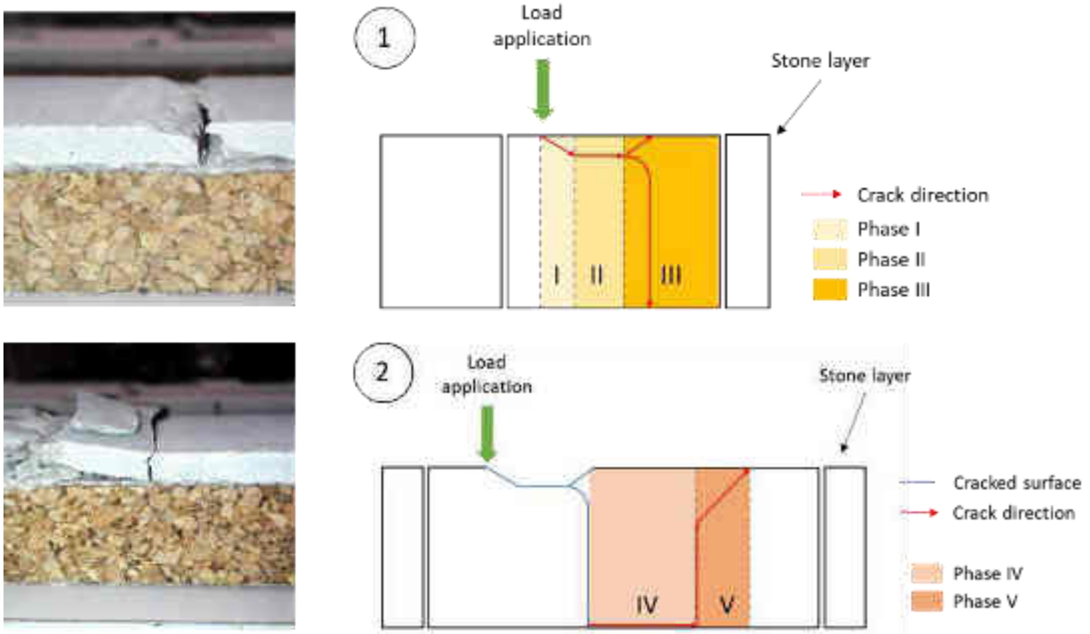

Figure 5.4 Images(on the left) and schematic representation (on the right) of crack propagation in L2

In this kind of limestone, the resin impregnation is not visible at naked eye, therefore it can't be said whether crack propagation follows the boundary between resin-rich stone or not. Nevertheless, the delamination surface has stone residues; we can thus infer that the resin-stone bonding is well done. Special attention should be put to the first stone chip that detaches: in all tests, the fracture surface is not planar, but presents some waviness (Figure 5.5). Each of the "wave peaks" represent a change in direction of the crack. This kind of behavior might be associated with the internal structure of the stone, which has stratifications.

Figure 5.5 Example of stone chip detached (phase III)

5.1.2 Influence of the thickness on the failure load

The thickness reported is the arithmetic average of three/four thickness measures, taken along l_2 (complete tables of the measurements in Appendix A). As previously mentioned, the unevenness of the thickness influences the failure load of L1C1. Figure 5.6 shows the failure load versus the average thickness (t); since there is an obvious dependence of the two parameters, it has been chosen to describe this dependence by a linear interpolation curve. The slope and intercept values obtained from OriginPro 8.5 built-in function are:

$$F_{UF} = 359{,}2\,t - 6283\,. \qquad (6.1)$$

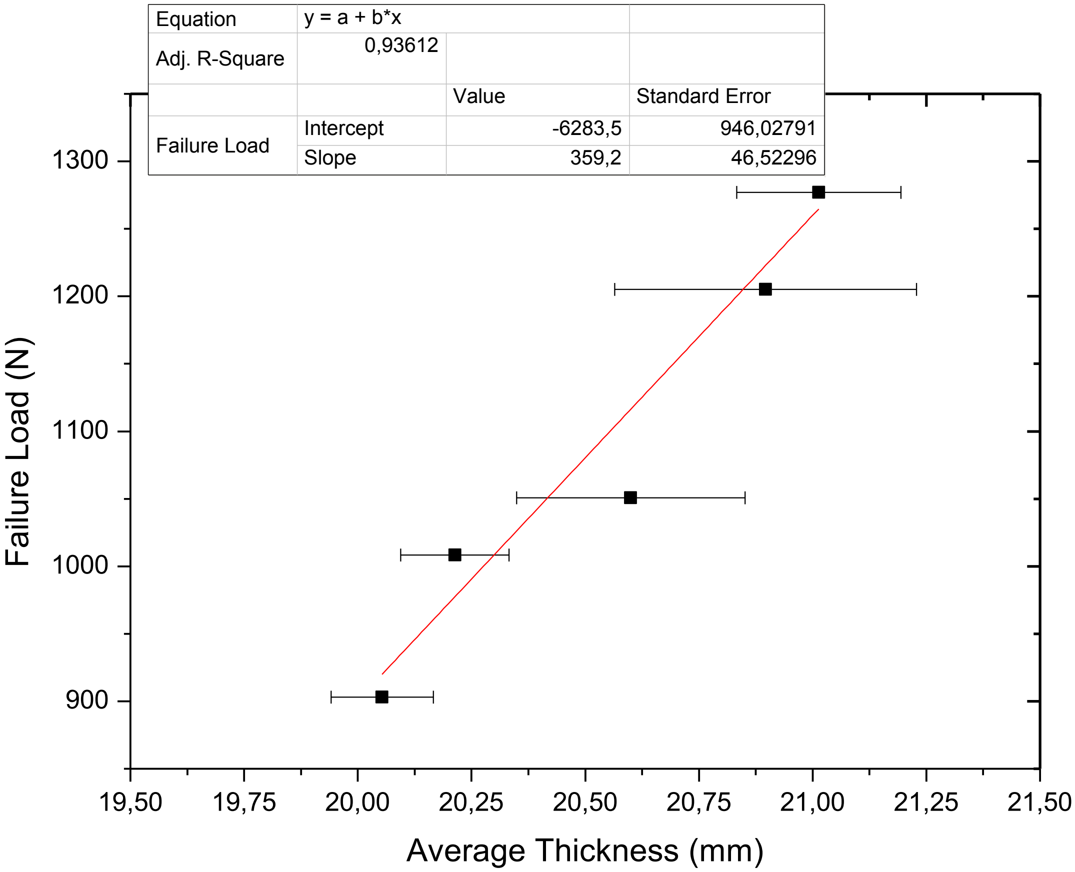

Equation	y = a + b*x		
Adj. R-Square	0,93612		
		Value	Standard Error
Failure Load	Intercept	-6283,5	946,02791
	Slope	359,2	46,52296

Figure 5.6 Failure load versus thickness for L1C1. The error bars refer to the standard deviation of the measures

As for L2C1, there has been no identified dependence $F_{UF}(t)$ both because a) the standard deviations of the thickness measurements on the same specimen are lower than in L1C1, and b) the variability of the average of the thicknesses is low (see Figure 5.7). It has been therefore concluded that F_{UF} of L2C1 can be taken as the average of the failure loads: 2409 N.

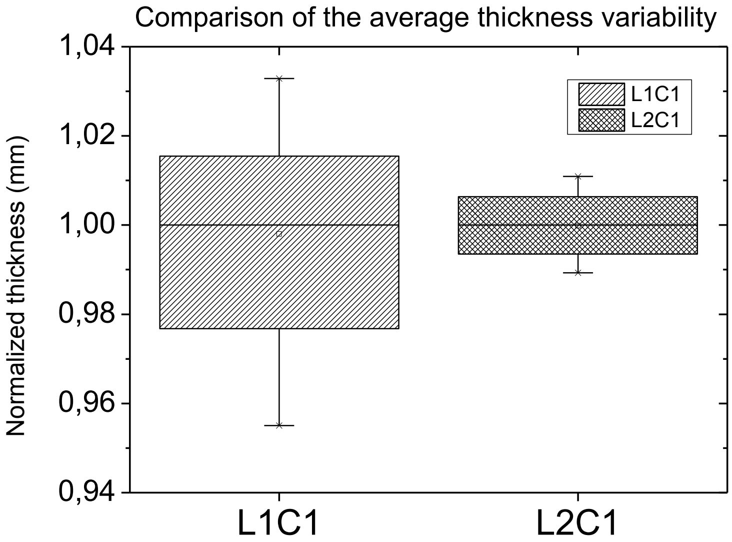

Figure 5.7 Comparison of the normalized average thickness variability of L1C1 and L2C1, where thickness is normalized with respect to the median of the data series.

5.1.3 Statistical considerations

a. Fitting with weighted least squares

When fitting the average thickness with an ordinary least square regression curve, we are assuming homoscedasticity, which means constant variance for each specimen. A way to take into account the difference in variance, giving more importance to data which have a lower dispersion, is to use a weighted least squares linear fit.

Entering the y_i coordinate as the one with the most error (hence the thickness in this case), the best fit values of the slope and intercept are given by:

$$b = slope = \frac{1}{\Delta}\left(\sum \frac{1}{\sigma_i^2} \sum \frac{x_i y_i}{\sigma_i^2} - \sum \frac{x_i}{\sigma_i^2} \sum \frac{y_i}{\sigma_i^2}\right), \qquad (6.2)$$

$$a = intercept = \frac{1}{\Delta}\left(\sum \frac{x_i^2}{\sigma_i^2} \sum \frac{y_i}{\sigma_i^2} - \sum \frac{x_i}{\sigma_i^2} \sum \frac{x_i y_i}{\sigma_i^2}\right), \qquad (6.3)$$

$$\Delta = \sum \frac{1}{\sigma_i^2} \sum \frac{x_i^2}{\sigma_i^2} - \left(\sum \frac{x_i}{\sigma_i^2}\right)^2, \qquad (6.4)$$

$$intercept\ error = \sqrt{\frac{\sum \frac{x_i^2}{\sigma_i^2}}{\Delta}}\ , \qquad (6.5)$$

$$slope\ error = \sqrt{\frac{\sum \frac{1}{\sigma_i^2}}{\Delta}}. \tag{6.6}$$

The fitting values obtained by applying this method are shown in Table 5.3. The two regression curves (Figure 5.8), are almost the same, hence it can be concluded that the ordinary least squares method provides a good fitting for this kind of data. Since the thickness variance is coming from the same source (natural variability of stone), the variance is the same for each specimen.

Table 5.3 Intercept and slope values using the weighted least squares method

	Value	Error
Slope	0.002775	0.0005375
Intercept	17.5	0.5526

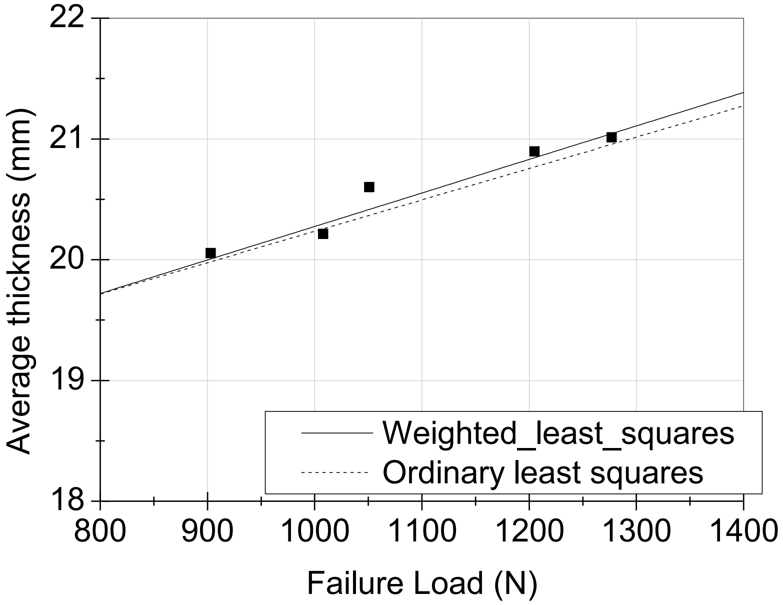

Figure 5.8 Comparison of ordinary least squares and weighted least squares method

b. Propagation of uncertainty

Supposing that Eq. (6.1) best describes $F_{UF}(t)$, we now want to know the failure load of an intact specimen. The interpolated failure load will have an error, and we want to quantify it. Uncertainties in the interpolation of the failure load come from a) the errors already present in the fitting parameters (slope and intercept) and b) the standard deviation of the new thickness measurement. The interpolated quantity F_{UF} will depend not only on *t*, but also on *a* and *b*, and on their errors. The deviation in F_{UF} can be related to the deviation in the dependent variables by using calculus:

$$\delta F_{UF} = \left(\frac{dF_{UF}}{dt}\right)\delta t + \left(\frac{dF_{UF}}{da}\right)\delta a + \left(\frac{dF_{UF}}{db}\right)\delta b \tag{6.7}$$

$$\sigma_F = \sqrt{\left(\frac{dF_{UF}}{dt}\right)^2 \sigma_t^2 + \left(\frac{dF_{UF}}{da}\right)^2 \sigma_a^2 + \left(\frac{dF_{UF}}{db}\right)^2 \sigma_b^2} \tag{6.8}$$

$$t = b \cdot F_{UF} + a\,, \quad \frac{dF_{UF}}{dt} = \frac{1}{b}, \quad \frac{dF_{UF}}{da} = -\frac{1}{b}, \quad \frac{dF_{UF}}{db} = \frac{a - F_{UF}}{b^2}\,. \tag{6.9}$$

Hence, the propagation of the uncertainty in the calculation of a failure load from the derived equation is:

$$\sigma_F = \frac{1}{b}\sqrt{\sigma_t^2 + \sigma_a^2 + \frac{\sigma_b^2}{b^2}(a-t)^2}\,. \tag{6.10}$$

Which means that, for example, a measurement where $t = 20.3\ mm$ and $\sigma_t = 0.25\ mm$ produces a $F_{UF} = 1009\ N$ with an uncertainty of $293\ N$.

c. Weibull analysis

Brittle materials as stone do not deform plastically, but fracture in the elastic regime. Fracture is initiated in the points of discontinuity of the material, which are considered to be homogeneously distributed; more in detail, it nucleates from the defect of the biggest size. This is the so-called "weakest link theory". The distribution of the biggest defects, thus also the distribution of the failure loads, in a sample of tested specimens, is usually and successfully described by the two-parameters Weibull distribution. The probability of specimen failure is given by:

$$P_f = 1 - exp\left(-\left(\frac{\sigma}{\sigma_\theta}\right)^m\right), \tag{6.11}$$

where m is the Weibull modulus (or shape factor), and σ_θ the characteristic stress.

It has been attempted to use Weibull's statistic in the sample of 5 specimens tested statically, although requirements recommend a test sample of at about 30. Due to the impossibility of having a failure stress (σ) in the case of bending of an asymmetric sandwich, it was evaluated the possibility of using, instead of the classic σ , a modified σ'. The definition of a possible σ' has been done in the following ways:

$$\sigma_1' = F_{UF}/t\,, \tag{6.12}$$

$$\sigma_2' = F_{UF}(l_1 - l_2)/2\,t^2, \tag{6.13}$$

The geometry tested are two: the first, referred to as "Geometry 1", is the same that was used for the fatigue tests, and the second, "Geometry 2", has a shorter length (geometric values in Table 5.4).

The parameters m and σ_θ obtained in the two cases are given in

Table 5.5 and Figure 5.9. To each datum, a cumulative probability of failure, P_f, was assigned, and $P_f = (i - 0.5)/n$, where i is the ith datum and n is the total number of data points. An inconsistent flaw population and/or poor testing produce bad Weibull fits. A good fit is usually synonym of a single flaw type and confirmation of care in testing procedures. Kinks in the distribution function usually indicate fracture from multiple flaw types.

Table 5.4 Geometries of the specimens tested for the Weibull distribution determination

	b (mm)	l_1 (mm)	l_2 (mm)
Geometry 1	50	250	83.3
Geometry 2	50	200	66.6

Table 5.5 Weibull parameters for Geometry 1 and Geometry 2.

	Geometry 1		Geometry 2	
	σ_1'	σ_2'	σ_1'	σ_2'
Weibull modulus (m)	9.6	11.4	21.9	23.2
Characteristic stress (σ_θ)	55.14	2253	83.9	2665

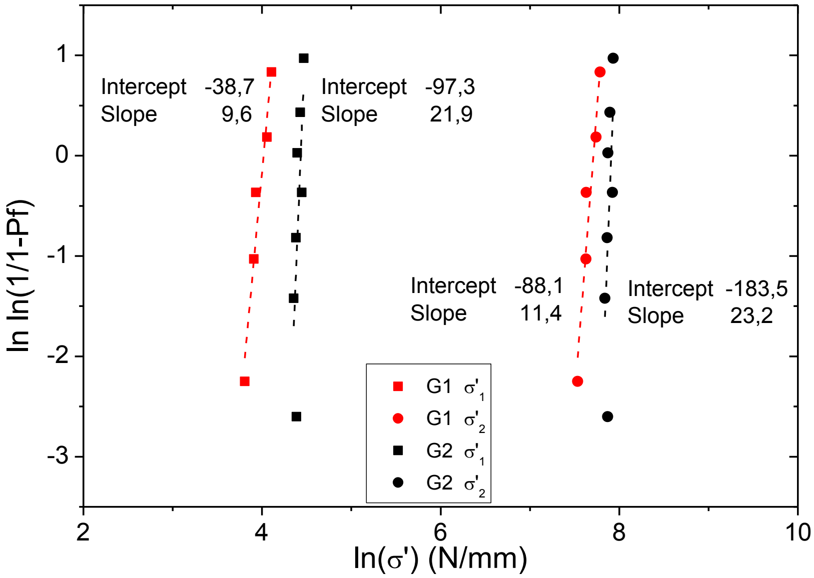

Figure 5.9 Graphical representation of the Weibull analysis results. To each datum, a cumulative probability of failure, P_f, was assigned, and $P_f = (i - 0.5)/n$, where i is the ith datum and n is the total number of data points.

Flexural tests on different geometries do not produce the same failure load. In homogeneous materials with equal cross sections, the maximum stress is proportional to the bending moment, thus to the force multiplied by the lever arm. The σ_2' tries to substitute the real stress, due to the difficulty of defining a moment of inertia. In a Weibull analysis on different geometries one must also consider size effects, because a bigger volume loaded at a certain stress would yield a higher probability of finding a critical size defect with respect to a smaller volume at the same load. In this case, no volume correction has been applied because, since the failure occurs below the loading pins, the loaded volume can be considered equal. Therefore, the only difference between the two cases is the lever arm, which is accounted for in σ_2'.

Figure 5.9 shows that the two tests have different modulus m, which reflects the dispersion of results, being a higher modulus related to a lower variability. The results indicate that the tests, which were made on the same material but cut at different times, have a failure distribution which is not comparable. It is thus impossible to infer failure distributions on different geometries or material batches.

d. Normal distribution

If, on the other hand, a normal distribution of failure loads, instead of a Weibull distribution, is hypothesized the parameters of the probability distribution are:

Average Load μ	1089 N
Standard Deviation σ	151 N

This means that there is a probability of 63% for the next tested specimen to have a failure load between (1089-151) and (1089+151) N.

5.2 Fatigue tests

The maximum force (F_{MAX}) of the fatigue cycle is always calculated as a percentage of the static failure load; from now on, the expression "load percentage" is used for brevity to indicate the ratio F_{MAX}/F_{UF}.
Two types of tests have been conducted: a) continuous tests up to failure or 500'000 cycles, and b) tests with a resting time after a defined block of cycles. Tests of the second category were performed to see if the number of cycles at failure was the same with respect to the same load percentage.

5.2.1 Continuous tests

Hereafter, the results of the two materials tested are summarized.

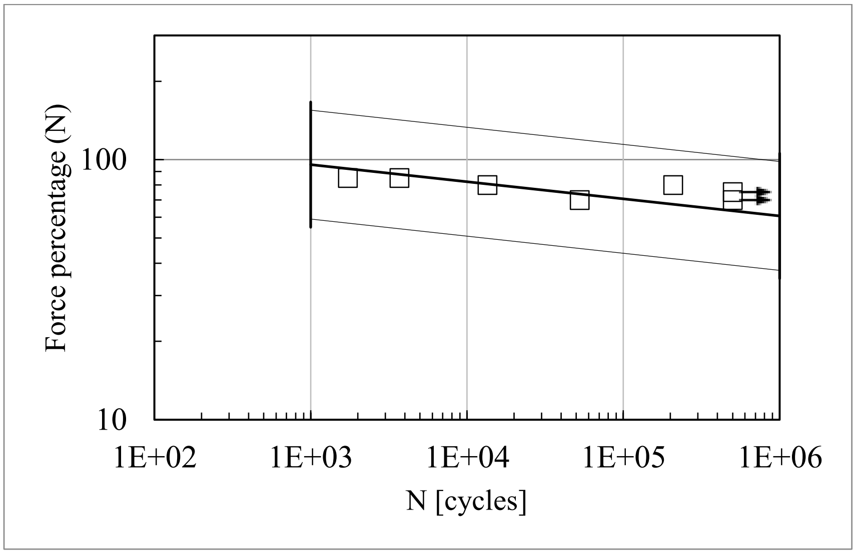

Figure 5.10 Fatigue curve of L1C1. The points with arrows indicate run-outs; the bands indicate a survival probability of 10-90%.

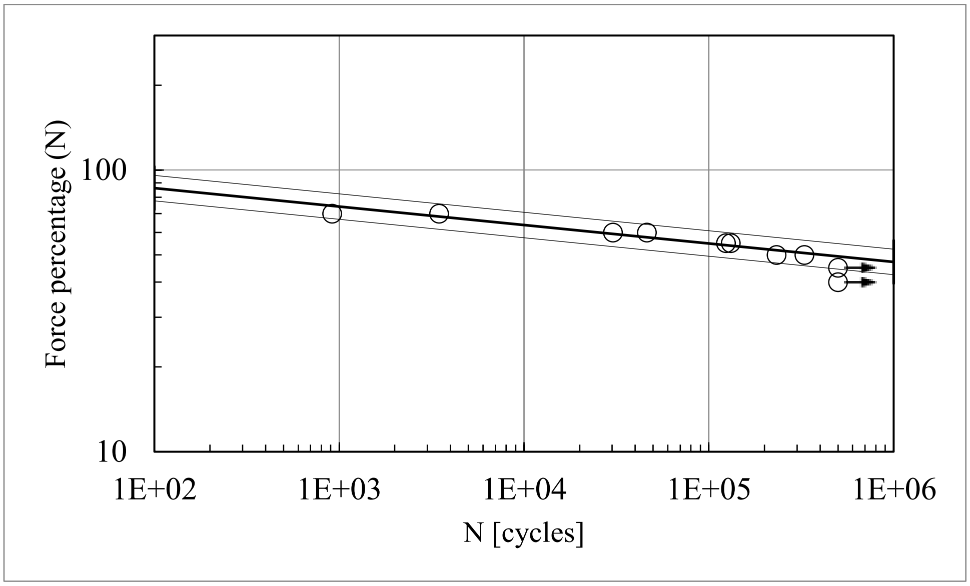

Figure 5.11 Fatigue curve of L2C1.

a. Trends

The first series of graphs, Figure 5.12, shows the trends of accumulated deformation, relative stiffness, absolute stiffness, and energy along the cycles for the various load percentages. The second series of graphs, Figure 5.13, illustrates the value of the cited quantities, in the cycle preceding failure.

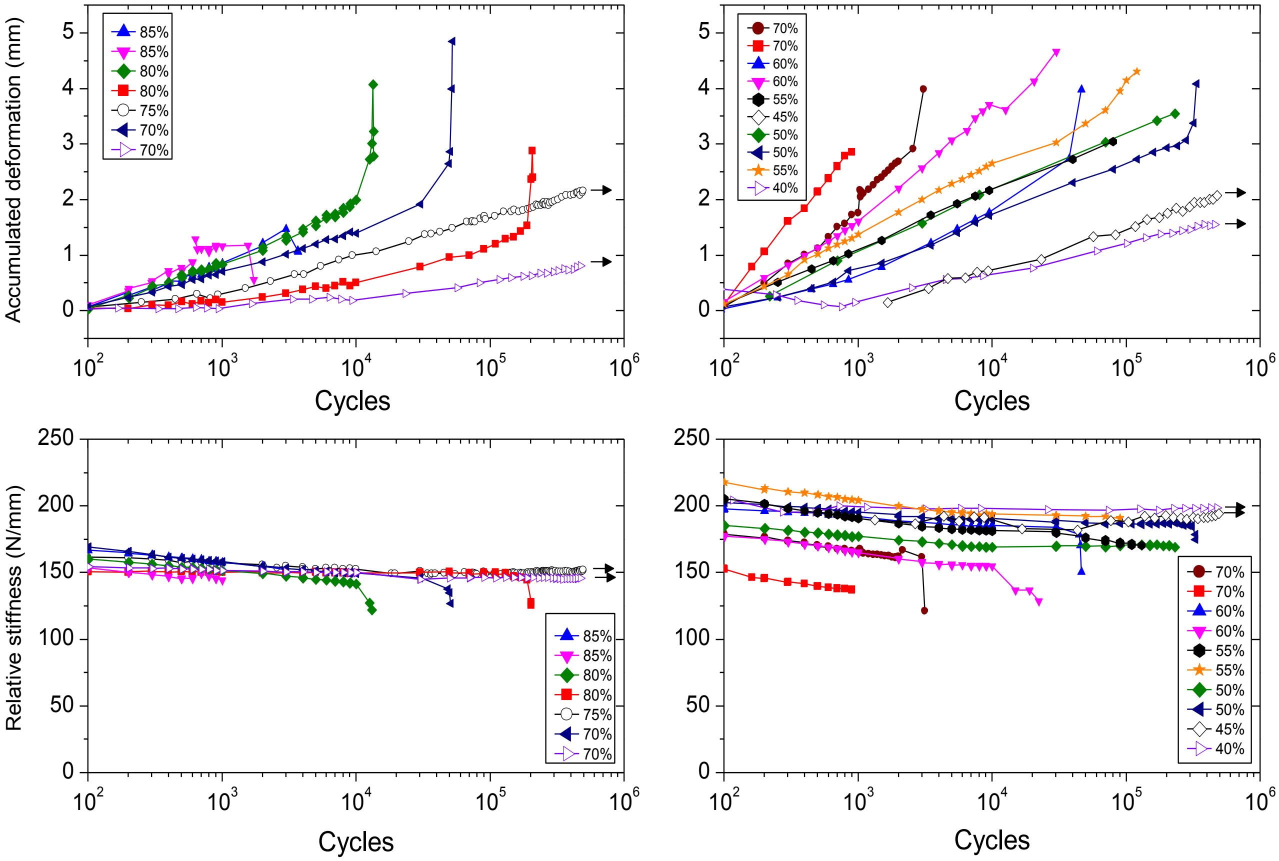

Accumulated deformation (mm)
Relative stiffness (N/mm)
Cycles
85%
85%
80%
80%
75%
70%
70%
60%
60%
55%
45%
50%
50%
55%
40%
0
1
2
3
4
5
50
100
150
200
250
10^2
10^3
10^4
10^5
10^6

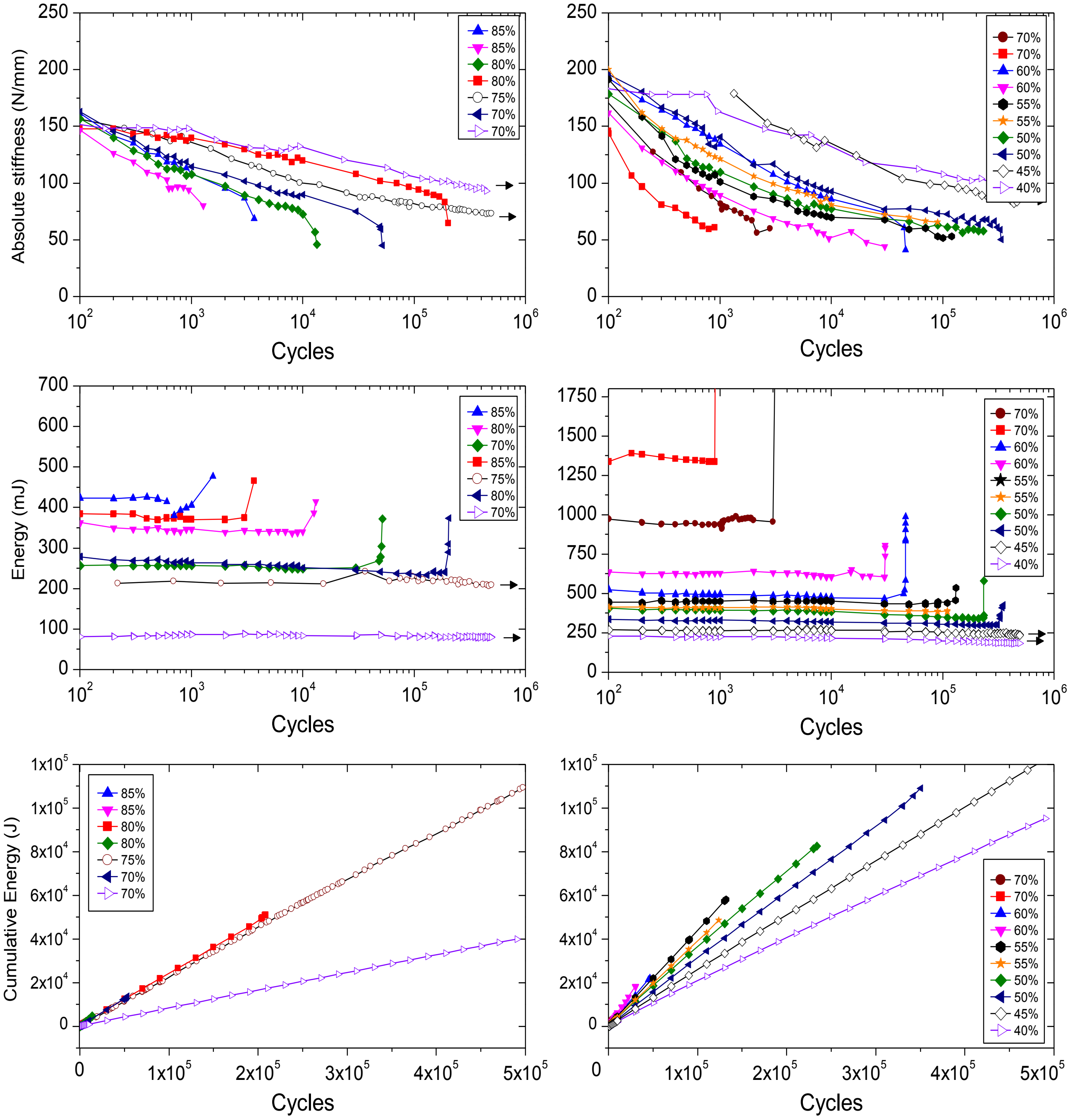

Figure 5.12 Trend of the quantities 1) accumulated deformation, 2) relative stiffness, 3) absolute stiffness, 4) dissipated energy, and 5) cumulative energy along the cycles for L1C1 and L2C1

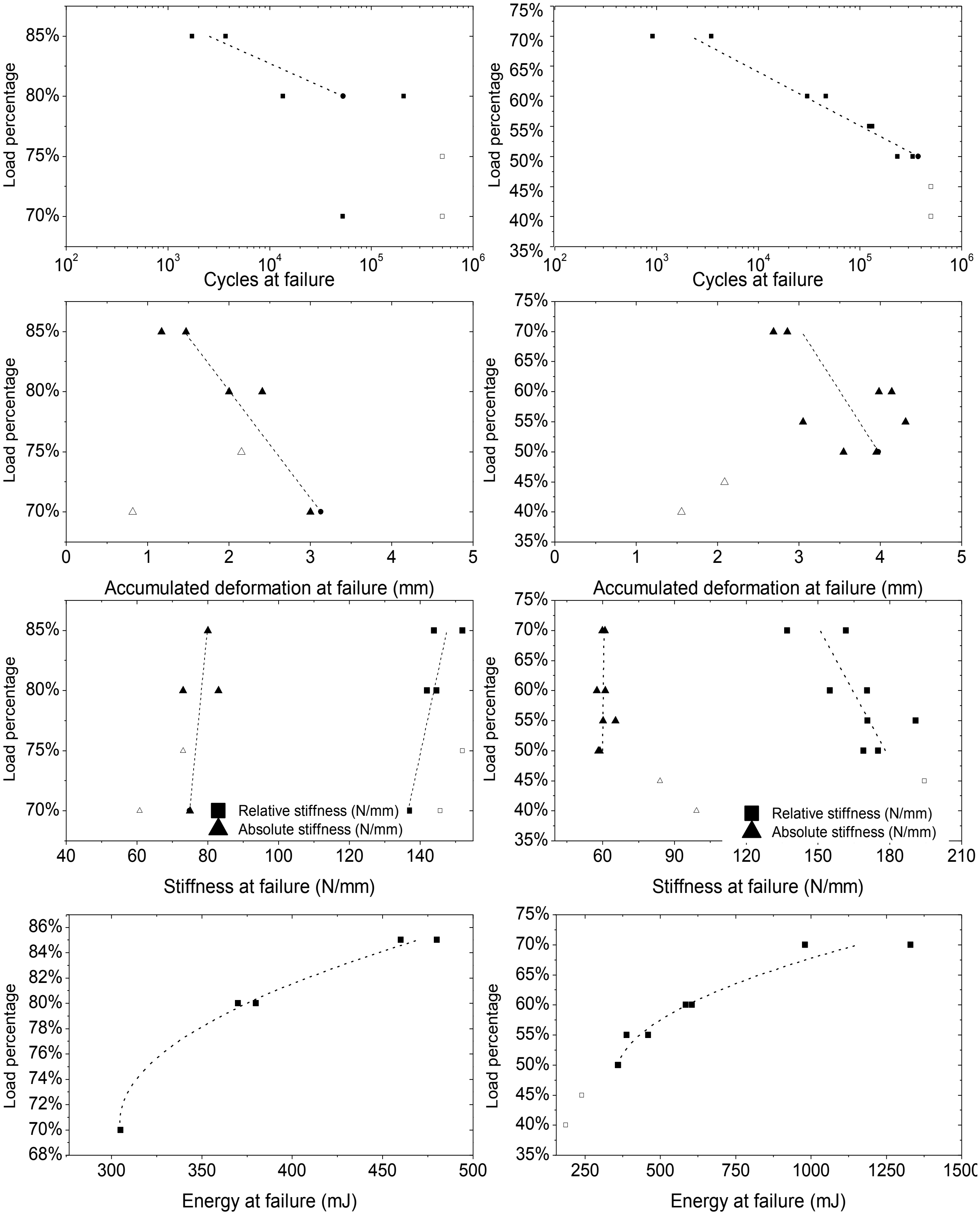

Figure 5.13 Summary of the values of the calculated fatigue quantities in the cycle preceding failure

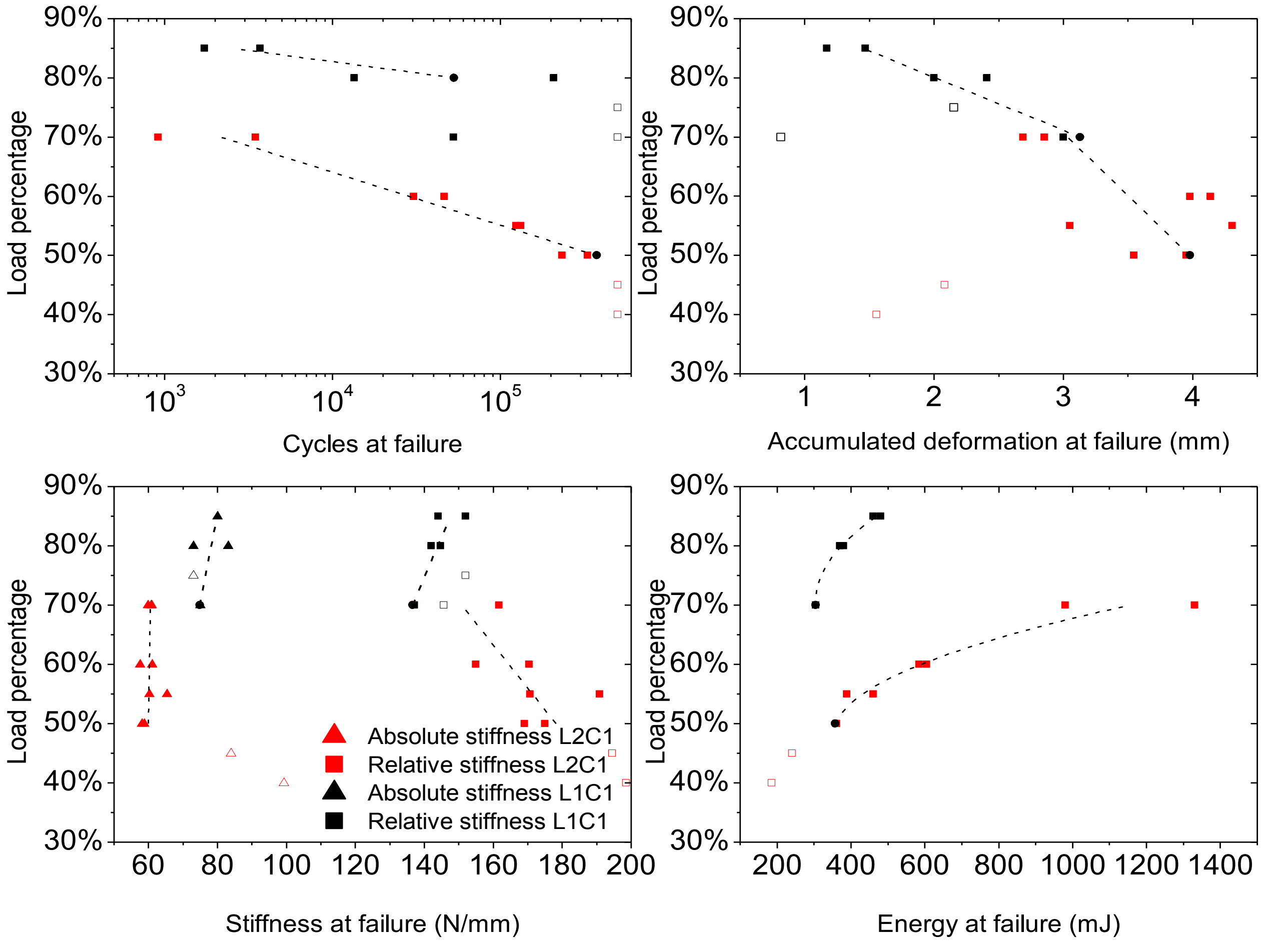

Figure 5.14 Summary of the value at failure of the calculated parameters including the two materials on the same graph. The red symbols refer to L2C1, the black to L1C1. Empty symbols, both black and red, refer to specimen that did not fail.

b. Observation of damage and failure

The material L1C1 showed cracks under the load application point, in all the cases analyzed. Failure occurred due to crushing of the stone layer because the piston generated localized stresses that overcame the compression resistance of the limestone. The material L2C1 instead showed different modes of failure according to the applied load percentage. For $F_{MAX} > 60\%\ F_{UF}$ failure occurred due to indentation of the limestone, as was in L1C1 (Figure 5.15).

For $45\%\ F_{UF} < F_{MAX} < 55\%\ F_{UF}$, a change in failure mode was observed. At $F_{MAX} = 55\%\ F_{UF}$ two specimens were tested, which showed two failure modes: in one case, a crack under the load application point was formed (Figure 5.16 left); in the other case failure occurred because of breakage of the lower layer fibers, and crack propagation in the cork layer in the direction of maximum shear stress (Figure 5.16 center). The fibers fracture on the vertical under the load pin, where shear stress and bending moment are maximum. For $F_{MAX} < 45\%\ F_{UF}$, no fracture was observed. The failure modes for each applied load percentage are shown in Figure 5.17

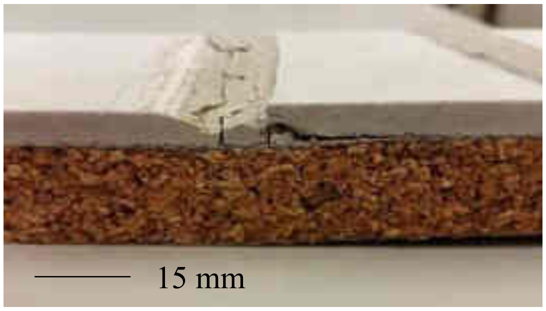

Figure 5.15 Failure for stone crushing after 30'000 cycles of L2C1 tested at 60% F_{UF}

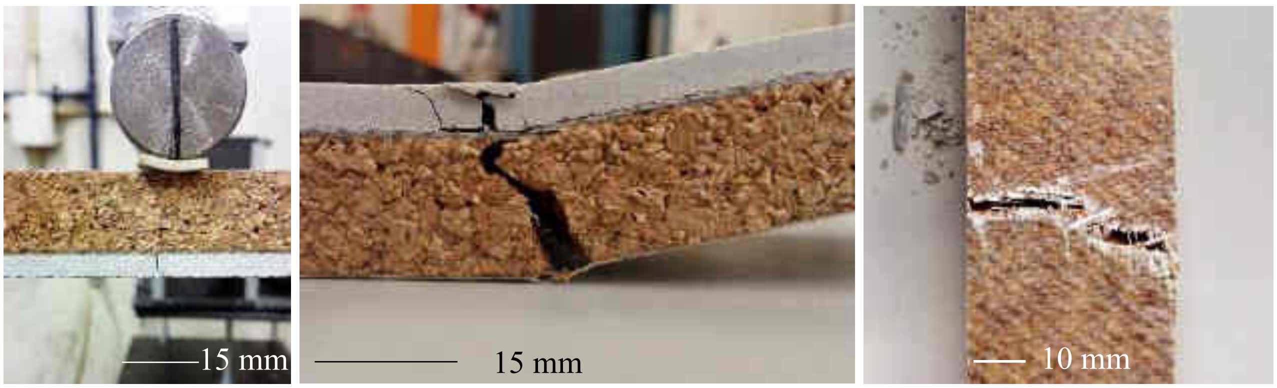

Figure 5.16 Failure modes observed for load percentage 55% (L2C1). Left: fracture of the limestone (the picture was taken in "reversed configuration" applying a tensional load on the stone to open the crack, for it to be easily seen. Center: fracture nucleated on the lower fibers. Right: picture of the fractured fibers.

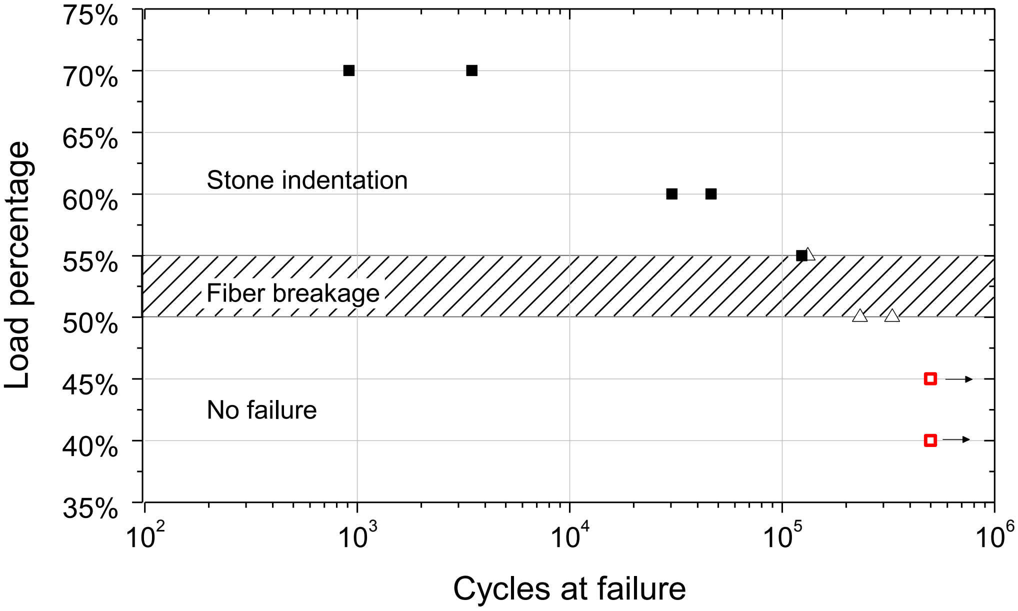

Figure 5.17 Failure mode map for L2C1.

5.2.2 Tests with resting time (L2C1)

a. Trends

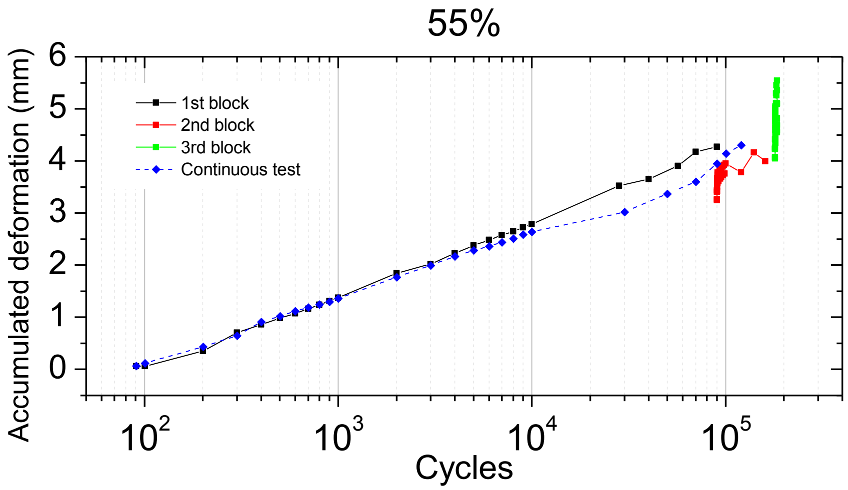
55%

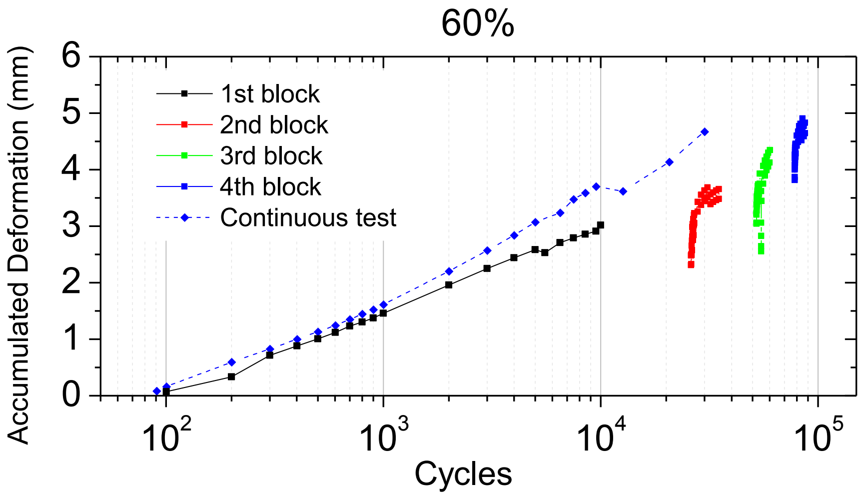
60%

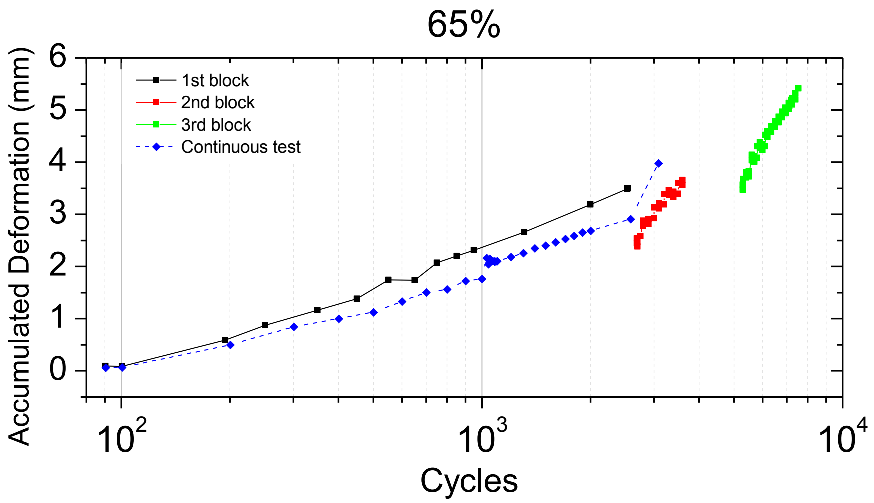
65%

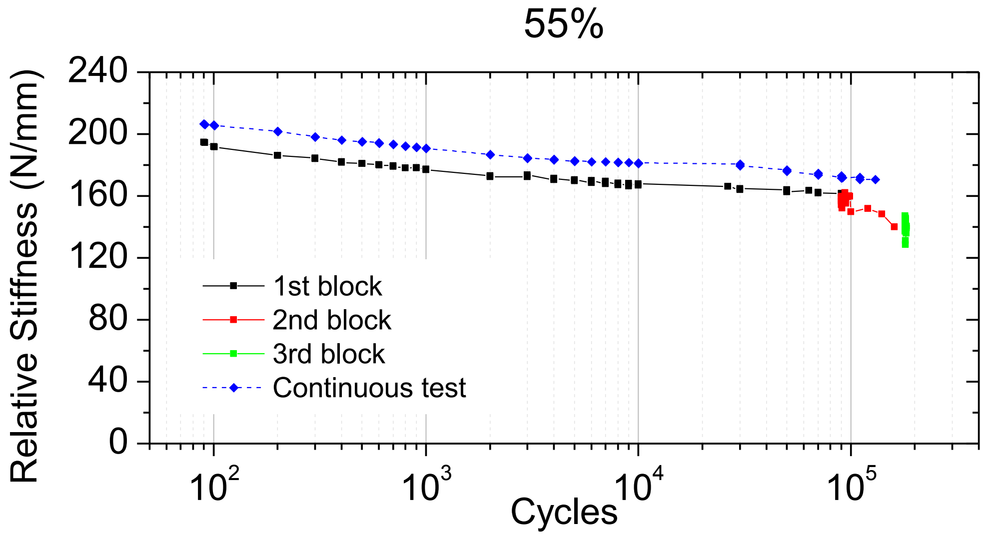
55%
Relative Stiffness (N/mm)
240
200
160
120
80
40
0
10^2
10^3
10^4
10^5
Cycles
1st block
2nd block
3rd block
Continuous test

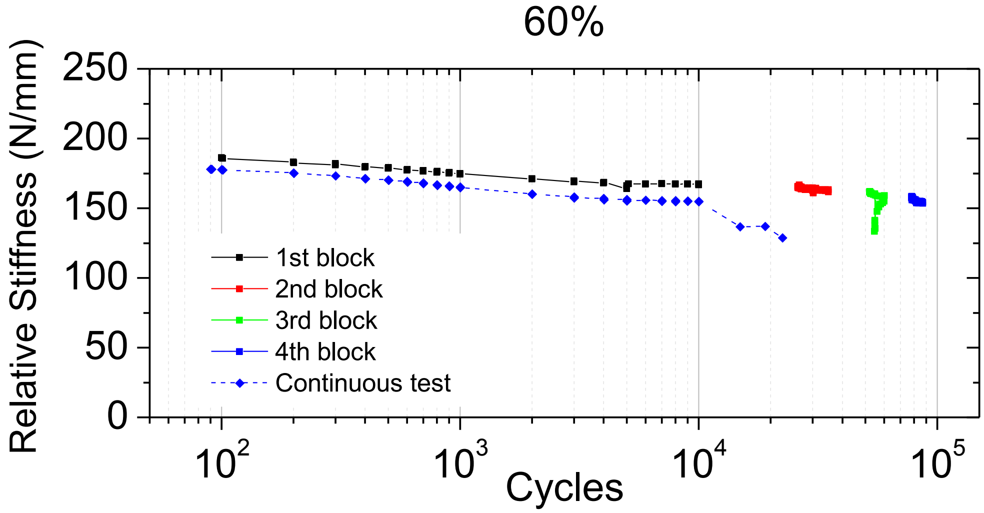
60%
Relative Stiffness (N/mm)
250
200
150
100
50
0
10^2
10^3
10^4
10^5
Cycles
1st block
2nd block
3rd block
4th block
Continuous test

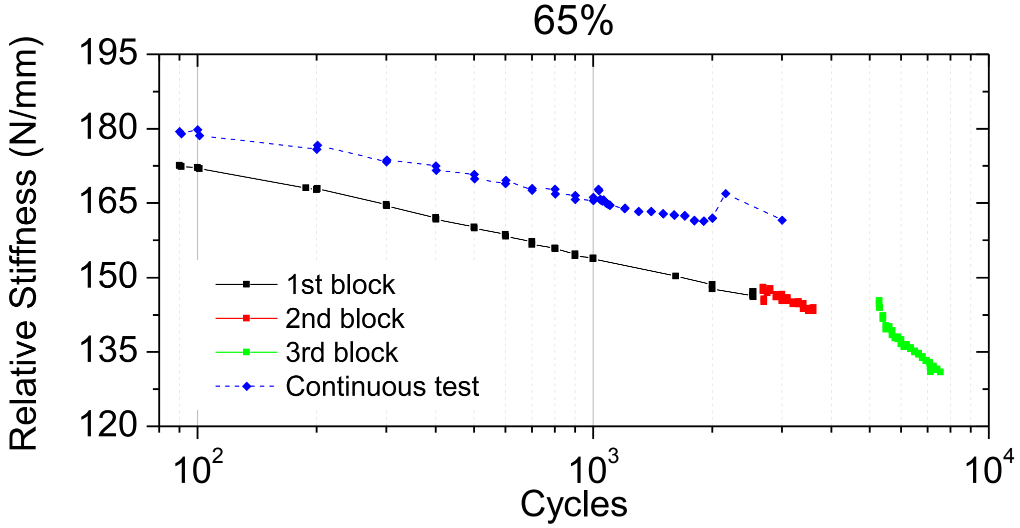
65%
Relative Stiffness (N/mm)
195
180
165
150
135
120
10^2
10^3
10^4
Cycles
1st block
2nd block
3rd block
Continuous test

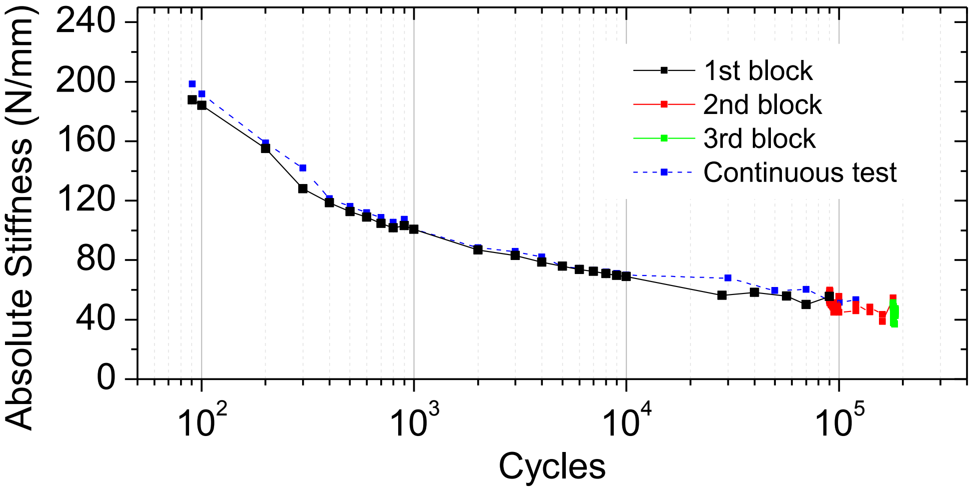

55%

Absolute Stiffness (N/mm)
240
200
160
120
80
40
0
10^2
10^3
10^4
10^5
Cycles
1st block
2nd block
3rd block
Continuous test

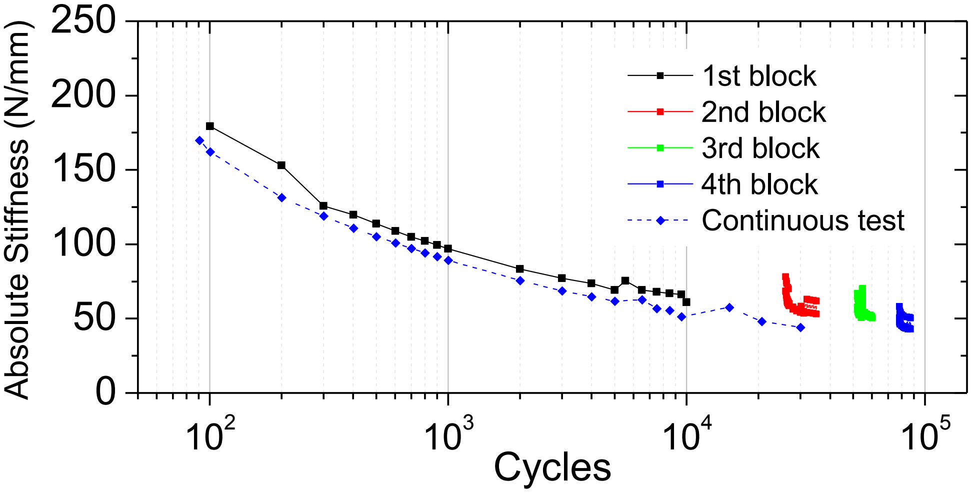

60%

Absolute Stiffness (N/mm)
250
200
150
100
50
0
10^2
10^3
10^4
10^5
Cycles
1st block
2nd block
3rd block
4th block
Continuous test

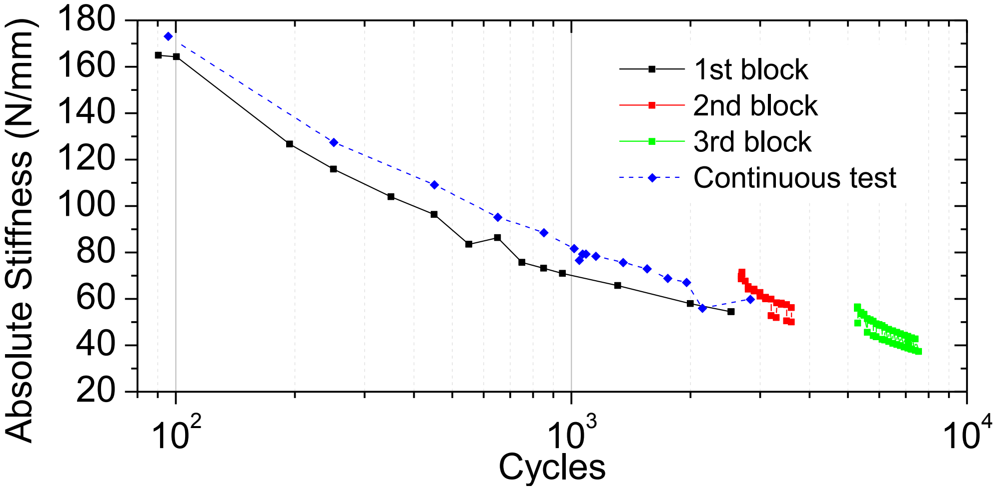

65%

Absolute Stiffness (N/mm)
180
160
140
120
100
80
60
40
20
10^2
10^3
10^4
Cycles
1st block
2nd block
3rd block
Continuous test

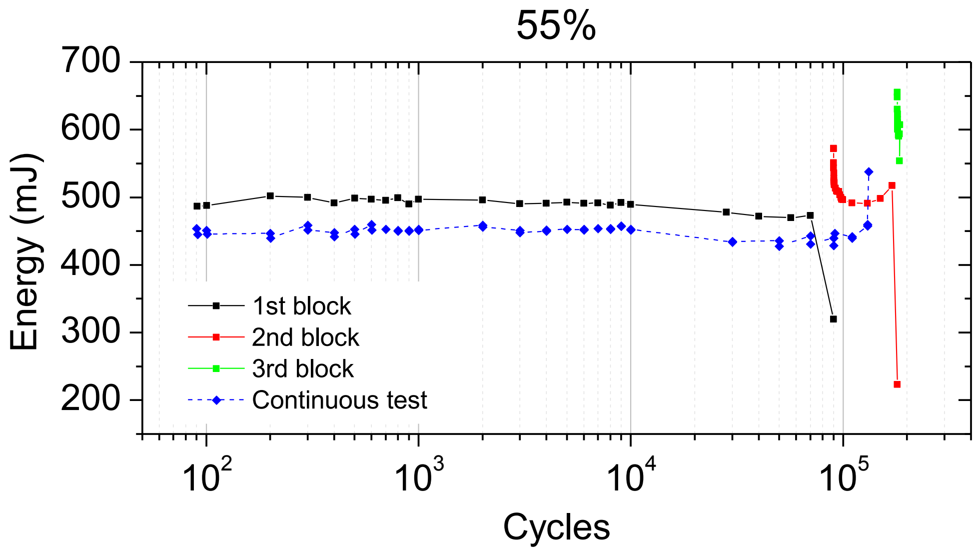
55%

Energy (mJ)
700
600
500
400
300
200
Cycles
10^2
10^3
10^4
10^5
1st block
2nd block
3rd block
Continuous test

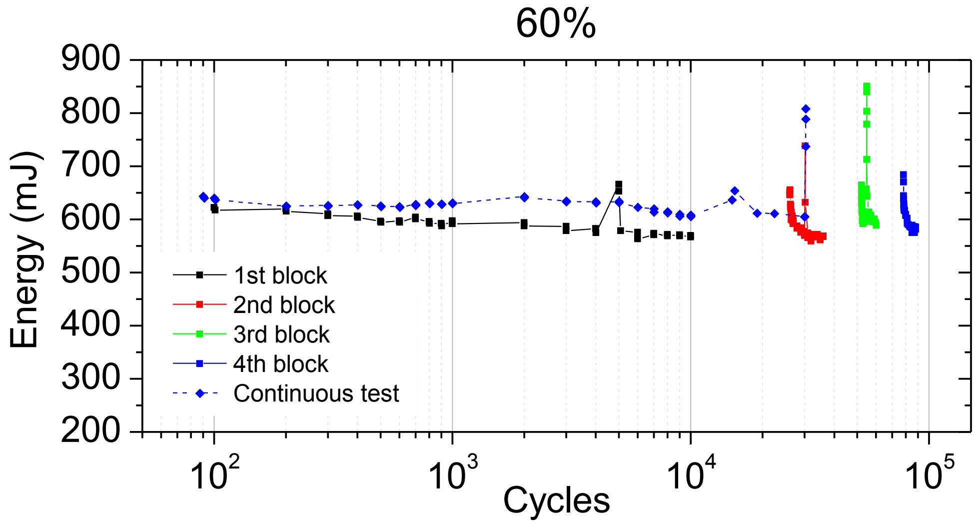
60%

Energy (mJ)
900
800
700
600
500
400
300
200
Cycles
10^2
10^3
10^4
10^5
1st block
2nd block
3rd block
4th block
Continuous test

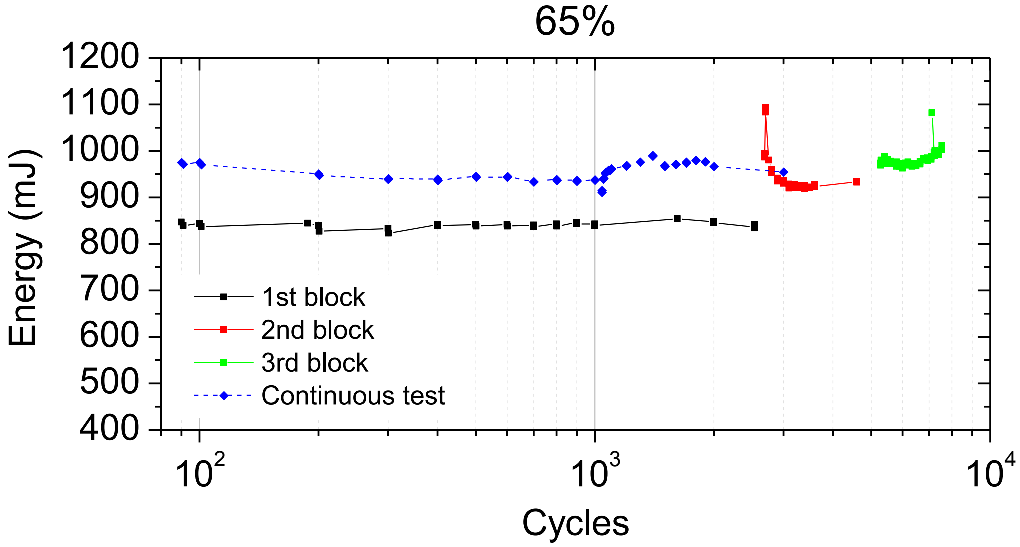
65%

Energy (mJ)
1200
1100
1000
900
800
700
600
500
400
Cycles
10^2
10^3
10^4
1st block
2nd block
3rd block
Continuous test

b. Observation of failure

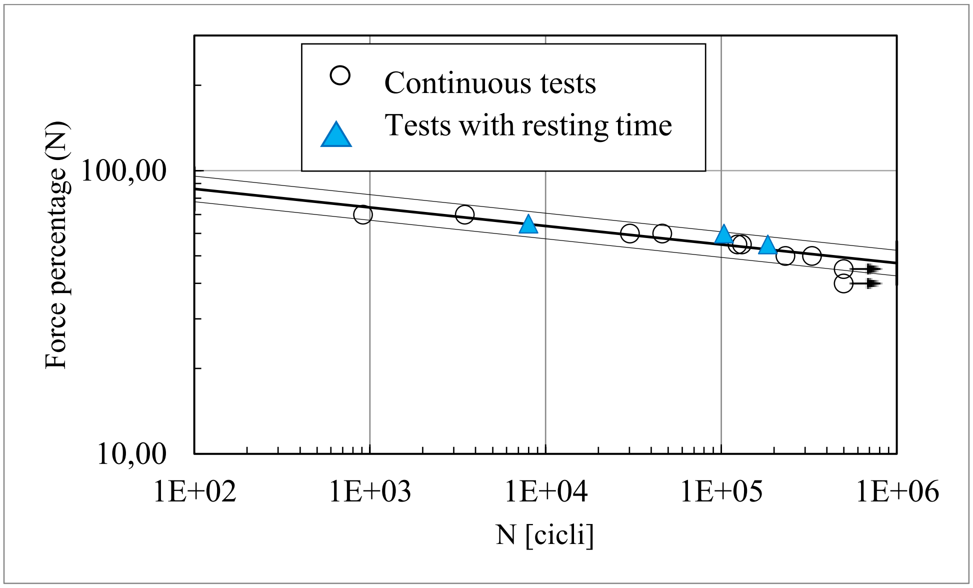

Figure 5.18 Fatigue curve of L2C1 with indication of tests with resting time.

The test at 45% did not show any sign of failure after two blocks of 500’000 cycles. The tests at 55, 60, and 60% instead failed showing a common feature: multiple macrocracks at 45° orientation on the cork layer located at the right- and at the left-side of the left and right roller, respectively (Figure 5.19). Such cracks are due to shear forces; the cracks follow the border of the granules, where they are coated with the adhesive.

Figure 5.19 Macro-cracks on the cork layer on the fatigue tests with resting time. Load percentages are specified on the images.

Additional damage was observed for the specimen tested at 60% after the 4th block, in the form of a crack in the stone, and whiting of the lower layer resin (

Figure *5.20*). The whiting follows the pattern of the glass fabric, which, due to its nature and the difficulty in manufacturing, happened to be with undulations.

Figure 5.20 Specimen tested at 60% with resting time. Left: crack on the stone. Right: whiting of the resin.

c. X-ray CT

Here reported is an example of the images taken from the X-ray CT of samples drilled near the inner loading point of L1C1 and L2C1 specimens. The cracks could be identified only after a long search, and can be easily confused with the natural microstructure of the stone, being this porous and heterogeneous. Figure 5.21 shows the most X-ray opaque points in the stone layer, and Figure 5.22 shows the pattern of the first glass fibers' layer. The intensity of radiation which stone and cork absorb belong to two different ranges; at the intensity in which the stone is visible, cork isn't. Therefore, only one layer at a time can be seen.

Cracks in L1C1 specimens could be discerned more easily than those in L2C1, but nevertheless no quantitative nor qualitative conclusion can be drawn from them. Only one frame of L2C1 is reported, because it was the only crack found within the tomographies.

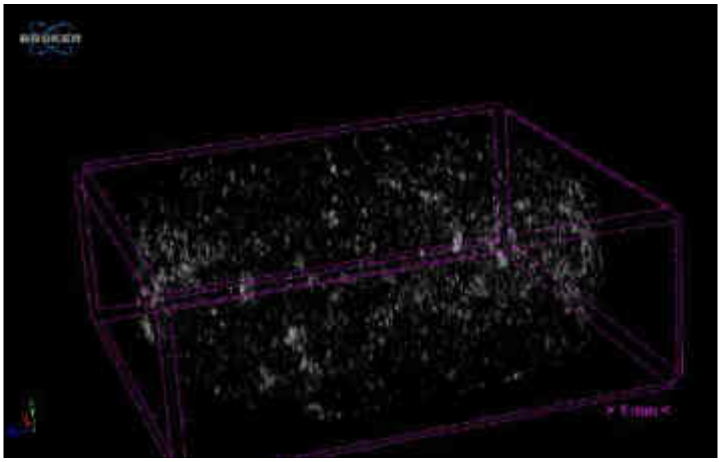

Figure 5.21 L1C1, zones of higher density (more opaque to radiation)

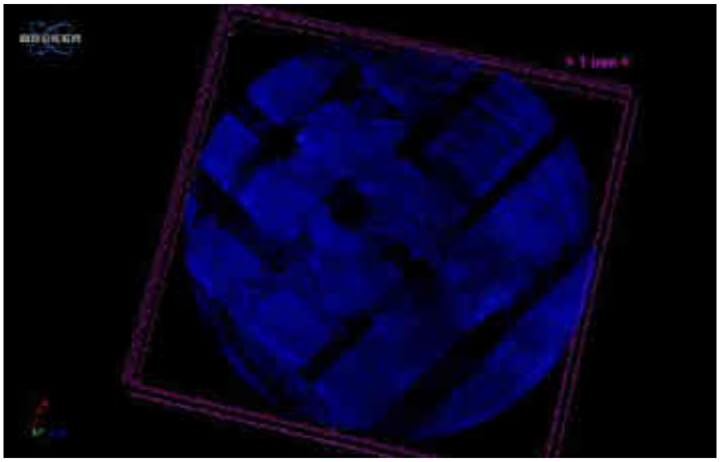

Figure 5.22 Glass fibers

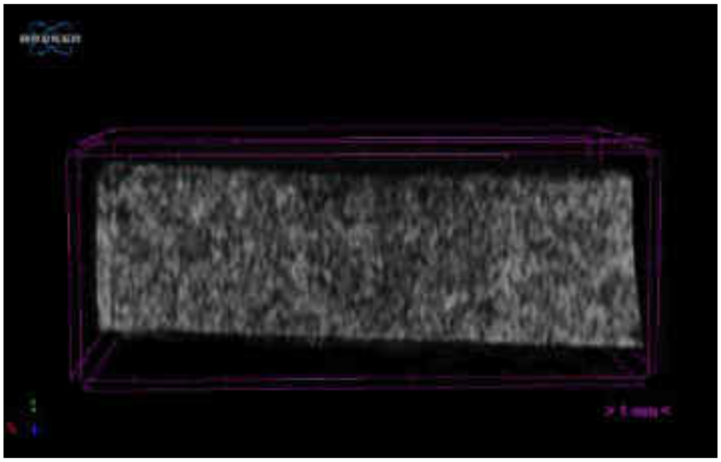

Figure 5.23 L1C1 $F_{MAX} = 85\%\ F_{UF}$

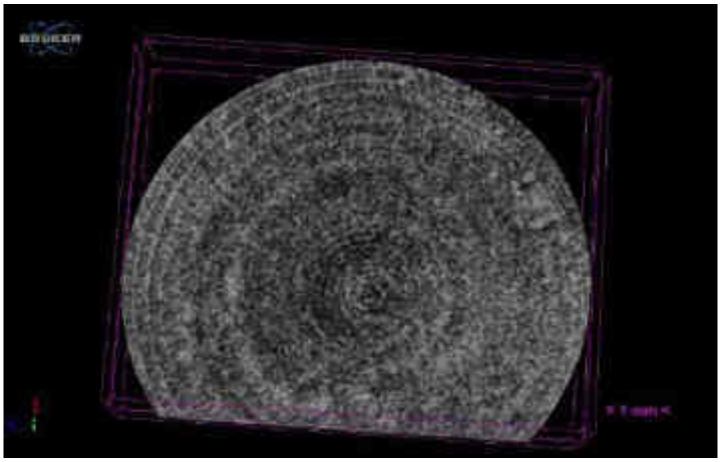

Figure 5.24 L1C1 $F_{MAX} = 85\%\ F_{UF}$

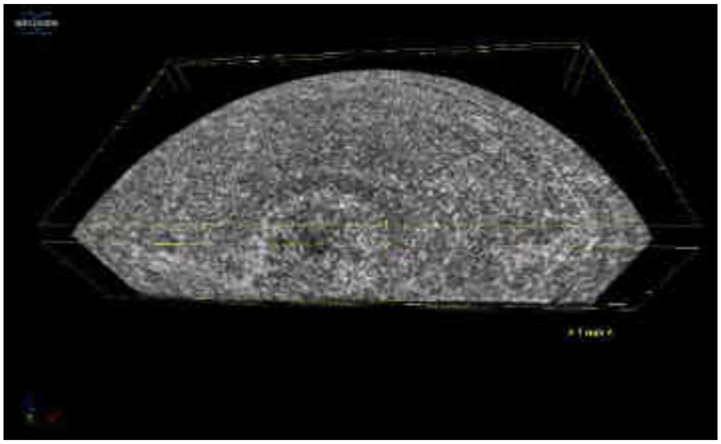

Figure 5.25 L1C1 $F_{MAX} = 85\% \, F_{UF}$

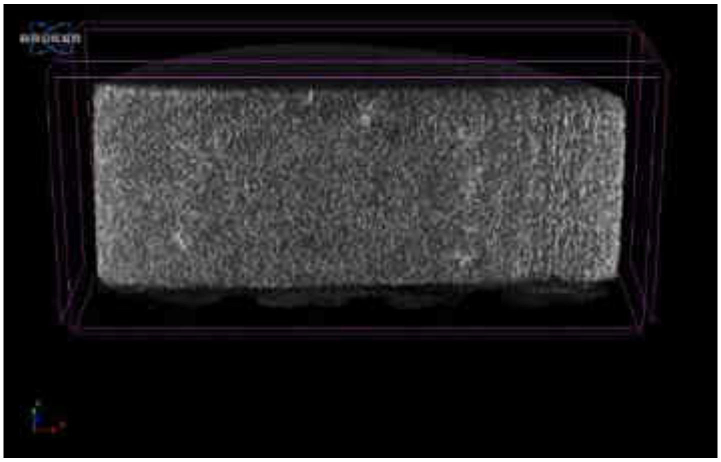

Figure 5.26 L2C1 $F_{MAX} = 85\% \, F_{UF}$

Chapter 6.

Discussion of the results

6.1 Accumulated deformation

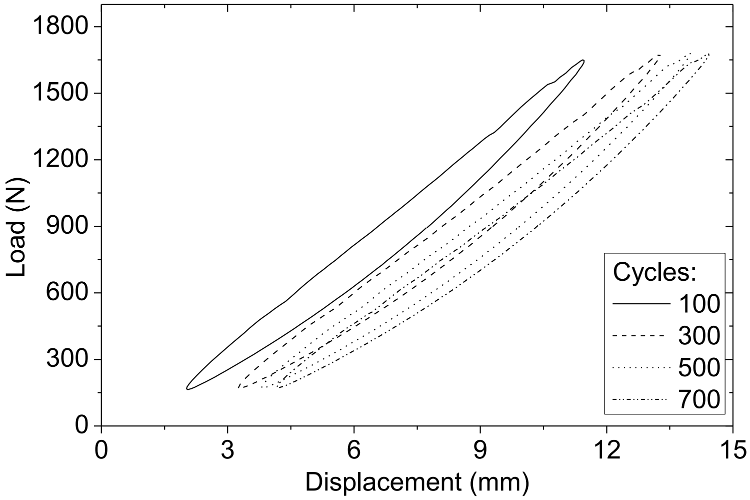

Figure 6.1 Load-displacement loops of a specimen L2C1 tested at 70% for cycles 100, 300, 500, 700.

The accumulated deformation (d_{acc}) is the difference between the position of the piston at load *x* (with *x*=300 N for L1C1 and 600 N for L2C1) for cycle *j* and the position of the piston at load *x* for the first cycle. Therefore, it represents a value of deformation accumulated by the material instantaneously. After a resting period, such as that of 24 hours in the fatigue tests with stops, some of that deformation was recovered.

For both materials, d_{acc} shows a linear **trend** in logarithmic x-scale, meaning that there is a rapid increase until about 10^4 cycles, after which, unless the material fails shortly after, it stabilizes to a plateau. Curves tend to have higher **stabilization deformation** for increased load percentages, although for L1C1 a curve at (theoretical) load percentage of 80% has lower d_{acc} than the one at 70%. Material L2C1 shows a more regular behavior, with linear curves and approximately decreasing slope for decreasing load percentage.

The fact that all curves for the two materials have a linear trend, or logarithmic trend in linear scale, means that there always is an initial period during which the material loses part of its stiffness. The number of cycles until stabilization is, for both materials, 10’000 cycles. As shown by the test with stops, the loss in stiffness is permanent.

The trends of the curves showing infinite life in L1C1 (70% and 75%) are similar, with higher value of d_{acc} of the stabilization plateau for the curve at 75%. The value of d_{acc} for the plateau of infinite life specimens is 0.85 and 2.2 mm for L1C1, 1.56 and 2.0 mm for L2C1. The difference in the plateau value might be due to the different maximum load in the four cases: higher F_{MAX} in absolute terms induces higher penetration of the rollers on the cork side, thus generates a higher d_{acc}.

Overall, the d_{acc} at failure for L2C1 is set at higher values than for the other configuration (3 to 4 mm versus 1 to 3 mm); the cause could be found in the higher compressive resistance of the stone L2. Normal stresses that arise from bending are sustained for the greatest part by the limestone; therefore, a stone with low compressive strength associated to an increase in the mean displacement along the cycles, fails at lower accumulated displacement than one with a higher compressive resistance.

According to the load percentage used, three cases can be distinguished in L1C1 and L2C1:

1) The material does not show stabilization, but fails at very low number of cycles; this can be due to a permanent damage induced by the high load. This failure is equal to a static failure of the composite.
2) The material stabilizes, but breaks before reaching 500’000 cycles. In this case, since d_{acc} keeps the same plateau value; failure is due to the detrimental effect of fatigue on one of the layers.
3) No failure occurs before 500’000 cycles, d_{acc} has stabilized to a lower value than the previous cases. In this case, one must also take into account the penetration of the rollers on the cork side, which leads to the wrong conclusion that d_{acc} might still increase along the cycles.

In the second and third case, deformation accumulates faster for higher than for lower load percentages, thus the plateau of d_{acc} is set to higher values. This could be due to two factors:

- At frequency and R constant, increasing F_{MAX} means that the loading pin travels faster, hence the material has less time to recover the deformation. The correctness of this assumption could be checked performing the fatigue tests at constant velocity instead of constant frequency.
- Higher forces F_{MAX} cause more permanent damage in the material, which loses its stiffness.

The trend of d_{acc} at failure in L1C1 from Figure 5.13 seems to be inferring that lower load percentages have higher accumulated displacement at failure, although again, the penetration of the rollers on the cork is not considered. The same happens for L2C1, although the data are more scattered.

6.2 Relative and absolute stiffness

Relative stiffness is the slope of the load-displacement curve between the two values mentioned in § 4.2. L1C1 always shows an initial decrease until stabilization at a constant value, which is maintained until before failure. Materials showing infinite life have a curve with slope zero and similar value of relative stiffness (145-150 N/mm): this is a confirmation of the homogeneity of the stone composition.

Three cases are observed in L1C1:

1) When there is infinite life, the stiffness does not fall below 90% of the stiffness of 100th cycle.

2) In the case of failure at high cycles (70 and 80%), the value of stiffness before failure, when stone macrocracks are already visible, is 80-85% of stiffness of the 100th cycle.
3) In the case of failure at low cycles, the value of stiffness is 94% and 85% stiffness of the 100th cycle.

Researchers have been using as failure criterion the decrease of relative stiffness below a certain percentage of the initial stiffness (El Mahi et al. 2004). Here this is not an effective criterion for determining failure. In fact, failure in cases 2) and 3) might have different causes: at low cycles it is caused by the impact of the rim on the stone, at high cycles by the displacement and a probable fatigue effect.

L2C1 shows the same trend as L1C1: an initial stiffness decrease, and a stabilization for high number of cycles. For specimens tested at lower loads, the stiffness value is comprised in a tight range (about 40 N/mm), again demonstrating homogeneity in the microstructure of the limestone. Nevertheless, for higher load percentages D_{rel} does not stabilize, and decreases at a higher rate.

The initial decrease of D_{rel} (until 10^3 cycles) is shown both for L1C1 and L2C1, and can be attributed to a damage of the cork layer, since it is the layer in common of the two configurations, and the one that shows the viscoelastic behavior; it is the same damage that was visible in the d_{acc} graphs. Instead, a faster decrease in stiffness for load percentages above 60 in L2C1 could indicate another damage mechanism, probably on the stone, since it is the stone that fails due to crushing. At higher loads the damage happens faster; before the 100th cycles shown on the graphs, the cork already lost its initial stiffness, increasing the bending displacement. Higher displacements at constant frequency, and slow recovery of deformation induce the composite to be loaded abruptly, until the repeated impact of the loading pin on the stone generates failure.

The trend of D_{rel} at failure according to the load percentage (Figure 5.13) seems to have inverse slope for the two materials, but always within a small range, therefore it could be associated with the natural variability of the stone material.

The absolute stiffness was introduced to have one parameter that contains information about the stiffness decrease and about the instantaneously accumulated deformation. All curves in L1C1 can be described by a relation like $D_{abs} = \log(cycles)^a + D_{abs,0}$ where a is the slope of the curves, while curves in L2C1 have a positive concavity. Interestingly, all curves in L1C1 fail at a value $D_{abs} = 70$ N/mm, while in L2C1 they fail at a similar value of 60 N/mm.

6.3 Energy

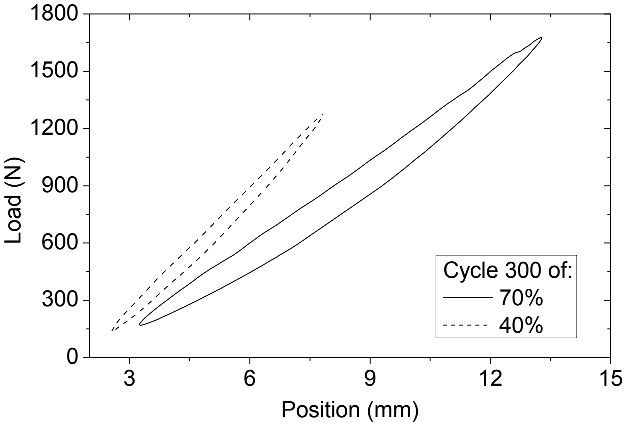

Figure 6.2 Hysteretic loop of the 300^{th} *cycle for load percentages of 70 and 40 (L2C1). The area inside the loop is the dissipated energy.*

The graphs of dissipated energy per cycle show whether there is or not a variation in the shape of the hysteretic loops, which in turn is an indication of occurrence of energy dissipating processes. The hysteresis arises due to the non-linearity in the force-displacement relationship of the composite. Irreversible processes responsible for energy dissipation can be: compaction of the stone, stone microcracking, resin cracking, or heat generation, among others.

Specimens with the highest absorbed energy per cycle fail at the lowest number of cycles, for both materials. L2C1 graph indicates that the energy absorbed per cycle increases for higher maximum loads, as it is expected, because they are associated to increasing values of F_{MAX}. Moreover, in all cases the plateau energy value is constant until failure, following the same trend as the relative stiffness. This confirms that there are not additional relevant damage processes before failure.

For configuration L1C1, since the load percentage is related to F_{MAX} through the thickness variable, a higher load percentage does not always correspond to higher F_{MAX}. Therefore, the curve at theoretical load 70% that shows no failure absorbs half the energy with respect to the specimen showing infinite life at 75% just because the load extremes are 56-560 N (against the 84-840 N).

There is a difference of about 250 mJ between two L2C1 specimens theoretically loaded at the same value (70%). This difference can be attributed to the fact either that a) possible defects accelerate the damaging process, or b) a difference in stone thickness makes the effective load percentage higher than 70%, for the specimen that failed at lower N_f. The second hypothesis would be discarded, if the idea that energy absorption depends on the load interval, and not on the load percentage, is considered correct.

The curves for cumulative energy showed a predictable trend: looking at L2C1, specimens tested at lower load percentages absorb less energy per cycles, therefore accumulate energy more slowly, and their slope is lower than for specimens which fail sooner. Overall, the cumulated energy at break is not constant, but higher for specimens that last longer. This means that the mechanisms inducing energy dissipation in infinite-life specimens do not degrade the properties of the material, because of an equilibrium between energy dissipation – probably in the form of heat – and thermal exchange with the environment.

6.4 Fatigue tests with resting time

The most evident results of this kind of tests are:

- The specimens last longer than in continuous tests, for equal load percentages, but nonetheless their lifetime is within the 10-90% confidence band. Therefore, there is not enough evidence to prove that the resting time leads to a longer lifetime.
- There is permanent damage, as can be deduced by a) the relative stiffness not going back to the initial value, and b) the d_{acc} rapidly reassuming the value it had before the resting time.

The graphs of absorbed energy along cycles are also peculiar: for 55, 60, and 65 % the energy dissipated in blocks other than the first has a high initial value, then decreases. The resting induces recovery of some viscoelastic deformations, recovery which is lost again at the beginning of each new block. It is unclear whether the recovery is in the cork, in the stone, or in the fibers.

6.5 X-ray CT

Computerized tomographies were performed in order to have a qualitative understanding on whether the stone layer forms microcracks after loading. It was found that in material L1C1, some cracks are visible in the direction parallel and perpendicular to the loading pin, at all percentage of maximum force. In material L2C1, the number of cracks found was much lower.

It is important to be aware of the following: a) stones possess a heterogeneous microstructure with natural presence of areas of lower and higher density and inclusions; b) the cutting process might generate cracks in addition to those formed by the fatigue test. Point a) makes the process of finding cracks difficult, with zones of lower density resembling microcracks and vice versa; point b) introduces further doubt in the definition of which is a crack or not. In addition to its ambiguity, this technique is long, expensive, and requires a skilled technician to be employed. In the current case and in the prospect of an industrial quality check, it is concluded that CT is not a reliable investigation technique for the determination of stone cracks. Conversely, the images obtained give a clear idea of the stone microstructure, and location of impurities.

Chapter 7.

Conclusions

Two material configurations have been manufactured, L1C1 and L2C1, differing only by the type of limestone used in the upper layer. The measurements of thickness and the static flexural tests showed that the load at failure of L1C1 varies linearly with the composite thickness, while load at failure of L2C1 does not show correlation with thickness. A statistical analysis has been conducted on the propagation of uncertainties during the calculation of the load percentage to be applied in L1C1; as a result, it was not possible to state with precision if the theoretical load percentage applied is the real load percentage, being the variance of the force given by $\sigma_F = \frac{1}{b}\sqrt{\sigma_t^2 + \sigma_a^2 + \frac{\sigma_b^2}{b^2}(a-t)^2}$. The effect of statistical variance is most important when the F_{MAX} is between 70% and 80% of the static failure force, because in this load range there is a shift of behavior from infinite life to finite life. The data of failure for both materials can be plotted on a S-N diagram, but being the stone a very brittle material, the slope of the curve is very steep. This effect amplifies the uncertainty in measurement.

The models applied for the calculation of the neutral line in § 3.5 suggest it to be located 3.9 mm below the top layer, therefore in the interface between the GFRP layer and the cork layer. Such models, however, do not take into account the non-linear elastic behavior of cork and GFRP, which is why we can't say with confidence that the value is correct. A more precise analysis should be done with a VIC or with extensometric measurement. Our prediction is that the neutral line is located deeper into the cork layer.

The limestone in configuration L1C1 determines the cyclic failure of the composite, being it always due to stone crushing; infinite life occurs for $F_{MAX} < 70\%$.

For configuration L2C1, failure at high cycles also happens caused due to stone crushing; for a $F_{MAX} < 55\%$ though, the failure mode shifts to lower fiber breakage, and below 45% the composite can sustain infinite cycles. In order to have an increased fatigue resistance, it is convenient to improve the quality of the lower fiber layer, namely its grammage and geometry.

There is no statistical evidence to say that the resting time between cycles has a lifetime increasing effect. In tests with resting time, the failure occurred for cork shearing, demonstrating another possible mode of failure, in L2C1.

Future studies should be conducted regarding:

- Determination of the strains on each material layer, as well as the location of the neutral line with extensometers or VIC analysis; determination of the stone elastic modulus with, for example, the resonance method.
- Performance of fatigue tests in displacement control, and at constant velocity instead of constant frequency.

- Performance of fatigue tests with randomly variable loads and with $R < 0$, simulating the effect of the wind.
- Influence of the change of lower layer glass fibers on the fatigue behavior.
- Performance of fatigue tests on real components, in order to account for the effect of the fixing system on fatigue.

References

Adam, T.J. & Horst, P., 2017. Fatigue Damage and Fatigue Limits of a GFRP Angle-Ply Laminate tested under Very High Cycle Fatigue Loading. *International Journal of Fatigue*, 99, pp.202–214.

Åkesson, U., Hansson, J. & Stigh, J., 2004. Characterisation of microcracks in the Bohus granite, western Sweden, caused by uniaxial cyclic loading. *Engineering Geology*, 72(1–2), pp.131–142.

Allen, H.G., 1969. *Analysis and Design of Structural Sandwich Panels* 1st ed., Oxford: Pergamon Press.

Amaral, P. & Pinheiro, J., 2017. Multilayer laminate panel.

Ben Ammar, I. et al., 2014. Mechanical behavior and acoustic emission technique for detecting damage in sandwich structures. *Applied Acoustics*, 86, pp.106–117.

Anjos, O. et al., 2014. Effect of density on the compression behaviour of cork. *Materials and Design*, 53, pp.1089–1096.

Anon, lneg.pt. Available at: http://rop.lneg.pt/rop/ [Accessed May 29, 2017].

Atkinson, B.K., 1984. Subcritical crack growth in geological materials. *Journal of Geophysical Research: Solid Earth*, 89(B6), pp.4077–4114.

Burman, M. & Zenkert, D., 1997. Fatigue of foam core sandwich beams - undamaged specimens. *International Journal of Fatigue*, 19(7), pp.551–561.

Campbell, F.C., 2012. Fatigue and Fracture. In pp. 1–10.

Caprino, G. & Giorleo, G., 1999. Fatigue lifetime of glass fabric/epoxy composites. *Composites Part A: Applied Science and Manufacturing*, 30(1), pp.299–304.

Carlsson, L.A. & Kardomateas, G.A., 2011. *Structural and Failure Mechanics of Sandwich Composites*, Dordrecht: Springer Netherlands.

CBI Market Survey, 2010. *The natural stone and stone products market in the EU*,

Chow, T.M., Meglis, I.L. & Young, R.P., 1995. Progressive microcrack development in tests on Lac du Bonnet granite-II. Ultrasonic tomographic imaging. *International Journal of Rock Mechanics and Mining Sciences and*, 32(8), pp.751–761.

Correia, F.L., 2016. *Fatigue analysis of an asymmetric composite structure composed of dissimilar materials - thesis*. Istituto Superior Tecnico.

Costa, A., Pereira, H. & Oliveira, A., 2003. Variability of radial growth in cork oak adult trees under cork production. *Forest Ecology and Management*, 175(1–3), pp.239–246.

Curtis, P.T. & Moore, B.B., 1987. A comparison of the fatigue performance of woven and non-woven CFRP laminates in reversed axial loading. *International Journal of Fatigue*, 9(2), pp.67–78.

Daniel, I.M., Gdoutos, E.E. & Rajapakse, Y.D.S., 2010. *Major Accomplishments in Composite Materials and Sandwich Structures*, Dordrecht: Springer Netherlands.

DNV, 2003. Composite Components Foreword. *Design*, (January 2003), p.65.

Erarslan, N., 2016. Microstructural investigation of subcritical crack propagation and Fracture Process Zone (FPZ) by the reduction of rock fracture toughness under cyclic loading. *Engineering Geology*, 208, pp.181–190.

Gao, F. et al., 1999. Damage accumulation in woven-fabric CFRP laminates under tensile loading: Part 1. Observations of damage accumulation. *Composites Science and Technology*, 59(1), pp.123–136.

Gibson, L.J. & Ashby, M., 1997. *Cellular Solids - Structure and Properties* 2nd ed.,

Gil, L., 2007. *Cork as a Building Material*,

Gomes, G., 2016. *Characterization and optimization of the production process of sandwich composite structures*. Istituto Superior Técnico.

Graça, J., 2015. Suberin: the biopolyester at the frontier of plants. *Frontiers in chemistry*, 3(October), p.62.

Griffith, A.A., 1921. The Phenomena of Rupture and Flow in Solids. *Philosophical Transactions of the Royal Society A: Mathematical, Physical and Engineering Sciences*, 221(582–593), pp.163–198.

Harris, B., 2003. *Fatigue in composites: science and technology of the fatigue response of fibre-reinforced plastics*, Woodhead Publishing.

Harte, A.M., Fleck, N.A. & Ashby, M.F., 1999. Fatigue failure of an open cell and a closed cell aluminum alloy foam. *Acta*

Materialia, 47(8), pp.2511–2524.

Hossain, M.M. & Shivakumar, K., 2014. Flexural fatigue failures and lives of Eco-Core sandwich beams. *Materials and Design*, 55, pp.830–836.

Huang, J.S. & Lin, J.Y., 1996. Fatigue of cellular materials. *Acta Materialia*, 44(1), pp.289–296.

Jardin, R.T. et al., 2015. Static and Dynamic Mechanical Response of Different Cork Agglomerates. *Materials & Design*, 68, pp.121–126.

Jeon, K.W., Shin, K.B. & Kim, J.S., 2011. Evaluation of tension-compression and tension-tension fatigue life of woven fabric glass/epoxy laminate composites used in railway vehicle. *International Journal of Precision Engineering and Manufacturing*, 12(5), pp.813–820.

Jones, R.M., 1998. *Mechanical behaviour of composite materials*, CRC Press.

Kanny, K. & Mahfuz, H., 2005. Flexural fatigue characteristics of sandwich structures at different loading frequencies. *Composite Structures*, 67(4), pp.403–410.

Katunin, A., 2012. Fatigue and Thermal Failure of Polymeric Composites Subjected To Cyclic Loading. *Advanced Composites Letters*, 21(3).

El Mahi, A. et al., 2004. Modelling the flexural behaviour of sandwich composite materials under cyclic fatigue. *Materials and Design*, 25(3), pp.199–208.

Marder, a R., 1989. Replication Microscopy Techniques for NDE. *ASM Handbook : Nondestructive evaluation and quality control*, 17, pp.52–56.

Montesano, J. et al., 2014. A microscopic investigation of failure mechanisms in a triaxially braided polyimide composite at room and elevated temperatures. *Materials and Design*, 53, pp.1026–1036.

Munz, D. & Fett, T., 1999. *Ceramics - Mechanical Properties, Failure Behaviour, Materials Selection* A. Zunger et al., eds., Berlin, Heidelberg: Springer Berlin Heidelberg.

Pápay, Z. & Török, Á., 2010. Physical changes of porous Hungarian limestones related to silicic acid ester consolidant treatments. *Geological Society, London, Special Publications*, 331(1), pp.147–155.

Peng, S.S., Podnieks, E.R. & Cain, P.J., 1974. The Behavior of Salem Limestone in Cyclic Loading. *Society of Petroleum Engineers Journal*, 14(1).

Pereira, H., 2011. *Cork: Biology, Production and Uses*, Elsevier.

Pereira, H., 2015. The Rationale behind Cork Properties: A Review of Structure and Chemistry. *Biorresources*, 10(2005), pp.6207–6229.

Pereira, J.S., Bugalho, M.N. & Caldeira, M.D.C., 2008. From the Cork Oak to cork. *APCOR - Portugese Cork Association*.

Reis, R.L. & Silva, A., 2009. Mechanical behavior of sandwich structures using natural cork agglomerates as core materials. *Journal of Sandwich Structures and Materials*, 11(6), pp.487–500.

Rossmanith, H.P. ed., 1983. *Rock Fracture Mechanics*, Vienna: Springer.

S. Kneezel, D. & J. Scheffler, M., 2014. Stone-Faced Aluminum Honeycomb Composites — Quality Control and Testing. In *28th RCI international convention and trade show*. pp. 155–167.

Salvo, L. et al., 2010. 3D imaging in material science: Application of X-ray tomography. *Comptes Rendus Physique*, 11(9–10), pp.641–649.

Scheffler, M.J. et al., 2007. Testing of Composite Stone Faced Aluminum Honeycomb Panels. *Journal of ASTM International*, 4(7), p.100854.

Shafiq, B. & Quispitupa, A., 2006. Fatigue characteristics of foam core sandwich composites. *International Journal of Fatigue*, 28(2), pp.96–102.

Sharma, N., 2006. Fatigue of Foam and Honeycomb Core Composite Sandwich Structures: A Tutorial. *Journal of Sandwich Structures and Materials*, 8(4), pp.263–319.

Shenoi, R.A., Clark, S.D. & Allen, H.G., 1995. Fatigue Behaviour of Polymer Composite Sandwich Beams. *Journal of Composite Materials*, 29(18), pp.2423–2445.

Silva, S.P. et al., 2005. Cork: properties, capabilities and applications. *International Materials Reviews*, 50(4), pp.256–256.

Song, H. et al., 2016. Experimental analysis and characterization of damage evolution in rock under cyclic loading. *International Journal of Rock Mechanics & Mining Sciences*, 88, pp.157–164.

Steeves, C.A. & Fleck, N.A., 2004. Collapse mechanisms of sandwich beams with composite faces and a foam core, loaded in three-point bending. Part II: Experimental investigation and numerical modelling. *International Journal of Mechanical Sciences*, 46(4), pp.585–608.

Stowe, R.L., 1969. Strength And Deformation Properties of Granite, Basalt, Limestone And Tuff at Various Loading Rates. , p.154.

Takeda, N. & Ogihara, S., 1994. In situ observation and probabilistic prediction of microscopic failure processes in CFRP cross-ply laminates. *Composites Science and Technology*, 52(2), pp.183–195.

Takeda, N., Ogihara, S. & Kobayashi, A., 1995. Microscopic fatigue damage progress in CFRP cross-ply laminates. *Composites*, 26(12), pp.859–867.

Talreja, R., 2008. Damage and fatigue in composites - A personal account. *Composites Science and Technology*, 68(13), pp.2585–2591.

Toubal, L., Karama, M. & Lorrain, B., 2006. Damage evolution and infrared thermography in woven composite laminates under fatigue loading. *International Journal of Fatigue*, 28(12), pp.1867–1872.

Triantafillou, T.C. & Gibson, L.J., 1987. Failure mode maps for foam core sandwich beams. *Materials Science and Engineering*, 95, pp.37–53.

Tsai, K.H., Chiu, C.H. & Wu, T.H., 2000. Fatigue behavior of 3D multi-layer angle interlock woven composite plates. *Composites Science and Technology*, 60(2), pp.241–248.

Yang, B. et al., 2000. Bending, compression, and shear behavior of woven glass fiber-epoxy composites. *Composites Part B: Engineering*, 31(8), pp.715–721.

Yu, B. et al., 2015. 2D and 3D imaging of fatigue failure mechanisms of 3D woven composites. *Composites Part A: Applied Science and Manufacturing*, 77, pp.37–49.

Zabler, S. et al., 2008. High-resolution tomography of cracks, voids and micro-structure in greywacke and limestone. *Journal of Structural Geology*, 30(7), pp.876–887.

Zenkert, D. & Burman, M., 2011. Failure mode shifts during constant amplitude fatigue loading of GFRP/foam core sandwich beams. *International Journal of Fatigue*, 33(2), pp.217–222.

Zenkert, D. & Burman, M., 2009. Tension, compression and shear fatigue of a closed cell polymer foam. *Composites Science and Technology*, 69(6), pp.785–792.

Appendix A.

Thickness measurements

Table A-1 Thickness measurements of L1C1, average thickness, standard deviation and percental standard deviation

L1C1 thickness (mm)			Average	SD	SD%
19,67	20,05	19,57	19,76	0,253	1,3%
19,96	20,13	19,95	20,01	0,101	0,5%
20,08	20,15	19,93	20,05	0,112	0,6%
19,94	20,37	19,89	20,07	0,264	1,3%
20,05	20,13	20,23	20,14	0,090	0,4%
20,08	20,25	20,31	20,21	0,119	0,6%
20,19	20,59	20,57	20,45	0,225	1,1%
20,46	20,89	20,45	20,60	0,251	1,2%
20,57	20,76	20,55	20,63	0,116	0,6%
20,43	20,94	20,59	20,65	0,261	1,3%
20,54	21,00	20,54	20,69	0,266	1,3%
20,63	21,00	20,59	20,74	0,226	1,1%
20,71	21,28	20,70	20,90	0,332	1,6%
20,96	21,20	20,75	20,97	0,225	1,1%
20,84	21,00	21,20	21,01	0,180	0,9%
20,93	21,07	21,12	21,04	0,098	0,5%
20,99	21,32	21,00	21,10	0,188	0,9%
21,07	21,65	20,72	21,15	0,470	2,2%
20,94	21,50	21,10	21,18	0,288	1,4%
21,43	21,69	21,00	21,37	0,348	1,6%

Table A-2 Thickness measurements of L2C1, average thickness, standard deviation and percental standard deviation

L2C1 thickness (mm)				Average	SD	SD%
21,19	21,23	21,09	21,23	21,19	0,07	0,3%
21,27	21,39	21,20	21,24	21,28	0,08	0,4%
21,31	21,25	21,40	21,46	21,36	0,09	0,4%
21,70	21,80	21,26	21,44	21,55	0,25	1,1%
21,50	21,70	21,60	21,65	21,61	0,09	0,4%
21,55	21,63	21,51	21,90	21,65	0,18	0,8%
21,32	21,13	21,26	21,04	21,19	0,13	0,6%
21,22	21,42	21,20	20,95	21,20	0,19	0,9%
21,11	21,27	21,16	21,34	21,22	0,10	0,5%
21,23	21,33	21,16	21,27	21,25	0,07	0,3%
21,40	21,44	21,30	21,25	21,35	0,09	0,4%
21,33	21,27	21,30	21,50	21,35	0,10	0,5%
21,42	21,38	21,32	21,31	21,36	0,05	0,2%
21,26	21,44	21,28	21,53	21,38	0,13	0,6%
21,37	21,61	21,50	21,32	21,45	0,13	0,6%
21,64	21,52	21,42	21,25	21,46	0,17	0,8%
21,32	21,52	21,43	21,60	21,47	0,12	0,6%
21,39	21,41	21,45	21,64	21,47	0,11	0,5%
21,58	21,63	21,48	21,24	21,48	0,17	0,8%
21,41	21,70	21,45	21,71	21,57	0,16	0,7%
21,80	21,70	21,30	21,60	21,60	0,22	1,0%
21,55	21,60	21,60	21,76	21,63	0,09	0,4%